PROJECT FINAL REPORT

Grant Agreement number: ACP0-GA-2010-263913

Project acronym: ATLLAS II

Project title: Aero-Thermodynamic Loads on Lightweight Advanced Structures II

Funding Scheme: FP7: Collaborative Project: Small or Medium-Scale Focused Research Project Theme 7: TRANSPORT

Period covered: from   1st of May 2011 to   31st of October 2015

Project Deliverable: D1.1.8

Scientific representative of the project's coordinator:

Name: Dr J. Steelant

Title: Senior Engineer

Organisation: European Space Agency – European Space Research and Technology Centre (ESA-ESTEC)

Tel: +31/71/565.5552

Fax: +31/71/565.5421

E-mail: Johan.Steelant@esa.int

Project website address: www.esa.int/techresources/atllas_II

APPROVAL

Title	issue	revision
ATLLAS II: Final report	1	

Author(s)	date
J. Steelant (ESA)	
M. Dalenbring (FOI)	
M. Kuhn (DLR)	
M. Bouchez (MBDA)	
J. von Wolfersdorf (USTUTT)	

Approved by	date
J. Steelant (ESA)	

Table of contents

List of Figures

List of Tables

Nomenclature

Acronyms

CFD   Computational Fluid Dynamics

Roman Symbols

T   temperature [K]

Greek Symbols

ρ   density [kg m^{-3}]

Superscripts and subscripts

i   species index

1   Final Publishable Summary Report

This is a comprehensive summary of results, conclusions and the socio-economic impacts of the project. The publishable report shall be formatted to be printed as a stand alone paper document. This report should address a wide audience, including the general public.
Please ensure that it:

- *Is of suitable quality to enable direct publication by the Commission.*
- *Is comprehensive, and describes the work carried out to achieve the project's objectives; the main results, conclusions and their potential impact and use (including the socio-economic impact and the wider societal implications of the project). Please mention any target groups such as policy makers or civil society for whom the research could be relevant.*
- *Includes where appropriate, diagrams or photographs and the project logo, illustrating and promoting the work of the project.*
- *Provides the following information:*
  - List of all beneficiaries with the corresponding contact name and associated coordinates
  - The address of the public Website of the Project as well as relevant contact details.

1.1   Executive Summary

Not exceeding 1 page

1.2   Project Context and Objectives

ATLLAS-II is a logical continuation project built upon the experience and technology development gained within *ATLLAS-I*. The focus will again be on advanced light-weight, high-temperature material development strongly linked to a high-speed vehicle design. The previous study revealed in the end that the optimal cruise Mach numbers is around Mach 5 to 6. In line with the reviewers' comments, a detailed design and feasibility study is proposed here which aim to a globally optimized vehicle with respect to aerodynamic, propulsive, structural and thermal layout but nevertheless allowing restrictions imposed by emissions regulations and sonic boom mitigation. The validated tools developed previously along with the lessons learnt will allow the consortium to further address and improve the multi-disciplinary design process.

In parallel, a lot of effort is still foreseen to extend the precious built-up material database with durability characterization both for the aero-frame and combustor related structures. Also new materials and compositions are addressed to cope with limitations previously encountered.

As mentioned before, a novel aircraft design for high-speed flight is retained in the present proposal. The description of the objectives is split up along the vehicle design process and the material development. Concurrently the recommendations of the reviewers are used as a general guideline in the project set-up.

Design of a Mach 5-6 Vehicle:

The driver to set the requirements for the material manufacturing, processing and testing is a Mach 5-6 vehicle. A fully integrated design taking into account several disciplines in the trade-off and optimization is foreseen, fully in line with the reviewers' comments. The points to be addressed are:

a. *Integrated Aerodynamic and Propulsive Flowpath Layout*

The envisaged vehicle must operate over a wide Mach number range (0-5) and should still be efficient at cruise conditions. The wake analysis performed as part of *ATLLAS-I* suggests the

cruise efficiency peaks at the cruise speed of Mach 5-6. However, the wake analysis takes no account of any material limitations and insulation weight at higher flight Mach numbers. The objective is to derive the optimum cruise Mach number by balancing thermal constraints (WP2.2) with the noted increase in cruise efficiency at higher speeds (WP2.1). The use of different fuel combinations will be assessed to maximize range, whilst recognising that the thermal management of the vehicle and/or the emission requirements will also require the use of cryogenic fuels such as liquid methane or a mixture of CH_4 with hydrogen. The challenging part is to design the vehicle that can create the flow-field described by the combined analysis. Also sonic boom constraints will have an impact on the global layout.

b. Conceptual Structural and Thermal Design

Hypersonic vehicles are exposed to temperatures that are beyond the limits of classical airplane materials. In order to handle this problem the latest developments of new materials and composite structures suitable for high temperature application need to be taken into account. In this context, it is necessary to handle also the integration of heat-shield/heat-resistant materials and less heat-resistant load-carrying structural members including thermal management systems. One of the main objectives is to create inputs for virtual testing and multi disciplinary optimisation (MDO) of realistic full-scale structures at operating conditions by the use of advanced numerical high fidelity methods. Besides the aero-thermal loads, also the unsteady loadings on the structure and control surfaces originating from shock-wave boundary layer interactions will be included. Their impact on control effectiveness and flutter will be first evaluated thoroughly as a separate topic, both experimentally as numerically, prior to the application onto the vehicle.

Despite the usage of high-temperature resistant structural materials, the passengers and cargo will require a stable thermal environment throughout the full vehicle's route. For subsonic aircraft, the cold ram air is used to thermally control the cabin air temperature which is drawn off the compressor. However, for high-speed vehicles, the ram air temperature needs rather to be cooled. The presence of onboard cryogenic fuels (e.g. CH_4) allows studying alternative designs to those used in subsonic aircraft. Open and closed cycles for the cabin air will be addressed.

c. Environmental Restrictions onto the Design Process

The major obstacles of introducing a supersonic aircraft have been the lack of solution to the sonic boom problem, emissions at high altitude and the risk of stratospheric ozone depletion. A first step has been performed in *ATLLAS-I* in terms of tool development and application. Sonic boom prediction for the studied vehicles in *ATLLAS-I* revealed similar levels as for Concorde but could eventually be alleviated by increasing the rise time, which transforms the boom rather into a puff. This encouraging path will be embedded into the design.

Apart from cruise induced sonic boom also acceleration from subsonic speed (M < 1.0) to cruise speed (M = 5 to 6) leads to the creation of a zone of sonic boom amplification due to ray convergence. This superboom may be especially annoying as it may be close to the coasts and very loud because resulting from the part of the flight path around Mach 1.2 – 1.3 for which the aircraft is at a much lower altitude than during cruise. It is known for Concorde type aircraft to be about 3 to 4 times larger than cruise sonic boom, with a major change in the waveform (from an "N"- to a "U"- wave) and with increased sensitivity with regard to local meteorology. To our knowledge, focused boom from hypersonic configuration has never been evaluated. Atmospheric turbulence is known to strongly modify the shock fronts of the sonic boom. In the mean it decreases the amplitude and increases the rise time, by means of scattering of the sonic boom by the largest structures of the planetary boundary layer. However, in a few percentage of cases, it may lead to its amplification, up to a factor 2, by means of random focusing. It is known for Concorde type booms to induce a variability of at least +/- 5 dBA (A-weighted Sound Exposure Level) in terms of usual noise metrics. Impact of turbulence on the sonic boom from a hypersonic configuration has never been evaluated.

Emission goals set by the EC could be achieved by the use of alternative fuels, such as methane or a CH_4/H_2-mix, having the potential to reduce carbon dioxide and particle emissions and thereby limiting the influence of supersonic aircraft on the atmosphere composition. The use of a more clean fuel will have the potential to eliminate the soot in the exhaust, something that has been lifted up lately as a concern in level with the CO_2 in the context of global heating. On the other hand required high combustion temperatures (regardless of fuel type) still make a reduction in NOx emission a challenge. Nevertheless, some guidelines formulated during *ATLLAS-I* will reduce it considerably if taken into account in the preliminary vehicle design. The global effect on the ozone at these cruise altitudes will be investigated as well.

d. Overall Vehicle Optimization and Final Assessment

The integration of the different subsystems, each optimized individually with preset restrictions, into a single vehicle system design does not necessarily ensure a globally optimized vehicle. Due to the complexity of interdisciplinary interaction, numerically steered improvement and optimization tools are applied here to ascertain a global optimum. Within the frame of the *ATLLAS-I* project a new modular MDO tool for the preliminary design of high speed vehicles was developed. The tool allows multiple-operational point analyses by means of aerodynamic and structural computations using CFD and FEM. Also flight mechanics aspects and propulsion integration are taken into account. A key conclusion from the study is the dominating effect of structural dimensioning over aerodynamic improvements. Hence a stronger consideration of the structural modelling and analyses including aeroelastic and thermal effects are targeted in *ATLLAS-II*.

As a powerful precursor to the multi-disciplinary optimisation (MDO) a stochastic multidisciplinary improvement (SMDI) is proposed. SMDI makes use of techniques based on the Monte Carlo method. Its goal is to move the performance of a system towards a predefined target. The usage of Monte Carlo methods implies that a whole cloud of solutions is generated and moved through the design space towards the desired target.

As an ultimate verification, the optimized vehicle design will be tested for subsonic, transonic and supersonic speed to see how the design, mainly driven by cruise conditions, is able to cope with take-off and transonic acceleration. Variable settings of control surfaces to investigate trimming and stability will be part of the test campaign. The verification will be further backed-up and extended to other trajectory points, including cruise, with Nose-to-Tail computations which uses the windtunnel results also as a validation. The effect of boundary layer transition has a large effect on the vehicle drag and heat load. Therefore, dedicated experiments and LES simulations are also foreseen to assess the start and extent of the boundary layer transition taking important effects such as compressibility, wall temperature and roughness into account. All of this will further reduce the uncertainty margins when a final assessment will highlight the vehicle performance in terms of range, payload, fuel consumption, weight, emissions and sonic boom. These elements could serve as a first input to an economical assessment with respect to development and exploitation costs.

Advanced Material Development for Aero-Frame and Combustor Structures:

As spelled out above, the highly loaded structure requires the implementation of advanced metallic and non-metallic materials which need to be light-weight and high temperature resistant. The large unknowns of these materials are their mechanical, thermal and optical (emissivity) characterizations at high temperatures as well as their durability capability. These information was completely lacking in the open literature at the start of *ATLLAS-I*. A first unique database is now available which lists these properties as useful engineering correlations as a function of temperature up to 1800 K. With respect to durability in real application environments, the samples have mostly been exposed to short duration tests. This lacking information will be a priority point in the material characterization. Nevertheless the database will be also expanded with new materials or compositions. This is needed to cope with shortcomings observed for certain materials in

ATLLAS-I but which can be overcome by adapting their compositions or manufacturing process. This is mostly related to improve their oxidization behaviour or resistance to fatigue and fracture mechanisms.

a. *Durability and Integration Technologies for Aero-Frame Materials*

Both metallic and non-metallic materials are considered for the aeroframe-structure. The titanium matrix composites (TMC) and nickel based hollow sphere stackings (HSS) are investigated for use as (semi-)cold structure or as sandwich panel with good cooling and acoustic damping capabilities. The non-metallic class will focus on Ultra-high Temperature Ceramics (UHTC) and Ceramic Matrix Composites (CMC).

i. After the encouraging results on high-temperature Hollow Sphere Stacking (HSS) processing route obtained at the end of *ATLLAS-I* project, the objective of this second part is to carry on with the HSS materials characterization and testing in order to have several solutions dealing with components for structural hot areas of a high-speed aircraft, such as sharp leading edge, air intake or nozzles. In particular, the large challenge of extremely porous metallic materials such as cellular materials is their resistance to oxidation and to creep. The development of high temperature Ni-based materials will be directed towards a protected-brazing route with sandwich materials that can be thermally characterized. This particular technique offers the advantage to be applied with every kind of elemental cells such as spheres, tubes or corrugated sheets. New high-temperature architectures obtained through brazing of tubes or relief-patterned sheets into a regular sandwich structure configuration will be investigated.

ii. Titanium alloys and Ti-aluminides exhibit excellent mechanical properties for applications where high specific strength, high ductility and toughness, good corrosion resistance as well as high creep and fatigue resistance are required. Their useful service temperature range from room temperature to about 800K. New design concepts require however higher mechanical and thermal loading. Therefore new materials concepts must be developed beyond the classical monolithic titanium alloys towards titanium based composites. Such Titanium Matrix Composites (TMCs) combine high strength, stiffness and creep resistance of Silicon Carbide (SiC) monofilaments with the damage tolerance of Ti-alloys and Ti-aluminides while further reducing the materials density. The use of TMC on high-speed vehicles is related to shafts and hinges of control surfaces (ailerons, canards), different engine parts (compressor, turbines, shafts), structural and actuation struts, landing gears, brake systems. The intention is here to investigate and characterize the limits of TMC samples as well as the fabrication and testing process for compressor blades at high thermal and mechanical loading to evaluate the potential of titanium metal matrix composite (TMC) for high temperature material use in hypersonic applications. This will require characterization of the performance of TMC based on aerospace standard and alternative high temperature grade alloys. A down selection of the alloy type will allow for the fabrication of a full scale generic component part, scheduled for testing. Trial component designs and potential fabrication routes to achieve the required reinforcement architecture for an agreed performance specification will be developed.
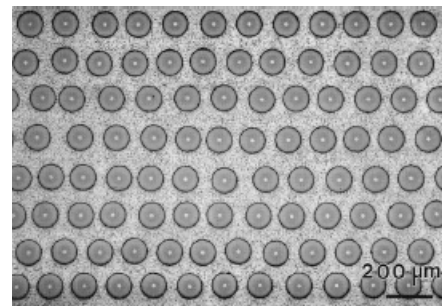
iii. After the encouraging results on three selected Ultra High Temperatures Ceramics (UHTC) obtained during the *ATLLAS-I* project, the objective of this second part is to pursue the investigation of UHTC materials in order to have at our disposal several solutions for components working under severe thermal and
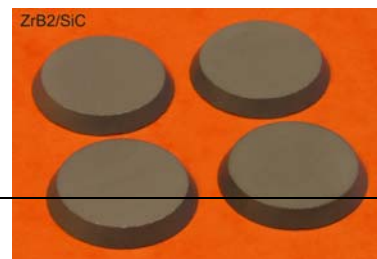
structural loads e.g.: wing leading edge, nose, air intake etc. Their capability to be tailored to a sharp leading edge will improve the aerodynamic performance. The main objectives are firstly to select UHTC compositions able to sustain the requirements, secondly to acquire basic knowledge of these materials (manufacturing processes for example) and thirdly to thoroughly characterize the sintered ceramics.

iv. Works in *ATLLAS-I* clearly revealed the demand for experimental data concerning fatigue and creep behaviour of the investigated CMCs, especially at higher temperatures. For the integration of CMCs into the load bearing structures, the materials behaviour in the vicinity of stress intensifying elements like slots, notches and holes has to be determined, evaluated and taken into account for design. Test setups and procedures will be defined to test samples at operation relevant test conditions. Additionally, the investigation of test samples to check for material changes (caused by load changes) is foreseen.

For the CMCs, enhanced coatings will be applied; experiences on EBCs (environmental barrier coatings) with C/C-SiC are available and should be extended to other CMCs. Such a coating could be e.g. cordierite, which can be applied by means of vacuum plasma spraying. Coated CMCs are able to withstand high temperature oxidation satisfying the demand of a long-term application.

v. As there will be a considerable temperature difference between the internal compartments and the aerodynamically heated outer skin of the hypersonic vehicle, different design possibilities of integrating the outer skin panels and the cold substructure needs to be explored. This temperature difference imposes a design constraint requiring an optimum fuselage structural concept very different from a conventional aircraft. Several different structural concepts exist for a primary cold load-carrying structure, which are explored at a first stage. Likewise the design and joining of the outer skin panels need to accommodate for the large thermal expansions in comparison to the substructure. Due to the finite panel size the influence of steps and gaps on airflow, and thus heating, but also on strength and stiffness will be analysed. An extensive know-how in joining a hot outer CMC structure to a cold, metallic substructure is proven for re-entry applications but not for hypersonic spacecraft demanding for long-life terms. It will be studied whether this technology can be adapted to civil hypersonic travel. Different aspects like e.g. inspection accessibility, exchangeability or fatigue considerations need to be treated here.

b. Durability and Integration Technologies for Combustor Materials

The high thermally loaded walls of the propulsion units require particular material development. Both metallic and non-metallic materials are considered for the different combustor components. CMC-based combustors with transpiration and/or regenerative cooled walls were shown to have a great potential as light-weight material combined with active cooling. However life-time and durability need to be proved to ensure their applicability for the defined goals. Nozzles parts or other heat loaded panels can be accommodated for by sandwich panels which have a high-temperature resistant core based on Ni-HSS. They have the additional possibility to act as cooled panel with good acoustic absorption. Finally, the most loaded parts are the injectors sticking out in the flow.
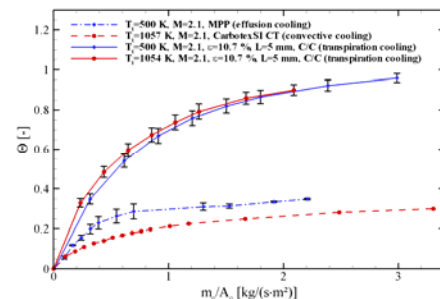
Also here different materials are checked from the durability and integration point of view.

i. The measurement of erosion and damage of transpiration or convectively cooled walls is a critical issue for actively cooled propulsion systems. The long term behaviour and life-time characterization of different CMC (oxide or non-oxide) materials will be investigated using a small scale HVOF kerosene/oxygen burner. This investigation will focus on material compatibility with respect to combustion products (H_2O, H_2, CO etc.), changing of permeability, erosion resistance at high temperatures (< 3000 K), thermo-physical and porous-fluidic properties at both room and high temperature levels. Detailed local heat transfer data for regenerative internal cooling configuration will be addressed experimentally and numerically.
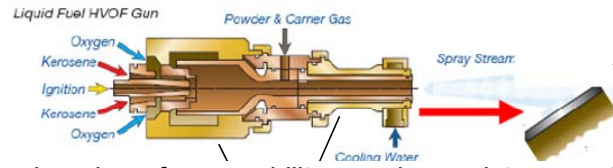
ii. The high thermally loaded walls of the propulsion units require particular material development. A sandwich structure with HSS core combined with CMC panels was identified as a key technology in *ATLLAS-I* and appears to be an attractive component in the design of lightweight, high-temperature, actively cooled structures. In order to evaluate the thermal insulation performance of HSS, thermal characterisation of hybrid HSS-CMC structures need to be performed under realistic conditions. A HSS cooled or uncooled panel assembly will be designed, manufactured and implemented at the exit of the existing SMR chamber for combustion test in METHYLE hypersonic test facility. These data will be used for a thorough inspection and feasibility assessment. To allow the assessment a dedicated coupled aero-thermal analysis will be performed. The numerical tools used were developed in *ATLLAS-I* and will be further developed for the present application.

c. Integration and Testing of (Un)Cooled Injectors

Injectors have to face a severe thermo-mechanical environment: aerodynamic loading due to the incoming air flow, very high temperature, high internal fuel pressure, etc. In addition, the final application requires very thin pieces to be efficient. UHTCs are very promising as uncooled fuel injectors used within airbreathing propulsion units. It was demonstrated in *ATLLAS-I* that these ceramics can quite easily be machined to obtain sharp leading edges or air-intakes e.g. by EDM or with diamond tools. Another approach is the use of porous CMC which is fuel-cooled by transpiration. Each type of injector will be experimentally exposed to a really harsh combustion environment within the SMR dual-mode ramjet combustion chamber METHYLE.
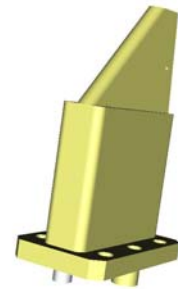
1.3 Description of the main S&T results

1.3.1 ==Not exceeding 25 pages:→ 5 pages per WP==

1.3.2 Detailed Design of a Mach 5-6 Vehicle

>> to be composed by WP2-leader with help of WP2-partners

Max. ½ page

1.3.3 Aero-Frame & Materials Integration

>> to be composed by WP3-leader with help of WP3-partners

Max. ½ page

1.3.4 Combustor and Material Integration

>> to be composed by WP4-leader with help of WP4-partners

Max. ½ page

1.3.5 Aero-Thermal-Structural Loads at High-Speed

>> to be composed by WP5-leader with help of WP5-partners

Max. ½ page

2   Design of a Mach 5-6 Vehicle

2.1   Conceptual Vehicle and Engine Design

The starting point in WP2 is the concept development based upon a fundamental analysis of the aircraft wake that was first presented as part of the ATLLAS-I, in which GDL conceive a 2-D flow-field for maximising cruise efficiency and then create a vehicle configuration that realises the flow-field. During the initial design, handbook surface inclination methods were used to predict aerodynamic forces from panel type geometrical description of the vehicle. For the propulsion system design part, an in-house method-of-characteristics GDL code was used to develop intake geometry with the intake model is coupled with a 1-D model for the turbofan and ramjet. Trajectory profiles are generated using the GDL in-house 3-DoF solver.

As a part of this study the performance of a hypersonic intake was also investigated by ESA for several flight conditions (Ma=0.3, Ma=1.6, Ma=3.0 & Ma=5.0 and AoA=0°, AoA=2° & AoA=10°) by using a 3D Euler CFD TAU simulations. In order to assess the performance, two indicators, mass flow rate (MFR) and mass capture efficiency (MCE), have been calculated. For Ma=5.0 and Ma=3.0 an appropriate solution could be obtained. It is noticeable, that for Ma=5.0 the whole internal flow path of the throat could be simulated, see Figure 3. This resulted in significant differences between the outflow and cowl mass flow rate. The development of the MCE shows a reducing efficiency for a decreasing Mach number, see Figure 4. However, In case of subsonic flight conditions the trend does not continue and the MCE starts to grow. The investigations revealed a suboptimal performance for the Ma=1.6 and Ma=0.3 intake geometry resulting in losses of mass inside the throat and unstarted solutions. On the one hand, these issues could have occurred due to numerical issues like the grid quality or the capability of the TAU CFD solver.
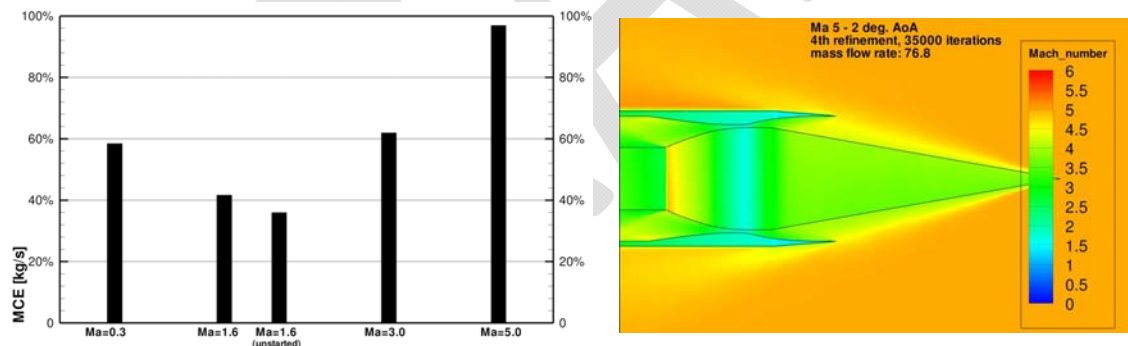
Figure 1: Bar chart of mass capture efficiency for Ma=0.3, Ma=1.6, Ma=3.0, Ma=5.0

For a better understanding of the flow behaviour in general and especially of the internal flow path, viscous effects should be taken into account for further investigations. Viscous calculations would also be able to simulate the thickening of the boundary layer, which has an effect on the throat diameter and therefore an effect on the intake performance. Based on the aerodynamic and propulsion design different vehicle configurations were developed. The analysis was extended to consider also the effect of venting an under-expanded exhaust into the base of the fuselage. The predicted cruise efficiency of this configuration is slightly lower than for a lee-side expansion analysed in ATLLAS-I, but has the advantage of separating the aerodynamics of the wing from the propulsive jet, thereby offering an alternative means of integrating the aerodynamic and propulsive flow fields. Based on these findings three separate vehicles were defined and analysed, and the so called baseline configuration was chosen through a down-selection process, see Figure 6. The baseline configuration feature a wide body fuselage sheltered behind a nose mounted variable geometry intake for the main engine together with nacelle mounted engines on each wing behind smaller intakes, with details reported by GDL & ESA in **D2.1.1** [2].
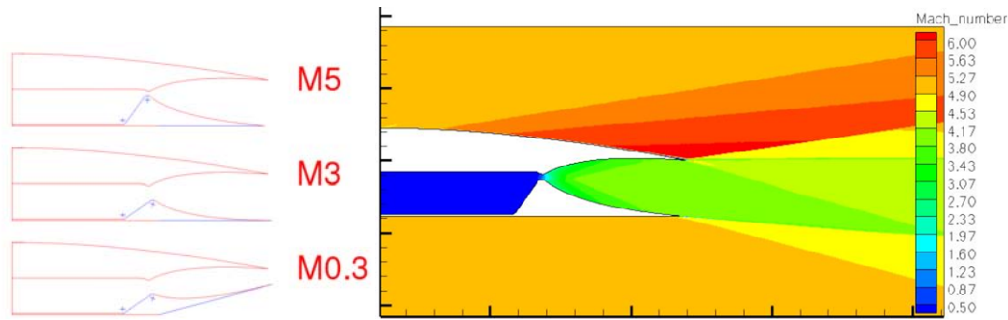
Figure 2: Mach contours for Mach numbers 0.3 and 5.0; MFR in kg/s

Under-expanded exhaust

Over-expanded exhaust venting into lee of the wing

Twin fuselage with under-expanded exhaus

Baseline configuration
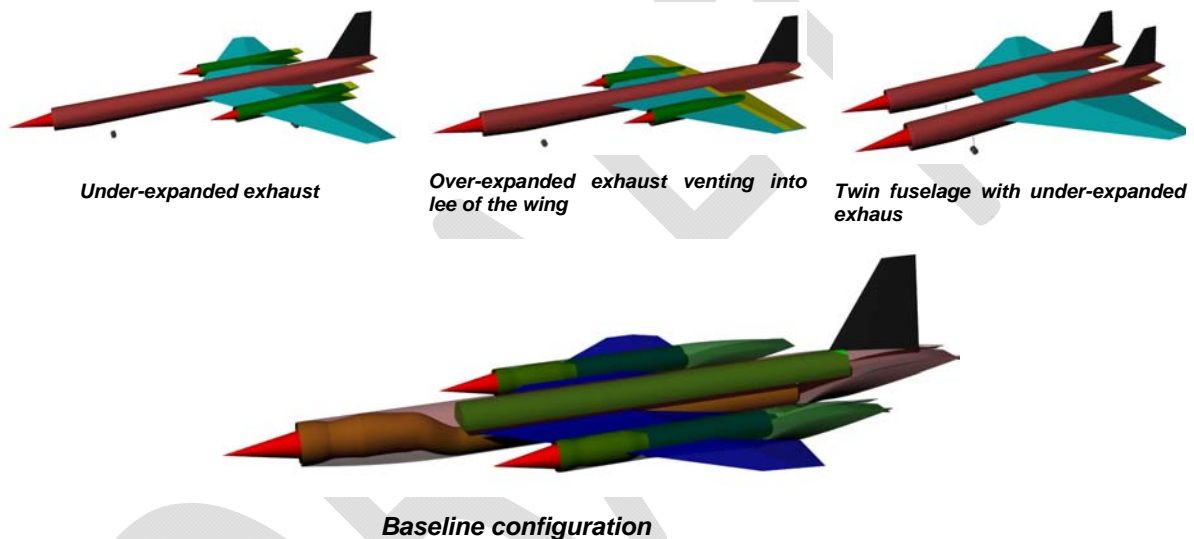
Figure 3: The ATLLAS II candidate vehicles (upper) and selected baseline configuration

Finally the resulting geometry of the design process was imported into CAD and then used to generate a full vehicle mesh to be used with the TAU CFD low solvers in the final vehicle assessment reported in ATLLAS-II deliverables **D2.1.2** [3] and **D2.1.3** [4]. In particular two trajectory points were considered:

- Take-off at Mach 0.3, including angle of attack (crucial for trajectory feasibility)

- Cruise performance at Mach 5.0 (important also for thermal aspects)

The intake of the engines were considered as perfect outflows (therefore without considering the possible fan effects) and the exhausts of the engines started at the nozzle throat. Moreover, the variable are of the engine nozzles was correctly simulated rotating at CAD level the dedicated panel. The simulations were carried out for full turbulent flow Navier-Stokes equation with standard Spalart-Allmaras model for turbulence. At take-off, Mach 0.3, a recirculation is found at the exit of engine nozzles. The lift at 0° of angle of attack (AoA) is low compared with the vehicle weight (1675 kN), while at 10° AoA the generated lift is higher than the vehicle weight (4920 kN). The calculated drag seems to be higher than the engine thrust by about 25% at both AoA. At cruise, Mach 5, a very good agreement is found with the optimization results in terms of lift (2900 kN) and engine performance (intake mass-flow capture, drag versus thrust). The average surface temperature is around 1200-1300 K, with limits up to about 1800 K on part of the leading edge close to the engine nacelles, see Figure 8.
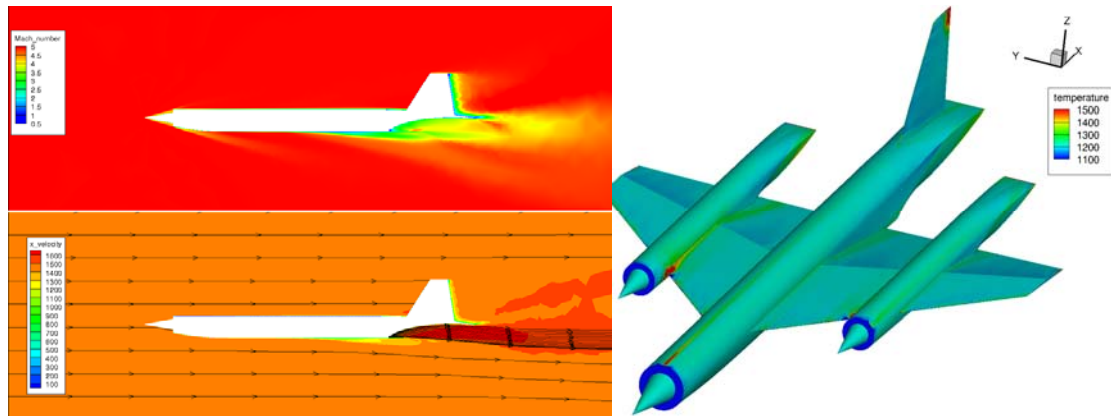
Figure 4: General flow field for Mach 5.0, AoA 0° (left) and surface temperature (right).

2.2 Conceptual structural and thermal design

The starting point in WP2.2 is the three different vehicle configurations developed within WP2.1, with special emphasis on aerodynamic and propulsion design. In WP2.2, structural and thermal design were performed in order to support the configuration design process and to allow for the identification of tendencies. It was decided to perform structural analyses already in this early stage of the design process, since the application of statistical/empirical methods is handicapped due to the limited availability of corresponding data for high speed vehicle concepts. The results of these investigations supported the configuration design process and were exploited in order to define the final configuration. Initially, a mass and centre of gravity (cog) estimation was performed for all three reference configurations using statistical/empirical methods.

First, an analytical fuselage design study was performed. Here, different structural design and passenger cabin integration concepts and materials have been evaluated in order to identify promising solutions. Also, aerodynamic models for all three configurations have been generated using an inclination based high-speed aerodynamic & aerothermodynamics code. The computed aerodynamic loads for the most relevant load cases were fed into the structural analysis process, while the estimated surface temperatures allowed for material selection and thermal protection system (TPS) sizing.

As a part of the down-selection process DLR-SART developed and used a parameterized finite element (FE) structural sizing tool to determine the structural weight needed to carry the expected flight loads reported in **D2.2.2** [5]. The most important part of the structural investigations was formed by different finite element (FE) based trade studies. For this task, the recently developed parametric structural analysis tool HySAP (Hypersonic vehicle Structural Analysis Program) has been applied, which was then modified in order to allow for investigation of the ATLLAS configurations. Using HySAP, different design parameters have been investigated on a comparative basis. The most relevant part was an aspect ratio study, where the impact of wing aspect ratio on the structural mass of the vehicle was evaluated, see Figure 5. Furthermore, different wing rib/spar spacings, alternative wing profiles and wing/nozzle integration concepts have been investigated. The FE-based investigations were complemented by first order analytical studies that investigated selected design features such as wing flow transfer duct or wing/fuselage carry-through design options.
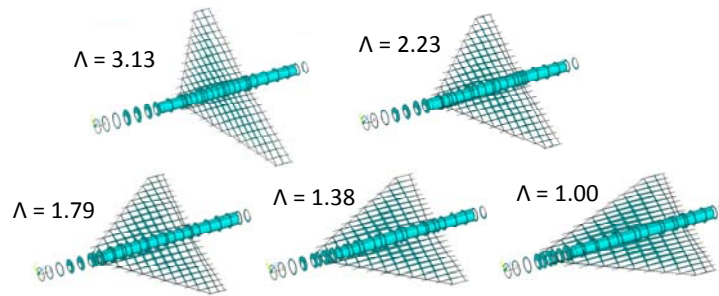
Figure 5: Internal structural architecture models for aspect ratio study

Based on the initial results of the structural analyses, a modified configuration ("Preferred Concept") was created by GDL, integrating structural and aerodynamic considerations. For this preferred concept, a new series of structural trade-off analyses comparing different structural architectures was performed (Figure 11).
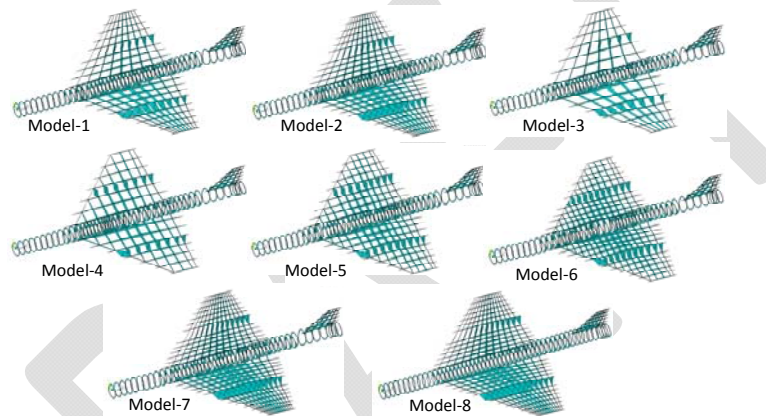
Figure 6: Structural architecture configurations for the preferred concept

From these concepts, a structural architecture was eventually selected (Model-1 in Figure 11). For this architecture, a structural material and structural design trade-off was done (Figure 12) using Aluminium (Al), Titanium (Ti), and Aluminium-Lithium (Al-Li) alloys as preferred materials. On the structural concept side, uniaxial stringer stiffening and honeycomb sandwich (SW) were compared. Finally, a 1D TPS sizing study was conducted for the complete vehicle surface (Figure 13), comparing three different TPS architectures.
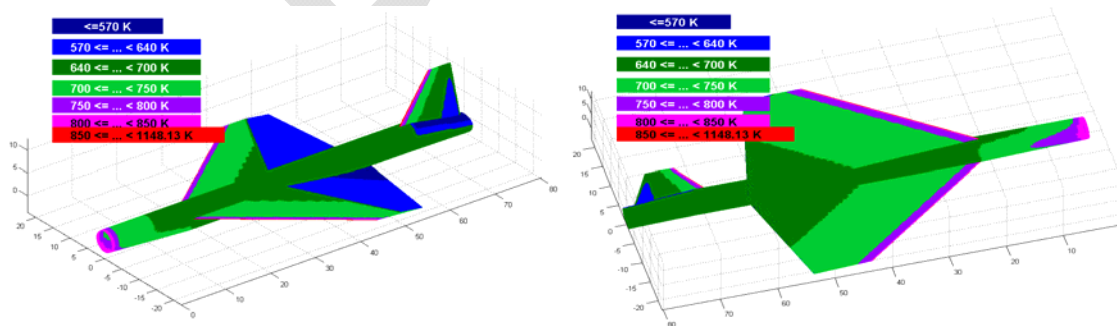
Figure 7: TPS material/concept surface partitioning for 1D TPS sizing study

The trade-off studies revealed low weight solutions for an aspect ratio range of Λ = 1.5-2. Also, a strong interaction of wing and fuselage mass was found, which may be a result of the comparatively deep wing root. The results were exploited for the redefinition of the baseline concept. Furthermore, a medium structural member spacing was found to be preferable, and all-sandwich structural design concepts allow for lower weights for this configuration compared to stringer-stiffening. The utilization of Aluminium-Lithium as structural material showed large weight saving potentials in the order of 20 % compared to Aluminium and Titanium structures. However, because of the better high-temperature resistance of titanium, the latter is proposed for the vehicle structure. Moreover, a titanium structure may allow for significantly higher structural temperatures, and therefore reduce TPS mass. Indeed, the TPS sizing study revealed that a TPS designed for a structural temperature of 300 K is around 58-74 % heavier compared to an approach where wing and the non-passenger carrying parts of the fuselage are insulated for 480 K. The result from this study was compared with a similar investigation done by GDL. Reasonable agreements were found, with slightly higher masses estimated by DLR. The mass estimations were later updated iteratively in order to account for the evolution of the designs through the development process.

Transient thermal simulation for a very sharp nose (with 2 mm radius) does indicate that there will be a rather high temperature at the tip of the leading edge. The temperature at the base of the leading edge will be however significantly lower. While at the tip of the leading edge, UHTC will become necessary since the temperature is very high, for the area behind the leading edge, other materials may be considered. The simulation by FOI suggests a feasible solution for a hot leading edge design. According to this design, UHTC will be used at the leading edge. Behind UHTC, high temperature CMC plates will be used as a bracket to connect the leading edge to the main structure. The bonded joint is preferred for the joint between UHTC and CMC with a co-cured technique, or even with high temperature adhesives. The CMC will bridge the gap between UHTC and the main structure with materials for even lower temperature tolerance. CMCs, super-alloys, TMC (Titanium-alloy matrix composite), or even Titanium alloys may be considered for the main structure. Since the joint between the CMC plates and the main structure will be subjected to lower temperature, low cost mechanical joints of super-alloys may be considered for the ease of assembly, maintenance, and reparations. Such a design may eventually enable beneficial design of sharp leading edge for hypersonic vehicle. Detailed analysis of a critical wing leading edge and a typical TPS panel, including a first life-time assessment, was reported in **D2.2.4** [6].

In future works the effect of elevated temperatures on the structural material characteristics, as well as thermal stresses have to be analysed. Furthermore, the very heavy TPS has to be reinvestigated in more detail for mass saving potentials, in particular when considering the heat sink capability of the kerosene fuel stored in the wing.

A massive weight penalty is incurred if insulation alone is used to manage the cabin thermal environment. Active cooling is therefore required. This involved re-circulating exhaust cabin air through a cooling duct wrapped around the internal cabin skin. A model based on the Law-of-the-Wall was developed to estimate the heat leakage rates from the duct cooling channel. Once the cabin thermal protection system had been developed, the last step in the analysis was to design an air-conditioning system that could not only provide conditioned air to the cabin at 10°C, but could also provide sufficient auxiliary power to drive the hydraulic, pneumatic, and electrical systems. The pre-defined structural concept was eventually delivered to project partner for further structural-dynamic analysis. The thermal management layout for the cabin and the general thermal and structural sizing of the structure was done. A novel and efficient air-conditioning and auxiliary power cycle scheme was designed by GDL and reported in **D2.2.1** [7], requiring relatively small volumes of cryogenic fuel. Air taken from the intake at 6 bar and 1250 K, is cooled and expanded to cabin conditions and then used to cool the cabin-wall before finally it is used to cool the air from the intake. The cycle is expected to generate approximately 730 kW. The methane is assumed to be burnt in the engines after it has performed its cooling duty, and for a 288K temperature rise the required flow-rate of methane is 0.82kg/s, equivalent to a fuel burn of 4.5 tons during a 90 minute cruise.
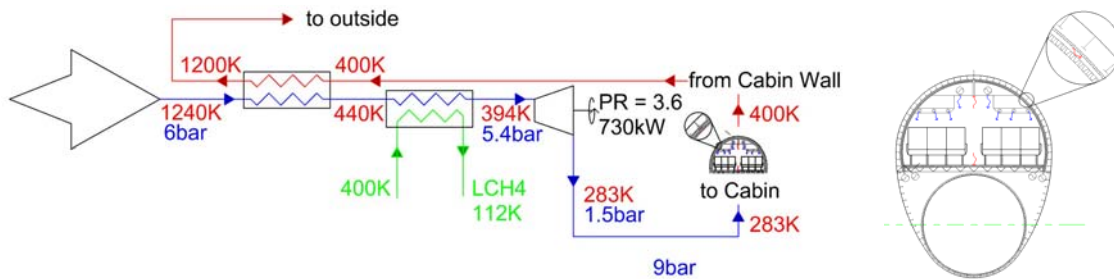
Figure 8: Cabin air-conditioning and auxiliary power cycle scheme

Moreover, high-speed cruise vehicles require the use of high temperature materials to withstand the high thermal fluxes during flight. The long duration of a flight dictates a proper thermal protection system to cope with the integrated heat load accumulated during flight while a part of this heat might need to be evacuated after touch-down. Structural analysis shows that the thermo-mechanical fatigue is the sizing parameter for the hypersonic vehicle structural design. For a given distance to be crossed at a given dynamic pressure for a cryogenically fuelled vehicle, it was observed that paradoxically the faster one flies, the lower the heat loads are as well as the accumulated thermo-mechanical cyclic loads.
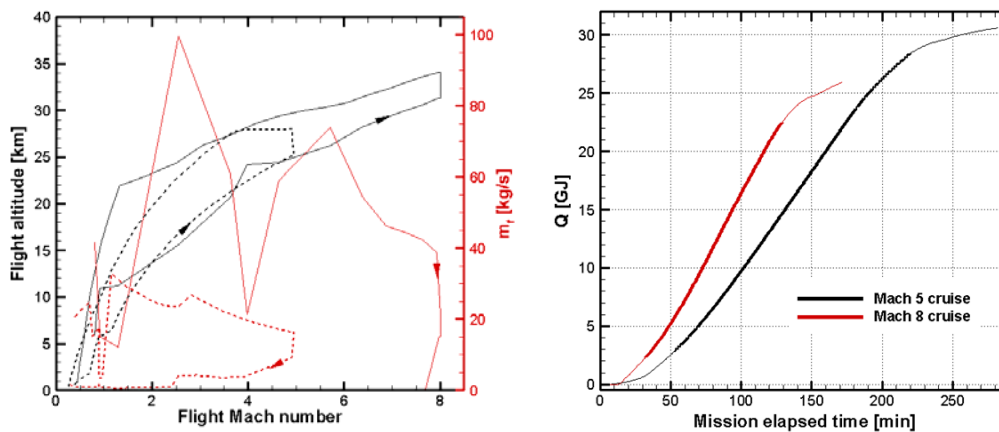
Figure 9: Comparison of missions (right picture) for M5 (dashed) and M8 (full): trajectory (black) and fuel consumption (red) and Integrated heat load Q during the Mach 5 and the Mach 8 missions (right picture).

This would result into a lighter TPS panel while having a longer life-time in terms of flights. The basic analysis is discussed on the basis of representative test cases. In order to properly assess the service life of a hypersonic cruiser the operating temperature, the mechanical loads as well as the exposure time need to be taken into account. The heat fluxes on the aeroshell during short duration trans-atmospheric missions, e.g. launch and re-entry, increase with the cubic power of the free-stream velocity. Already a simplified zero-dimensional analysis can highlight that this approximation is not appropriate for hypersonic cruisers travelling a predefined range using a cryogenic fuel as propellant e.g. hydrogen. Actually the thermal flux during Mach 8 flight is shown to be only 25 to 35% higher than at Mach 5. On top of this, the reduced flight times at Mach 8 yields a 20 to 25% reduction of the overall integrated heat load to the fuselage with respect to the Mach 5 cruise. This means that the integrated heat load decreases with increasing flight Mach number. The study was then extended towards a one-dimensional analysis to confirm these trends along a full trajectory. A similar paradox was observed from the thermo-mechanical fatigue analysis where the reduced flight time at higher Mach numbers actually increased the number of flights before the material needs to be replaced. The scarce data available on thermo-mechanical fatigue of carbon matrix composites shows performance degradation at relative high temperatures (reported up to 1300K).

In order to prepare for the multi-disciplinary optimisation (MDO) the model from DLR was converted by FOI into a NASTRAN model. This FE model was used by FOI as a starting point for a trade-off study and structural sizing analysis based on setting a constraint on the first eigenfrequency and using the internal optimiser in NASTRAN, reported in **D2.4.3** [9]. The issue investigated here is the implication of an eigenfrequency constraint used as a substitute for the aeroelastic (flutter/divergence/control-authority) and flight handling qualities constraints. Starting for the Aircraft Handling Qualities [10] including the MIL spec [11], "the thumbprint" says something about the short period requirement form a pilot perception perspective. High natural frequency increase response with the risk of pilot induced oscillations; i.e. you would like the frequency to be above 0.5 Hz for good response and also relatively low damping. Low frequency and high damping is a bad combination with bad flying qualities as result. A flight control system may of course enhance stability and handling qualities by increasing system damping, with the sacrifice of response. Based on the MIL specification, the ATLLAS II vehicle is of Class III, Category and Level 1, the short period frequency suggesting upper limit of omega around 3 rad/sec, in order to have good handling qualities. The final question is however the separation between the short-period body modes and the first elastic mode. This is outside the scope of ATLLAS II but an eigenfrequency constraint on the first eigenvalue of 2 Hz was later used in the MDO.

2.3 Environmental Impact – Sonic boom and high altitude emissions

The environmental impact in terms of sonic boom and high altitude emissions were addressed within WP 2.3. To accurately predict the shock and expansion patterns sufficiently far from the vehicle, as input to acoustic propagation methods, an automatic mesh adaptive unstructured CFD-solver for the nearfield acoustics was developed at ONERA, reported in **D2.3.2** and **D2.3.4** [16, 17]. Once coupled to nonlinear raytracing for atmospheric propagation, this model can be used to quantify the sonic boom at the ground level during the aircraft cruise in a stratified atmosphere. For ICAO standard atmosphere with no turbulence, the sonic boom from ATLLAS II hypersonic configuration was calculated and the ground undertrack boom was estimated to 91 dBA (ASEL), in the same order as the Concorde (89 dBA) **D2.3.6** [18] but with a peak at lower frequency. Width of ground geometrical footprint is larger than Concorde (136 km) because of higher Mach and higher altitude. Localization of caustic resulting from transonic acceleration was also achieved, **D2.3.5** [19]. However, it is also well known that atmospheric turbulence within the planetary boundary layer (PBL) near the ground significantly alters the shape of the sonic boom waveforms. A state-of-the-art code, so-called FLHOWARD3D, for statistical prediction of sonic boom through turbulent atmosphere was developed. Numerous validation tests have been successfully carried out to simulate the propagation of the sonic boom in a turbulent atmosphere near the ground, reported in **D2.3.6** [18]. The code includes propagation of non-linear shock waves in 3D atmosphere, flow motion, sound speed, density heterogeneities, atmospheric absorption (thermo-viscosity and N_2/O_2 molecular relaxation) and rigid ground reflection.
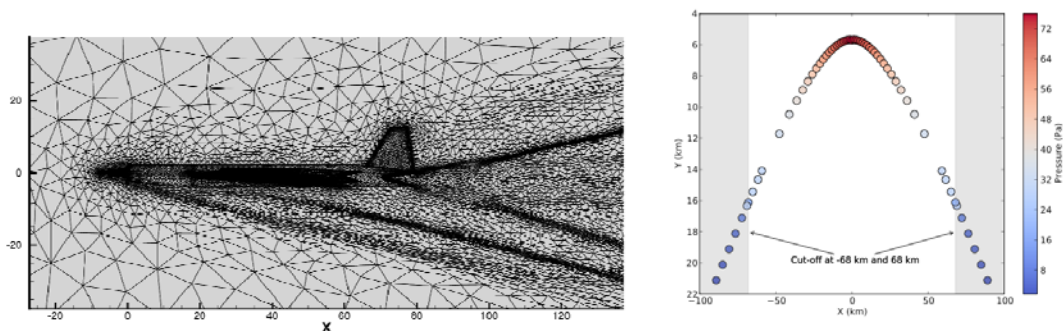
Figure 10: Left: example of automatic mesh adapted to shock capturing – Right : ground footprint of sonic boom from ATLLAS II configuration at cruise Mach number 5 (colors indicate peak overpressure in Pa).
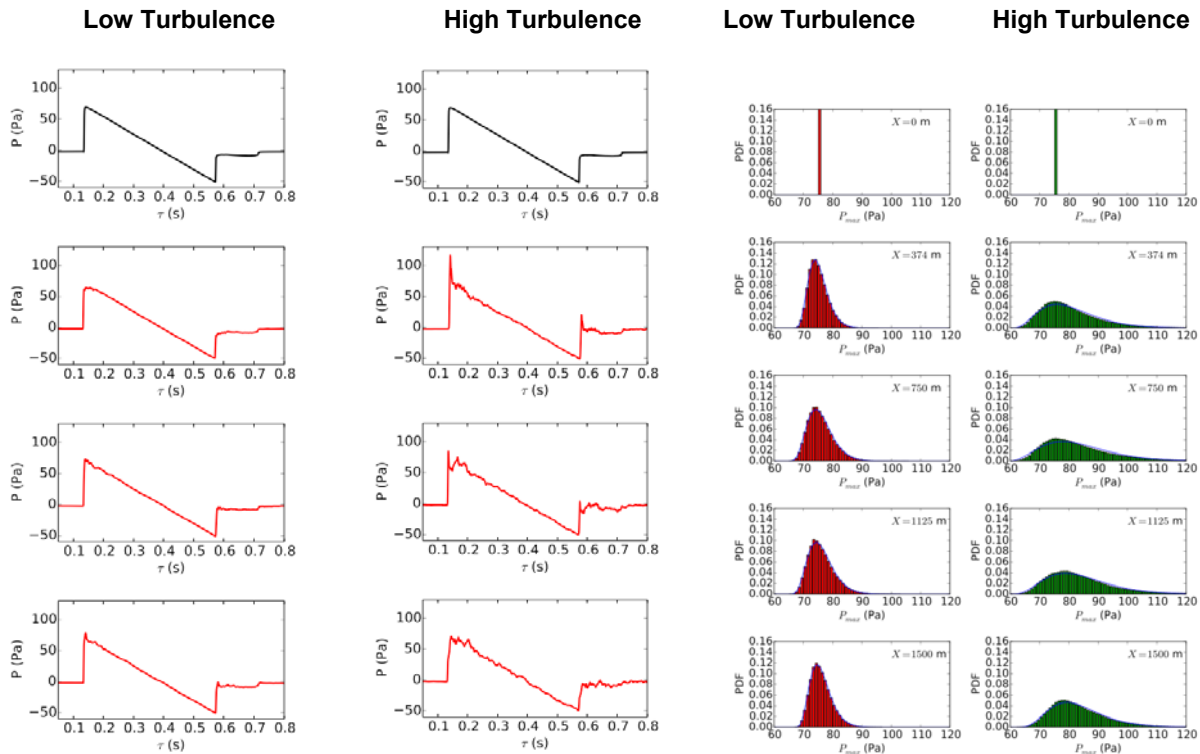
Figure 11: Left figure: examples of simulated boom pressure signatures in the PBL. Left column: small turbulence/Right column: strong turbulence. Top line (black signal): ground track boom in case of no turbulence. Right figure: histograms of peak pressure amplitude (in Pa). X is the boom propagation distance in the PBL with X=0 on top of PBL and X=1500m at ground level. Left column: small turbulence/Right column: strong turbulence.

The code is massively parallel (MPI), with typical boom simulations requiring 4×10^{12} dofs. PBL is modelled by means of synthetic turbulence with a von Kármán energy spectrum. Statistical boom variability was quantified for two cases **D2.3.5**, [19]: (i) ground track sonic boom in cruise conditions (ii) sonic boom penetration into the lateral shadow zone. The first case provides information on the global annoyance caused by sonic boom, while the second specifies the geographical extent of the boom. For ground track boom, standard deviation is relatively high and positively skewed, indicating that there is a significant probability of high intensity peak pressure. For lateral boom in the shadow zone, peak overpressure is enhanced due to sound scattering by turbulence.

GDL targeted the general problem about low sonic boom vehicle shaping, Figure 20. A 3D Method of Characteristics (MOC) code was written by GDL to extrapolate near field data. Comparison with an axisymmetric MOC test case revealed an error that grew with radius. The error was traced to the assumption that gradients tangent to the Mach cone could be treated as constant. An analytic impulse function F generated for an ideal wave-rider design, to produce a minimum boom, was used to validate a fit for purpose Cart3D CFD code **D2.3.7** [20], see comparison in Figure 21. Analysis of wind tunnel results reveals that the lift contribution to boom can be similar to the L.B. Jones minimum, but the disturbance generated by even a relatively fine nose can increase the F integral by a factor of 3 resulting in a $\sqrt{3}$ increase in N wave shock pressure.

FOI and GDL did joint work focusing on the possible atmospheric impact of a future ATLLAS2 fleet. This includes potential global warming effects as well as stratospheric ozone impact from emissions of H_2O, CO_2 and NO_x. For a traffic corresponding to 100 ATLLAS II baseline flights the results indicate a risk for ozone layer depletion of the order of 0.15 to 0.4% as a mean over the

Northern hemisphere. This effect is due to a combined NO_x and H_2O impact. The span in ozone depletion reflects directly the span in cruise NO_x emission index, $EINO_x$, which due the current engine design level has to be given as a rather wide span. From the current engine design EINOx levels where set to 5-20 g/kg fuel. The possibility to produce atmospheric impact is the results from extensive studies found in the literature, allowed for studies that otherwise would not have been possible within the given WP 2.3 and and reported in **D2.3.1** and **D2.3.3** [21]. Trajectory data was established by GDL in WP2.1, engine emissions data in collaboration with FOI.
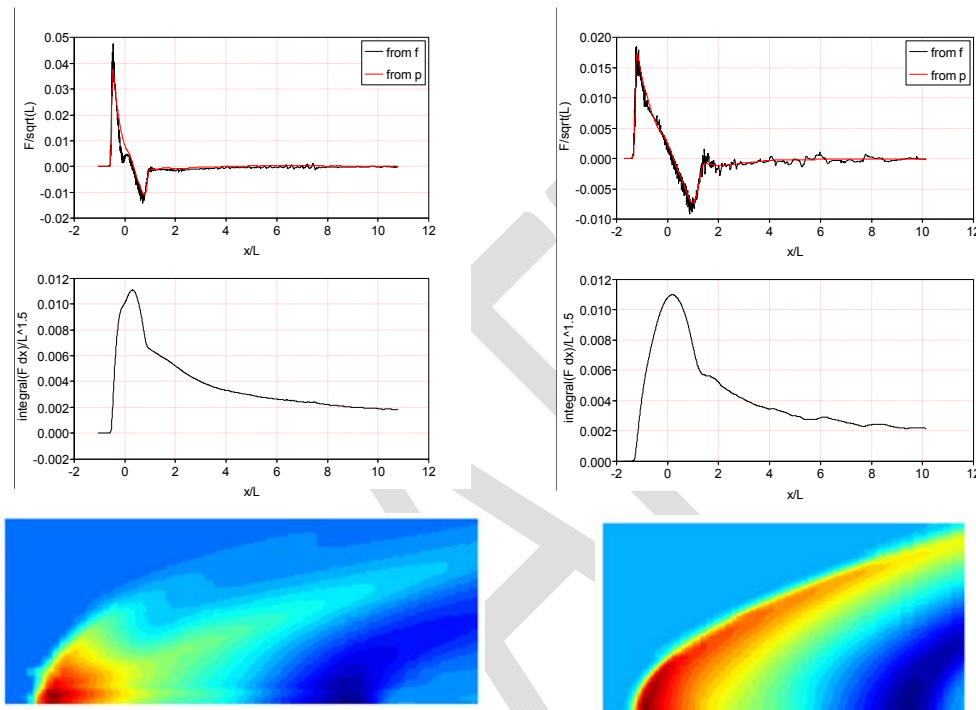
Figure 12: Verification of the Cart3D code and F function derivation from downwash

2.4 Overall vehicle optimization

The integration of the different subsystems, each optimized individually with preset restrictions, into a single vehicle system design does not necessarily ensure a globally optimized vehicle. Due to the complexity of interdisciplinary interaction, numerically steered improvement and optimization tools are applied here to ascertain a global optimum. Within WP2.4 modular MDO tools for the preliminary design of high speed vehicles was developed.

The goal of WP2.4.1 is to pre-optimise the ATLLAS-II Mach 5 vehicle. In addition, it is intended to investigate the applicability of stochastic methods for that task. The chosen stochastic methods are Monte Carlo simulation (MCS) and for Stochastic Design Improvement (SDI). MCS can be used to analyse a design over its entire design space by randomly varying the input parameters and recording the resulting responses. In the scope of this WP MCS was used to test the robustness of the model before optimisation. Only a model that runs reliably can be used in an optimisation process. The SDI method was selected because in general the method itself is robust and fast. SDI consists of performing a small MCS around a start design, selecting the best design and then using that design as the new start design. The process is repeated until a desired target in the design space is reached or no further improvement is achieved. The process resembles a cloud of samples being moved through the design space.

Performing any kind of stochastic simulation or optimisation requires a tool chain that is robust and runs automatically. Therefore, most work went into creating a model that runs successfully at least 95% of times. All processes are controlled through the optiSLang software package. It calls the tool chain via a single batch script. The different deterministic tools, which are part of the tool chain, are connected to each other via awk scripts. The goal of the improvement process was to maximise range and increase the first eigenfrequency to 2 Hz. The work consisted of setting up an interdisciplinary model for an optimisation process, ensuring the robustness of the model and finally improving the starting design by applying the Stochastic Design Improvement (SDI) method.

Figure 13: Mass break-down showing the components that are optimised by HySAP and TOP2

A model that includes mass estimation, hypersonic aerodynamics and a structural optimization was set up. A model robustness of 95% was reached by sampling the design space using Monte C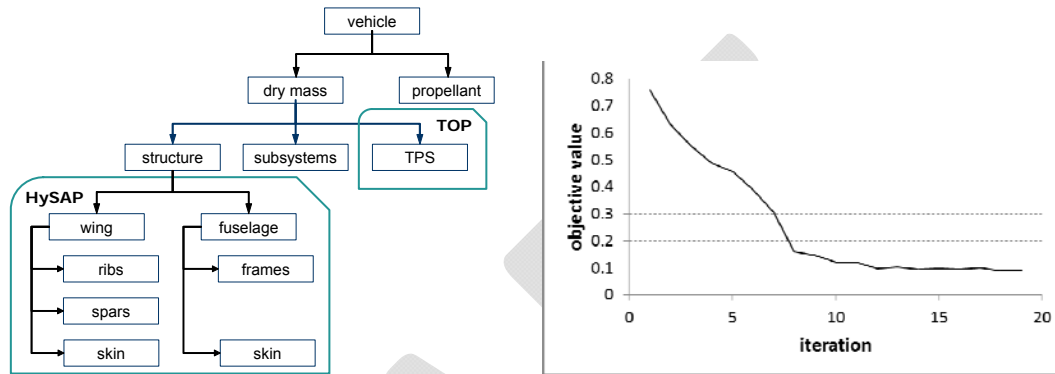arlo simulations (MCS) and solving the modelling problems that arouse. Afterwards a theoretical optimum for a hypersonic Mach 5 vehicle was found by applying the Stochastic Design Improvement (SDI) method. Two variants of the vehicle were optimised, one with straight and one with slanted spars. The arrangement of the spars had no influence on the optimal wing geometry. For both cases the design drivers could be clearly identified. These were the aspect ratio and the rib spacing. In case of the slanted spars the sweep angle also had an influence on the structural design. The designs that resulted from the SDIs were suitable for hypersonic cruise flight but looked unusual compared to traditional wing designs. Therefore, the take-off and landing performance of those designs was analysed. The designs with very low aspect ratios could not take off at a speed comparable to the Concorde. Therefore, a design from an earlier iteration of the SDI with slanted spars was selected. That design was modified by using the rib spacing from the overall best design of that SDI run. As the rib spacing is a major design driver this improved the range of that design.

The result from this work shows how to use MCS for ensuring model robustness and how to set up SDI to quickly improve a design. Further, the correlations between different parameters that were used in the SDI process were analysed. As SDI is a stochastic method analysing the correlations between the different parameters allowed to clearly identify the design drivers. It would have been beneficial to include take-off and landing performance in the SDI process. The improvement process only considered hypersonic cruise flight and was lacking a physical constraint for the aspect ratio.

In WP 2.4.2, a method for inclusion of aeroelastic constraints within the structural analysis part of a more general multi-disciplinary optimization scheme is proposed and demonstrated here. The proposed methodology is here investigated and demonstrated on a complete vehicle including the wing. It is demonstrated how aeroelastic phenomena such as flutter damping can be analysed within NASTRAN. One advantage is that the same structures-model can be used here as for the stress-analysis and the eigenfrequency analysis. New is the need to define the aerodynamic mesh for the panels-method and the structures-aerodynamics model coupling parameters. It is further demonstrated how the optimizer within NASTRAN can be used to find an optima (minimum

structural mass), considering a number of sub-cases, each having different constraints. The optima found can be used as an initial guess for the global multidisciplinary optimization (MDO). A stress analysis and sizing was performed by DLR using ANSYS [**D2.2.2**] for the baseline configuration described in [**D2.1.1**]. Different structural layouts, with different topologies, were analysed.

The optimizer in ANSYS was used for sizing taking minimum weight as cost-function and a defined value of the Von-Mises stress in each element as constraints. The model with this sizing from DLR was converted by FOI into a NASTRAN-model being used as the basis for the work described in **D2.4.3** [23]. One advantage in NASTRAN is that the same structural model can be used here for stress-, eigenfrequency and aeroelastic analysis. It is demonstrated how the optimizer within NASTRAN can be used to find an optima (minimum structural mass), considering the eigenfrequency constraint. When this work was finished the model, including the setup for weight-optimization taking flutter into account has been delivered to DLR for inclusion into the global MDO, where other disciplines such as engine performance, propulsion efficiency etc. are also included. The main result found was that the long and heavy nacelles makes it necessary to increase the torsional and bending stiffness of the inner wing to satisfy flutter and eigen-frequency constraints. Making the nacelles shorter and lighter would save structural weight, and so would a thicker wing profile in the inner wing with more internal volume. The wing-skin thickness in the inner wing was increased, whereas the outer wing skins and the fuselage and fin skins have a reduced thickness. The total weight resulting from the optimization increases the initial weight from 188 tons to 215 tons in order to satisfy the constraints. This corresponds to 14.5%. Furthermore, for a complete flight envelop, additional load cases should be taken into account, however, this will probably yield an increase in total weight.
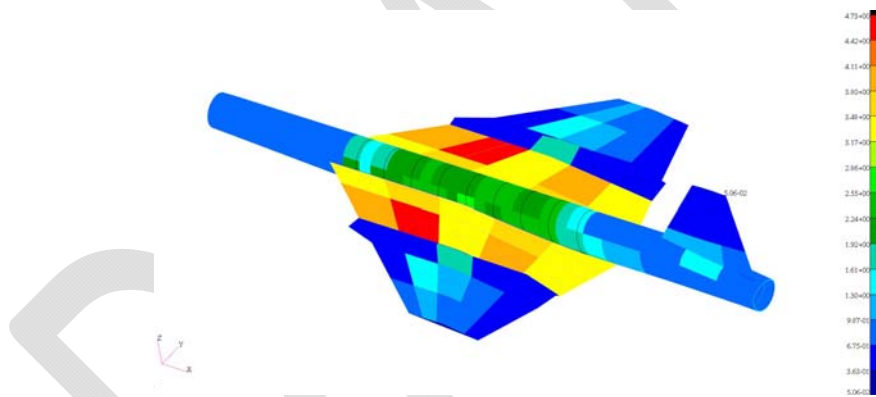
Figure 14: Design variables at the end of the optimization (allowed: 0.5 < dv <50)

In WP 2.4.3 focus has been on the setup of methodologies for design improvement and multidisciplinary optimization (MDO). The test case is the ATLLAS II vehicle and the implication on weight or range on the chosen set of design parameters and constraints. The baseline structural FE model developed during period II, including a thermal protection system (TPS) lay-out and interior equipment, was used as a starting point. DLR-SART performed a range optimization study on the reference configuration using the method of stochastic design improvement (SDI) **D2.4.1** [22] whereas DLR-RFZ used the simplex method, reported in **D2.4.2** [24]. The SDI study was limited to the cruise part of trajectory and clearly shows the importance on added relevant constraints into the optimization in order to avoid sub-optimization. The DLR-RFZ work on the other hand, used an adapted detailed FE model, optimized with NASTRAN to global constraints. The grid generation uses the DLR in-house code MegaCads to obtain a fully parameterized autonomous CFD grid generation for both structured, unstructured and hybrid grids. The CFD code TAU (Euler) was used for Nose-to-Tail evaluation of the aerodynamic performance analysis in the MDO loop. Trimming canards and elevators were not implemented in CFD but added afterwards by airfoil theory. The DLR-RFZ weight minimization procedure was executed with eigenfrequency and aeroelastic constraints included as a part of the multidisciplinary optimization (MDO).

Necessary modules such as the mission module, the module analysing engine and vehicle aerodynamic effects were also integrated. Separate engine calculations for engine thrust by bookkeeping method; linear engine-trust model based on selected CFD based points. In the model, drag equals trust was associated with the fuel mass flow for each configuration.
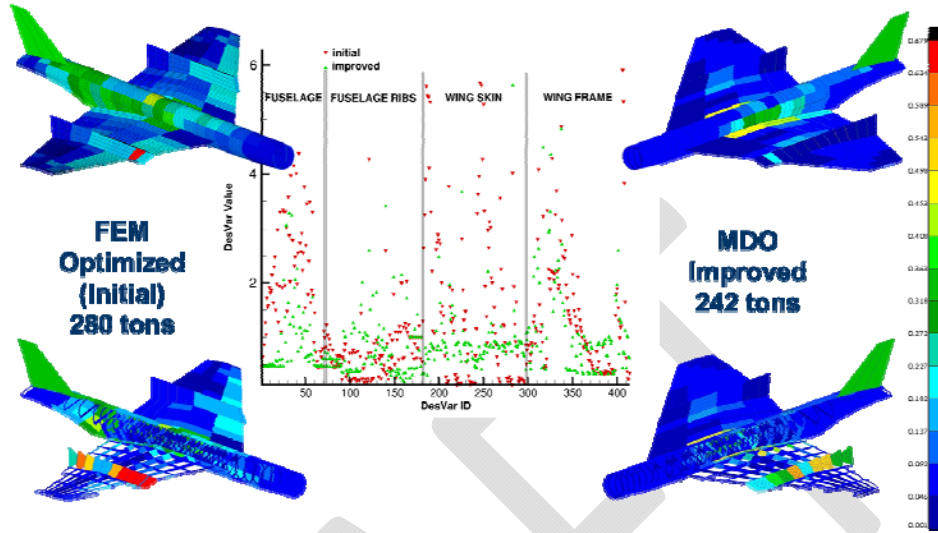
Figure 15: Result from structural optimization and change in design variables

The objective function module collects for each iteration lift, drag, moment coefficient and mass-data, and combines it into a punished Brequet range function. The result, presented in Table 2, shows that the improved vehicle has better range, L/D and less weight, compared to the starting original design. Figure 7 and 8 shows the new shape and the effect on the design variables respectively.

MDO Improved
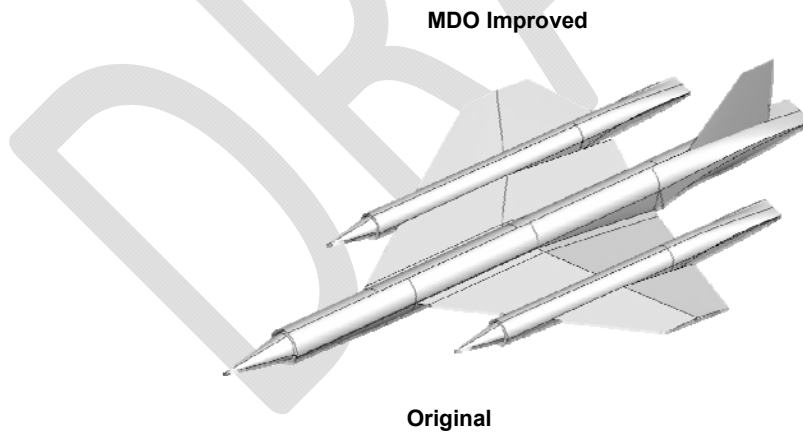
Original

Figure 16: Result from MDO original (lower) and improved (upper part)

	Original	Improved
Range	~6800 km	~9800 km
Fuel	187 tons	223 tons
Dry mass	280 tons	242 tons
Wing area	807m²	835m²
L/D	8.5	9.4

Table 1: Summary DLR MDO result

The evolution of vehicle weight as a function of time is plotted in Figure 42. From this picture it is clear that the original estimation of vehicle weight is significantly lower than the final weight. A more detailed analysis shows that the eigenfrequency constraint is a strong design driver that should have caused more action. This constraint was originally created as a substitution for the aeroelastic (flutter/divergence/control-authority) and flight handling qualities constraints reported in **D2.2.3** [9]. For the future, one should include also flight handling constraints, so that the eigenfrequency constraint could be removed. Possibly a safety factor between the structural eigenfrequencies and flight dynamics rigid body modes, for a few points in the envelope, as suggested in the literature would have been sufficient.

Figure 17: ATLLAS II Mach 5-6 vehicle dry weight evolution

As an ultimate verification, the vehicle design was tested for subsonic, transonic and supersonic speed to see how the design, mainly driven by cruise conditions, is able to cope with take-off and transonic acceleration. Variable settings of control surfaces to investigate trimming and stability will be part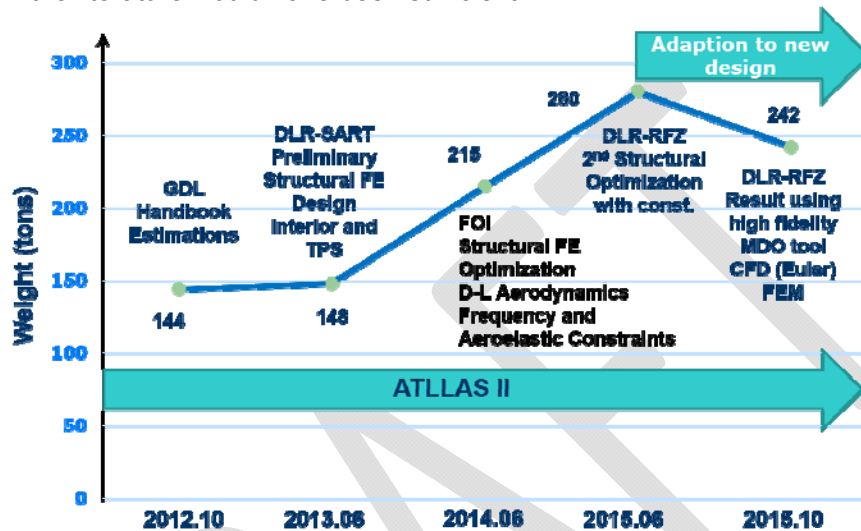 of the test campaign. The verification will be further backed-up and extended to other trajectory points, including cruise, with Nose-to-Tail computations which uses the wind tunnel results also as a validation. The model was designed with adjustable conical inlets and ducts designed to maximize internal flow. Detailed design was done of the intake geometry and adjustable exhaust by using detailed CFD analysis. The wind tunnel model scale is 1/70, having a wing span dimension of 645,7 mm and length of 1354,6 mm. Pressure measurement were performed using 8 Kulite sensors (with 50 samples/sec simultaneously), sonic boom and Schlieren visualization. A new sting with dimensions L=1150mm by D=40mm was manufactured with a contact protection, strain-gauges and sting force measurement added to avoid overloading. In total, a number of 110 WT runs were performed. Measurement Stage I included measurements of forces, moments, pressure on the model and pressure measurement at the model exits up to Mach 1.5. Bottom wall pressure measurement for sonic boom characterization was performed at Stage II. The sting was shortened by 373 mm during Stage III due to high structural vibrations in order to manage test up to Mach 2.5, see details in **D2.4.4** and **D2.4.5** [25, 26].

Nose-to-Tail validation for transonic configuration (ESTEC) using a total of 28 3D turbulent simulations were carried out varying grid dimensions and refinement, Mach number, angle of attack (AoA) and cone position (to change the intake area for higher Mach). The validation of TAU performed at ESA, in terms of aerodynamic coefficients, was performed considering the following conditions in terms of Mach number performed by INCAS: 0.5; 0.9; 1.03 and 1.5 (although for the latter, the actual Mach number was around 1.4). In addition to that, points at Mach 0.3 (for cross-comparison with DLR for the MDO), Mach 2.5 and 5 were also performed. At Mach 0.5 good agreement is found both for Cl and Cd at the lowest Mach numbers. In particular, a maximum shift

in Cl of 0.0045 (8%) is found at -4 degrees (corresponding to about 0.15° in AoA), while the maximum error on Cd is about 4% at 4 deg. No clear comparison with Cm could be performed, but Cm_α was found identical (-0.0085). In general a good convergence for the aerodynamic parameters was found. A comparison was also possible between TAU result and the results of the FOI Edge code simulations and good agreement was generally found in terms of flow field.

Figure 18: The transonic wind-tunnel-model with interior flow-path for the baseline

The experimental L/D curves are compared with CFD and acceptable alignment is observed between wind tunnel data and simulation result. Mach number 1.2 is considered to be relatively difficult to predict as it is slightly above the transonic range where the shocks starts to form and the result is sensitive to the shock position. The following settings where used in the wind tunnel at INCAS, see Ref. [25, 26]. WT test run 7878 (red curve) and 7929 (yellow) are measured at Mach 1.2 with a wall porosity set to 2.5%. Run 7883 (blue) were taken at Mach 1.19 with a wall porosity of 4% and finally run 7885 (green) at Mach 1.22 with a wall porosity (BOV) of 4%. The experimental L/D curves for Mach numbers 1.2, 1.6 and 2.5 are compared with CFD simulation, including also the internal engine surfaces in the force calculation, in Figures 14-17. One may notice here that run 7883 (blue curve) for Mach 1.2 is close to the CFD simulation. This may suggest that the 4% porous wall setting is more in line with the free-stream conditions used in all CFD simulations. This result is very god taken into account that the accuracy of the modelling of the flow though the engines will have a direct influence on this property.

Eight Kulite pressure transducers were installed on the wind tunnel model to provide point pressure data to compare with CFD (intakes, wing, aft part of the model close to the force balance). For the Mach 0.5 case a reasonable agreement is found for Kulites on the wing, while a bigger difference is found for the ones in the intakes. At higher Mach numbers a good match is often found at very low angle of attack, while the experimental value always experience a sudden increase with AoA that is not found in the simulations.
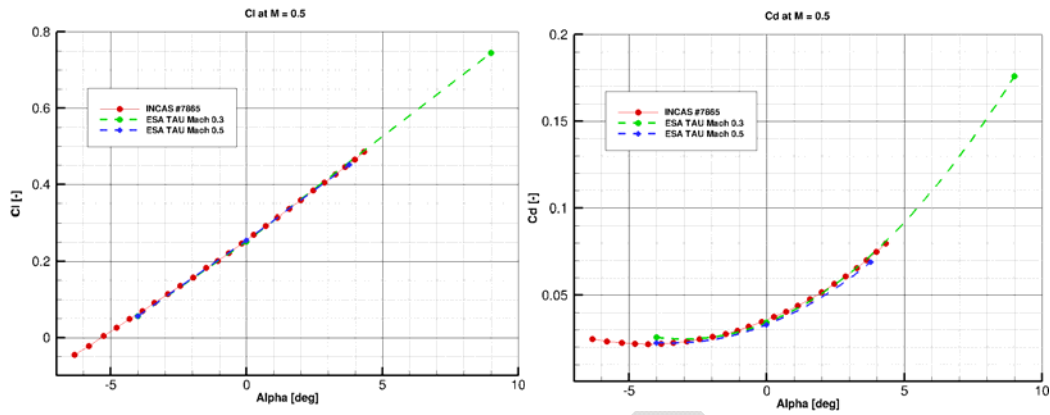
Figure 19: Lift coefficient (left) and drag coefficient (right) for the Mach 0.5 case (includes results of simulations at Mach 0.3)
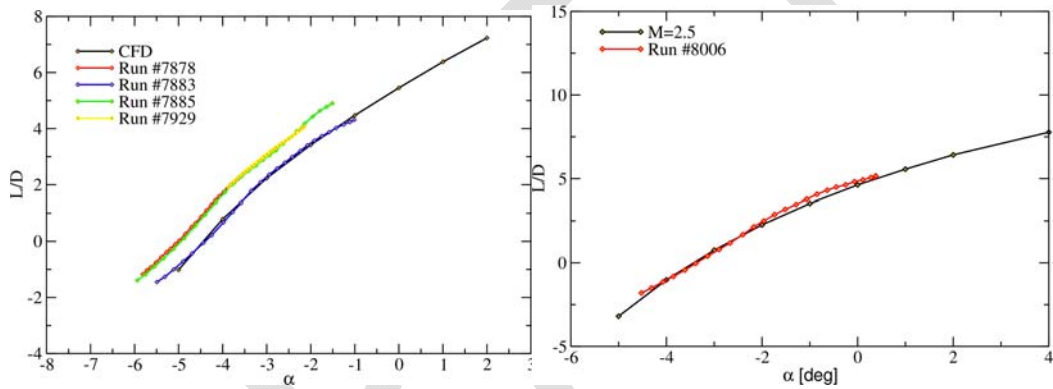

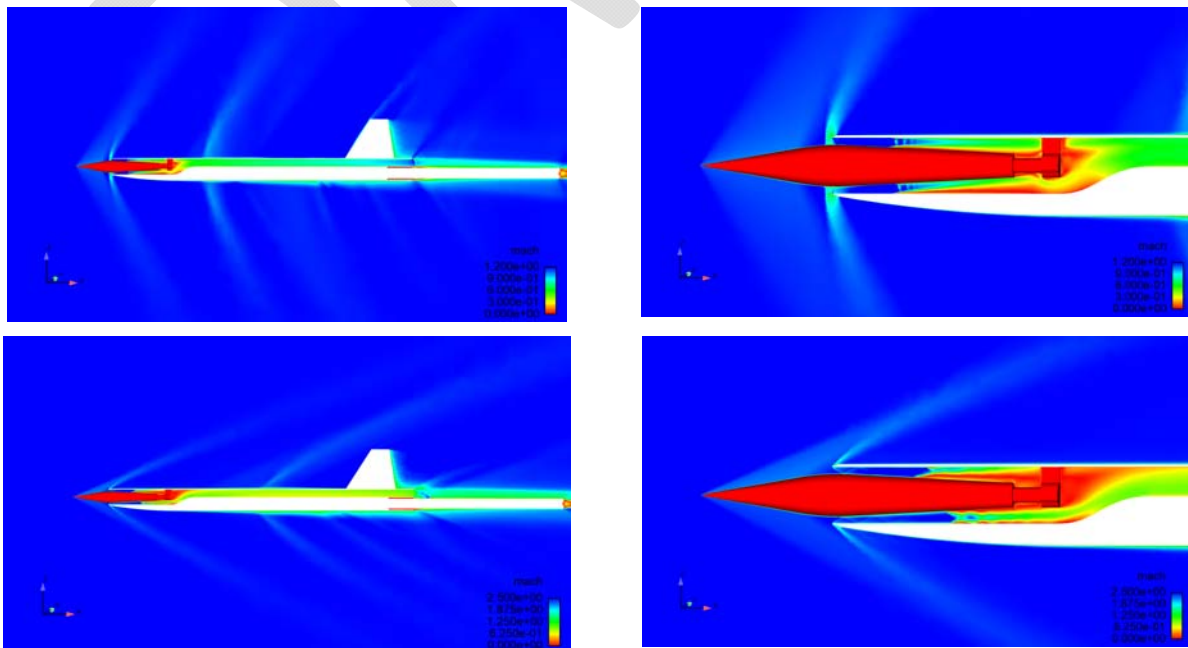**Figure 20: Comparison CFD simulated and WT data at Mach 1.2 and 2.5 (internal surface included)**

Figure 21: Flow visualisation of CFD simulation result at Mach 1.2, 1.6 and 2.5, α = 3°

2.5 Discussion

The main focus in ATLLAS-II WP 2 is to set the requirements for the material manufacturing, processing and testing. A fully integrated Mach 5-6 vehicle design taking into account several disciplines in the trade-off and optimization is foreseen. The general findings in WP2 are summarised below:

WP 2.1 Aerodynamics and propulsion:
- The analysis was extended to consider also the effect of venting an under-expanded exhaust into the base of the fuselage. The predicted cruise efficiency of this configuration is slightly lower than for a lee-side expansion analysed in ATLLAS-I, but has the advantage of separating the aerodynamics of the wing from the propulsive jet, thereby offering an alternative means of integrating the aerodynamic and propulsive flow fields
- Further investigations are needed to better understanding of the flow behaviour in general and especially of the internal flow path, viscous effects should be taken into account.
- For a given range: the faster one flies, the lower the integrated heat load: the heat flux has less time to penetrate into the structure. The faster one flies: the higher the external wall temperature but levels off due to the highly non-linear heat radiation
- The convective heat transfer doesn't increase with the power of 3, but rather flattens out at higher flight speeds
- Good agreement was achieved between CFD simulations and wind tunnel experiments
- Predicted cruise efficiency

WP 2.2 Structure, materials and thermal protection:
- The temperature at the base of the leading edge will be lower and metallic solution might be still doable for Mach < 4, but will be heavier and might require active cooling of panels (also heavier)
- CMC is preferred solution for Mach > 4. CMC promises good specific strength for extreme temperature applications. Oxidation, creeping, and fatigue issues remains to be a big challenge
- High emissivity is preferred
- Fatigue behaviour at high temperature may be rather different from the fatigue behaviour at room temperature for CMC materials considered. While the creeping property may limit CMC for the skin application, it is the structural random dynamic load that will dominate fatigue life of the TPS at high temperature
- The long duration of a flight dictates a proper thermal protection system to cope with the integrated heat load accumulated during flight while a part of this heat might need to be evacuated after touch-down.
- A cabin air-conditioning and auxiliary power cycle scheme was designed

WP 2.3 Environmental issues:
- For ICAO standard atmosphere with no turbulence, the sonic boom from ATLLAS II hypersonic configuration was calculated and the ground undertrack boom was estimated to 91 dBA (ASEL), in the same order as the Concorde (89 dBA) D2.3.6 [18] but with a peak at lower frequency. Width of ground geometrical footprint is larger than Concorde (136 km) because of higher Mach and higher altitude
- For ground track boom with turbulence, standard deviation is relatively high and positively skewed, indicating that there is a significant probability of high intensity peak pressure. For lateral boom in the shadow zone, peak overpressure is enhanced due to sound scattering by turbulence.
- For a traffic corresponding to 100 ATLLAS II baseline flights the results indicate a risk for ozone layer depletion

WP 2.4 Multi-disciplinary optimisation:
- Improved vehicle having better range, L/D and less weight
- Use of relevant constraints are extremly important
- From the evolution of vehicle weight as a function of time. it is clear that the original estimation of vehicle weight is significantly lower than the final weight
- The eigenfrequency constraint was identified as a strong design driver and should have caused more action
- For the future work, one should include also flight handling constraints, so that the eigenfrequency constraint could be removed.

A research plan from 2016 to 2025, including additional R&T and demonstrations was formulated D2.5.1 [28]. The development roadmap includes envisaged developments and demonstrations of different key technologies and systems that do not require flight testing before use on large scale A/C demonstration. Special emphasis is put on very long duration hot structures demonstrations. Finally, also develop and demonstrate in flight at small scale some critical technologies: high-speed powered flight, take-off and landing and transonic flight.

3   Aero-Frame & Materials Integration

Based on experiences made in ATLLAS I, lightweight airframe materials were supposed to be developed further with respect to long-term applicability. As materials are exposed to high thermal and structural loads (especially regions like nose structures, wing leading edges and air intakes), they need to be specifically tailored to this application. Hence, certain components demand for high specific strength, high ductility and toughness, increased oxidation resistance as well as high creep and fatigue resistance at elevated temperatures.

The focus within the current project was directed towards material design, investigation of oxidation resistant coatings and investigation of long-duration characteristics such as creep and fatigue properties, as recommended at ATLLAS I reviews. Following materials were under investigation along with their mechanical integration issues and their specific application.

- Titanium matrix composites (TMCs)
- Hollow sphere structures / tube stacking structures (HSSs/TSSs)
- Ultra high temperature ceramics (UHTCs)
- Ceramic matrix composites (CMCs)

In addition, feasibility and integration aspects of structures and materials were considered.

3.1   Titanium matrix composites

For titanium matrix composites (TMCs), a survey on published alloy data was performed where the need of creep data was detected. For this reason, cylindrical TMC samples were manufactured consisting of different titanium alloys (Ti-6242, Ti-834) as well as fibre-reinforced and monolithic samples. Thereby, the creep rupture was considered for tests from 1 to 1000 hours. Fig. 22a exemplarily shows some of the manufactured samples. During the manufacturing process, problems existed for those sample geometries. Hence, the samples were changed to a flat geometry, as shown in Fig. 22b. In the same manner like the cylindrical samples, they consisted of different titanium alloys (Ti-6242 vs. Ti-834) and fibre architecture (fibre-reinforced vs. monolithic). In the following, extensive investigations were performed for the different samples. As estimated, fibre reinforced TMCs showed significantly higher creep strength at tested temperature levels of 600°C using Ti-834 alloys. Furthermore, the enhanced performance of Ti-6242 vs. Ti-834 alloys was confirmed, see Fig. 23.
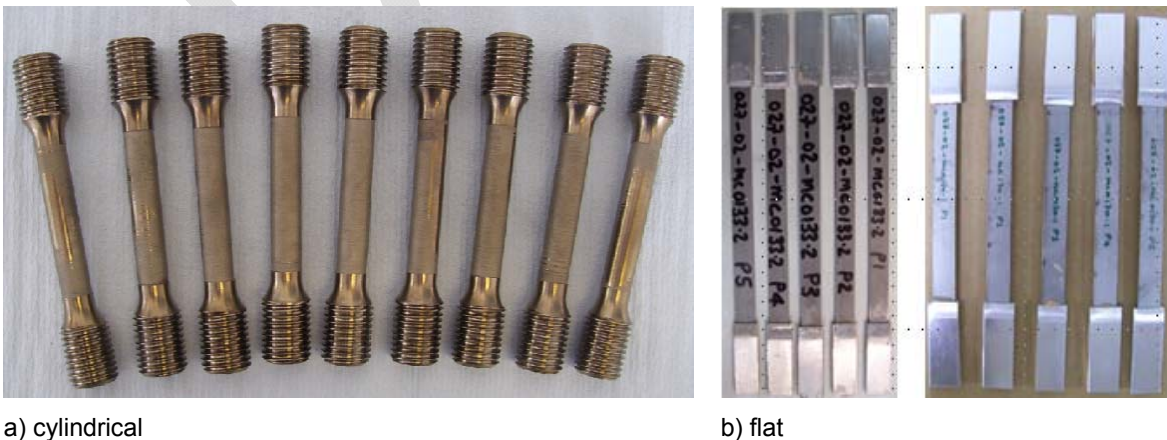

a) cylindrical   b) flat

Fig. 22: TMC creep samples
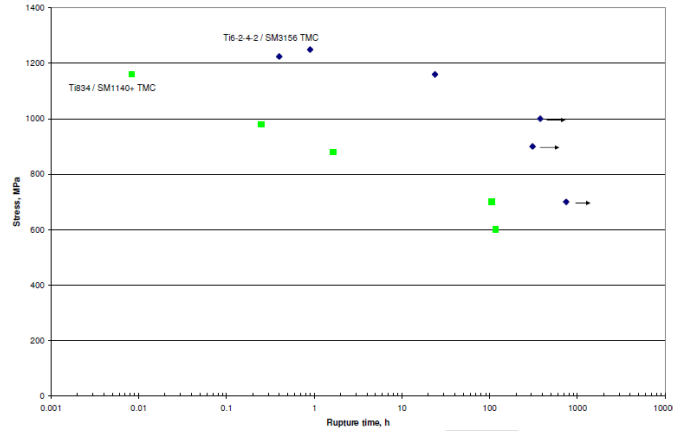
Fig. 23: TMC creep behaviour at 600°C (Ti-6242 vs. Ti-834)

The envisaged TMC material is intended for use in e.g. the rotation axis of a canard aerofoil. Due to impinging hypersonic airflow, the component could heat up to 1000°C and above. Aerodynamic forces induce bending loads, which result in tension and compression stresses within the material. It is therefore necessary to investigate the effect of combined thermo-mechanical loading. For this reason, thermo-gradient mechanical fatigue tests were conducted at DLR. As depicted in Fig. 24a, the thermal gradient is obtained by outer surface heating with an induction coil and simultaneously internal cooling with pressurised air. A steady-state thermal gradient is typically achieved after 20 to 40 seconds. The high energy input allows heating rates comparable to those e.g. in real turbine blades of a jet engine. Realistic cooling rates are achieved by forced air cooling from the inner bore of the specimens. The test cycle can be very short due to the high heating and cooling rates. Thus, the fatigue load of an entire flight mission can be imposed on the specimen within 3 to 5 minutes.

a) TGMF test setup

b) exemplary TGMF testing scheme

Fig. 24: TMC TGMF-testing

The loading sequence consists of inductive heating to high temperature, holding at high temperature, and cooling to low temperature. The thermal cycling is thereby synchronized with an

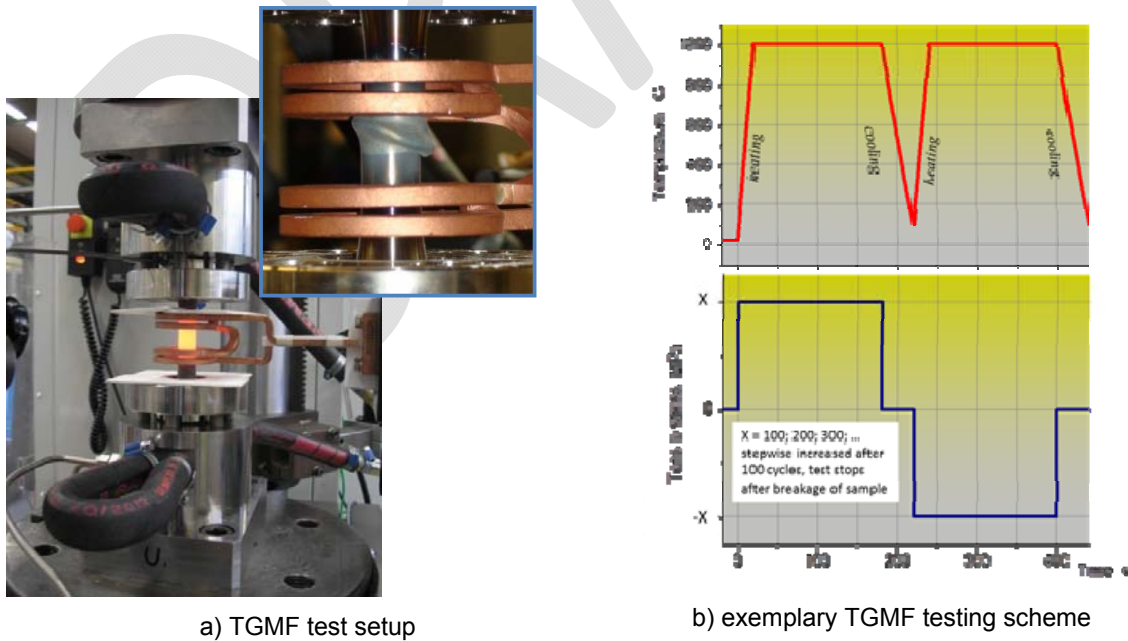applied cyclic axial force; see Fig. 24b. The maximum temperature will be kept the same for each specimen but varied in-between 500 and 1100°C. The mechanical loading will be increased stepwise in the case that the specimen survived a specific number of load cycles. Fig. 25 shows the numerical simulations performed to determine thermo-mechanical load distributions of the applied tubular TMC samples at specific temperature and stress levels.
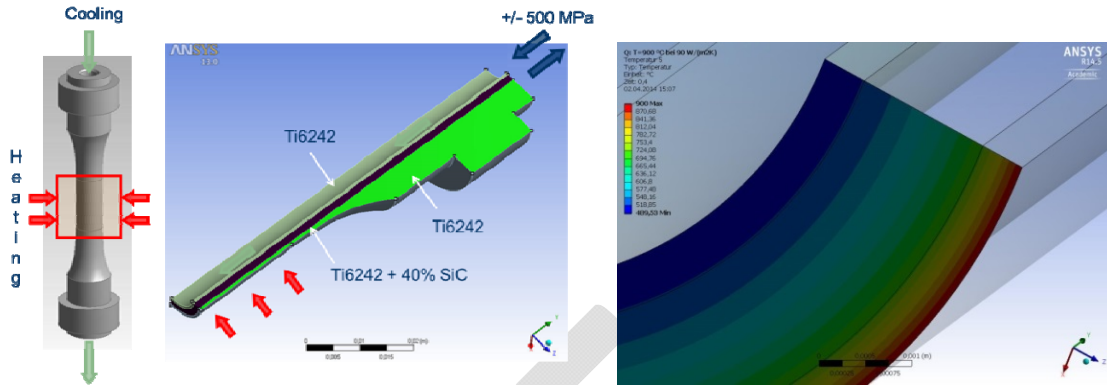
Fig. 25: TMC TGMF numerical simulation

By means of this testing procedure, the maximum allowed stress levels at different temperatures were obtained. In total, 11 of 15 fibre reinforced and 2 monolithic samples were tested, where temperatures up to 1000°C were reached. After each 10 cycles, the temperatures were increased by 100°C. The procedure was repeated until a failure was detected, which mainly occurred under compression, as indicated in Fig. 24(a).
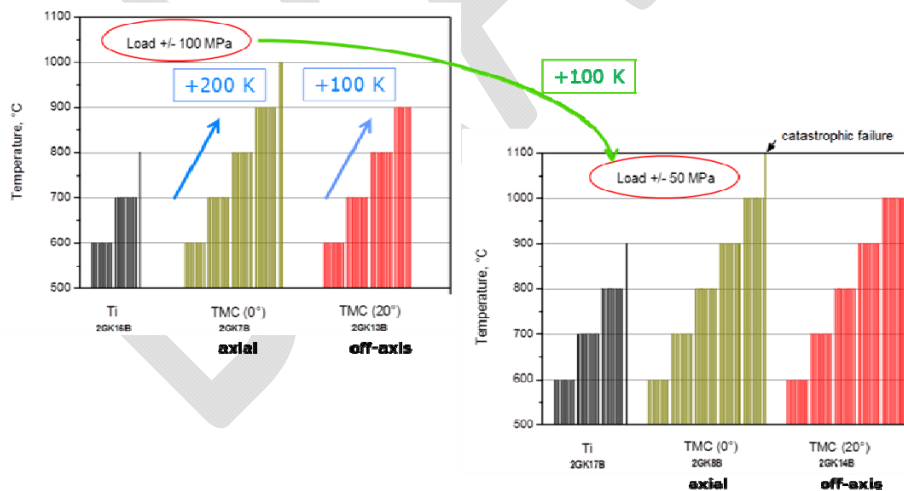
Fig. 26: TMC TGMF test results (black: monolithic Ti, green: axially reinforced TMC, red: 20° off-axis reinforced TMC)

Fig. 26 exemplarily shows some results for different stress (±50 and ±100 MPa) and temperature levels and various sample types: monolithic titanium (black), axially reinforced TMC (green) and 20° off-axis reinforced TMC (red). The influence of fibre reinforcement on the sample's strength is clearly visible. A fully axial reinforcement resulted in approximately 200 MPa higher strengths; an off-axis reinforcement exhibits a slightly lower fatigue strength as it would have been expected. Furthermore, the fatigue strength strongly depends on the applied alternating stresses as well; if

they are decreased from ±100 to ±50 MPa the same fatigue strength is achieved at approximately 100 K higher temperature levels.

Subsequently, TMC canard prototypes were considered for thermal testing at operational relevant conditions, .i.e. arc jet testing. Thereby, various leading edge radii of a TMC canard wing were investigated and numerically (CFD) simulated in order to assess the occurring thermal loads. A structural design was modelled and optimised by means of finite element analyses which included the optimisation of internal impingement cooling. This was necessary as initial computations indicated too high temperature levels exceeding the operational limits of titanium and TMCs. Thereby, impingement slit geometries and mass flow rates were tuned to achieve higher velocities and hence higher heat transfer coefficients; this in turn yields in increased cooling efficiency and lowered surface temperatures. Fig. 27 shows a typical slit geometry along with its resulting surface temperature trace is plotted; in this case, a pre-set limit of 1000°C was not exceeded (except point T1 was has to be considered as singularity due to set boundary conditions).
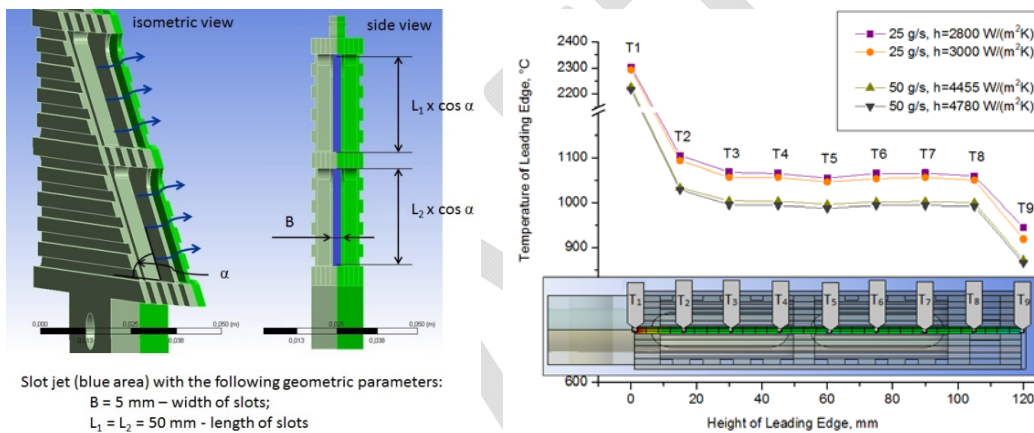
Fig. 27: TMC canard finite element analysis

Based on numerical results, TMC canard wing parts were designed and manufactured by TISICS. Based on previous performed simulation work, impingement cooling slits were integrated. At the outer skin of the canard leading edge, titanium matrix composite material (matrix and 0.4 mm Ti 6-2-4-2 monolithic cladding) was placed; such a fibre alignment allows transporting heat effectively away from the hot leading edge stagnation point. Thereby, the manufacture route included diffusion bonding of pre-form composite sections (Fig. 28a) to form a skin around a separate core, which allows for a cooling airflow. The final product can be seen in Fig. 28b.
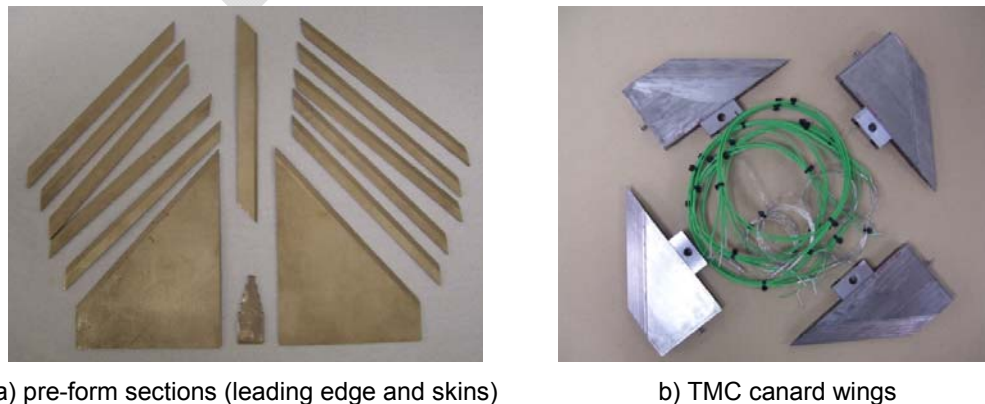
a) pre-form sections (leading edge and skins)   b) TMC canard wings

Fig. 28: TCM canard wing manufacture

Four canard assemblies were provided for thermal tests in DLR's arc jet facility L3K, see Fig. 28b. Two of them were made with a blunt leading edge radius of R0.8, whereas the others were manufactured rather sharp-edged. The TMC canard wings were integrated into a rectangular CMC plate and mounted on a model holder, as depicted in Fig. 29a, via a wing adapter which itself is mounted on the water-cooled base plate of the model holder. Internally, the canard was prepared for internal impingement cooling of the leading edge using air as coolant fed from exterior to an integrated plenum. After impinging through slits to the leading edge rear surface, the coolant flow was redirected beneath the outer skins towards the rear of the wing. For the final assembly the open space between the CMC cover plate and the baseplate was filled with insulation material. A photograph of the final assembly mounted in the test chamber of L3K is provided in Fig. 29b.
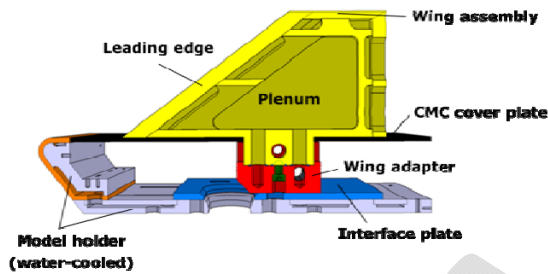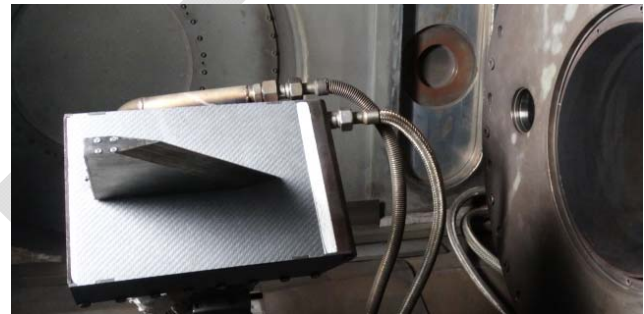

(a) TMC canard wings   (b) canard model setup

Fig. 29: TMC canard model

The tests were performed with air as working gas. With a total enthalpy 9.6 MJ/kg the facility was operated close to its low enthalpy limit in order to remain relevant for the requirements of hypersonic transport. The test condition were similar to the conditions used in the frame ATLLAS for aerothermal test on CMC leading edges.

The coolant system proofed stable operation during all tests of the campaign. Nevertheless, it did not reach the expected performance. Although designed for a flow rate of 50 g/s at maximal plenum pressure, only a flow rate of 20 g/s was achieved. During the tests, leading edge surfaces colours changed which came along with oxidation and slight erosion effects at the upper end of the leading edge (Fig. 30), where infrared system indicated temperatures up to 800°C. Both phenomena were assessed critical, hence the cooling was improved yielding in increased coolant flow rates of up to 30 g/s. Unfortunately, the cooling rates were still not sufficient to reach steady state conditions within the TMC's operational temperature range of 1000°C. Hence, the test duration was shortened to get at least an indication of the TMC canard performance.
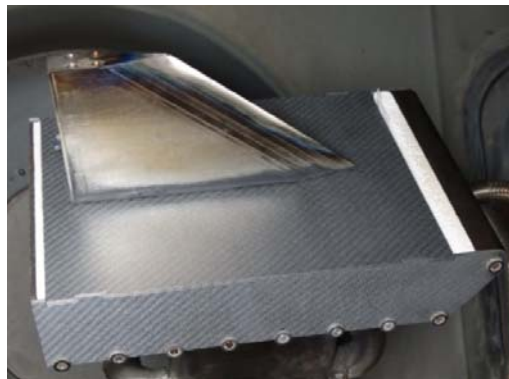

Fig. 30: TMC canard wing (final appearance)

## 3.2   Hollow sphere structures and tube stacking structures

Within the current project, HSS (hollow sphere structure) and TSS (tube stacking structure) materials were further developed by ONERA. The differentiation between HSS and TSS materials is mainly related to their intended use: HSS are rather randomly oriented and hence less predictable, but such materials are very favourable for parts of honeycomb like structures with acoustic damping abilities. On the other side, TSS are oriented, regular structures and therefore preferred from an industrial point of view. HSS materials exhibit a dedicated material behaviour in a well-defined direction, which is reflected by high oriented stiffness and energy absorption. Furthermore, due their regular nature, the simulation and characterisation of TSS based components is simplified as they can be considered as 2D.

With respect to material modelling, compression tests before and after oxidation treatments on TSS were performed. Thereby, TSS were brazed with various brazing materials and thermal treatment variants which resulted in a choice of optimised brazing process for materials of both high mechanical strength (at room and high temperature) and increased oxidation resistance. The elementary cells consisted of Inconel® 600 tubes. The brazing thermal process was performed at 1170°C for 15 minutes using a NiBCrSi braze.

As shown in Fig. 31, tensile tests on single tubes have been performed at elevated temperatures. It turned out that at room temperature and 600°C, the material's behaviour is mainly driven by plasticity effects. However at elevated temperatures of 800°C, the behaviour is governed by viscosity effects at the lowest strain rates; at higher strain rates the material tends to saturate and is then mainly driven by plasticity.
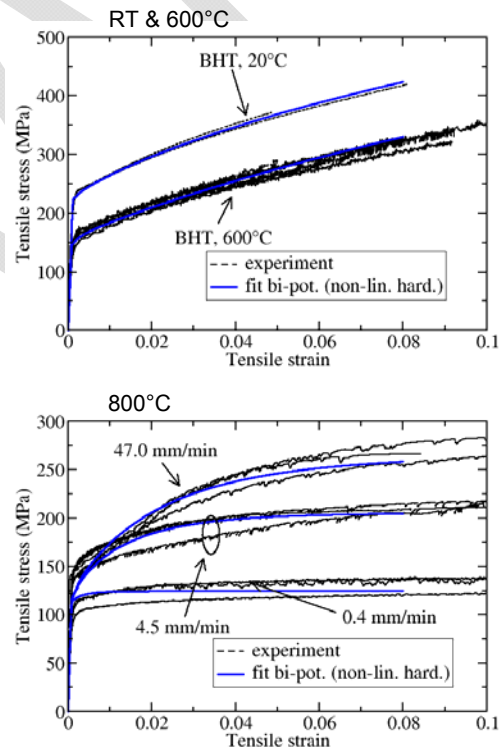
(a) test setup   (b) test results

Fig. 31: TSS single tube tensile tests at RT and HT

Furthermore, compression tests were performed for TSS at high temperature conditions within a vacuum furnace to avoid oxidation effects, as depicted in Fig. 32. An inverse traction-compression

setup was installed to improve the guidance of the compressive plate displacement. Optical access existed from outside so that the compressive plates displacement could be measured and digital images could be correlated to simulations. Three different temperature levels (RT, 600°C and 800°C) and two displacement rates (-1 and -0.1 mm/min) were considered for testing.

For these tests, only few geometrical defects were observed. The test reproducibility was quite good, whereas the scattering at room temperature is presumably related to some defects or non-parallelism of the skins. No effect of viscosity was detected at RT and 600°C, but at 800°C.

(a) test setup   (b) test results
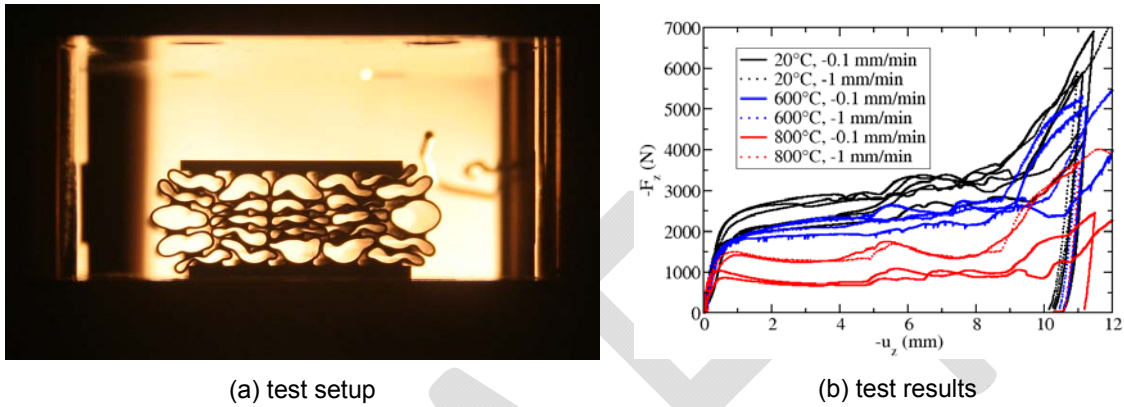
Fig. 32: TSS compression tests at RT and HT

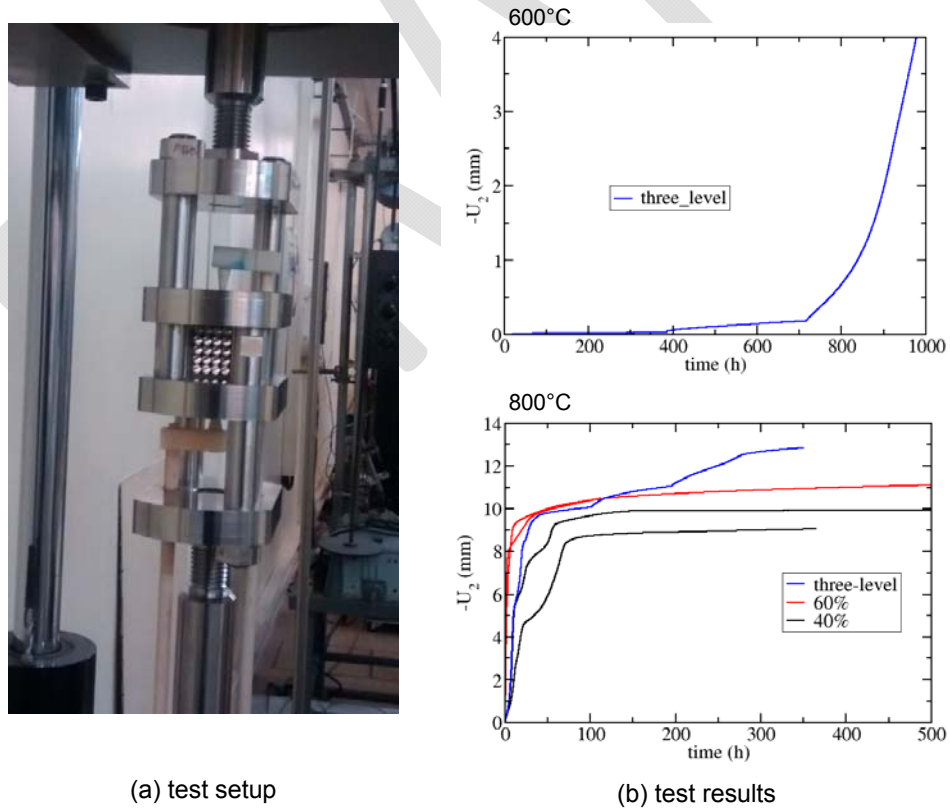(a) test setup   (b) test results

Fig. 33: TSS creep tests at HT

In addition, creep tests on TSS were performed at high temperature in air enabling oxidation effects, see Fig. 33. An inverse traction-compression setup was installed to improve the guidance of the compressive plate's displacement. No optical access existed. Two various temperature

levels (600°C and 800°C) were considered. At 800°C two different compressive stress levels (40% and 60% of the effective yield stress) were tested; furthermore, three-level compression test (40%, 60% and 80% of effective yield stress) was investigated at 600°C and 800°C, respectively.

At 600°C, only minor displacements were detected for the first two stress levels, but a sudden increase existed at the third level. This was expected due to the influence of localised plasticity (no viscosity). At 800°C, mainly viscosity effects contributed to the material behaviour but rather chaotic curves existed due to the buckling of the tube walls and the formation of new contacts.

Additional work on HSP materials was spent on the design and manufacture of transpiration cooled panel structures for tests at combustion relevant conditions at the METHYLE facility within WP4, see Fig. 34a. In terms of an assembly of cellular material and ceramic materials (Fig. 34b), two brazing solutions have been tested: dense or porous Al_2O_3 with Cu, and SiC with Ag. For both solutions, the addition of a TiAl sub-layer through PCT deposition process is necessary to ensure good wetting. Finally, a transpiration cooled HSS sandwich plate was manufactured, characterised and provided as a demonstrator.

Furthermore, investigations on the replacement of the extensive brazing process were initiated. For this reason, TSS made of stainless steel 316L were 3D-printed via the SLM (selective laser melting) technique and compared to conventionally Cu-brazed 316L tubes.

a) sketch for METHYLE tests

b) hollow spheres, tubes and Al_2O_3 skin
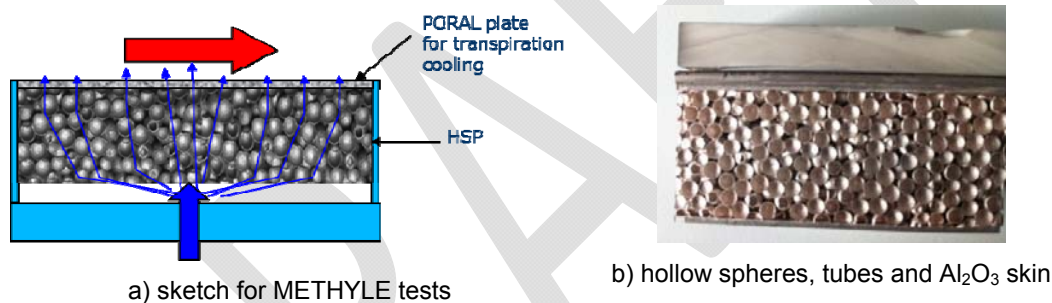
Fig. 34: HSP sandwich structure

Parallel to all before mentioned characterisation efforts, numerical simulations were performed to get an insight of the material behaviour at various operating conditions. As depicted in Fig. 35ab, small sandwich structures with a squared stacking of 5×5 tubes were considered. Thereby, the tubes had an outer diameter of 4 mm, skin thickness of 1 mm and mean braze joint width of 1.43 mm.

a) finite element mesh   b) compression sandwich samples
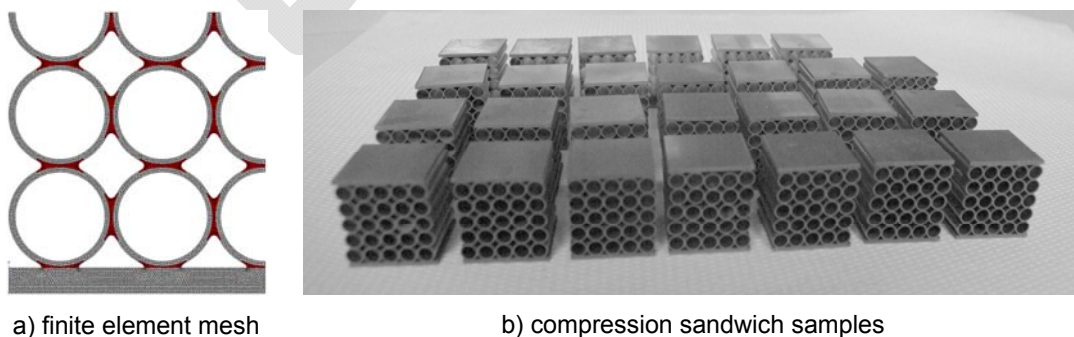
Fig. 35: TSS numerical modelling vs. experiments

The comparison of quasi-static compression tests (Fig. 36) showed a good agreement between numerical modelling and experiment being independent of the applied temperature levels. It can be

stated that strain rate effects were only detected at 800°C (experiments) but not at room temperature and 600°C.
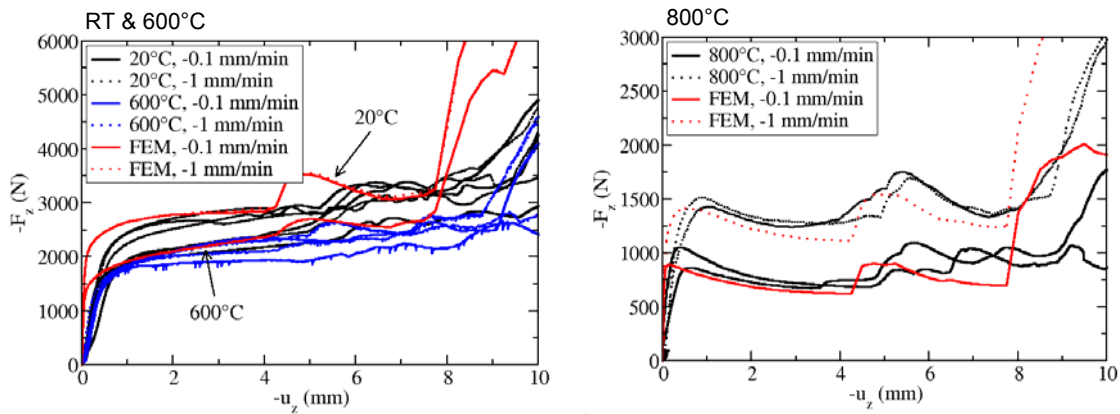
Fig. 36: TSS quasi-static compression tests (simulation vs. experiments)

Nevertheless, the comparison of creep compression tests (Fig. 37) showed some differences between numerical modelling and experiment results. As previously mentioned, creep tests were conducted following a three-stress-level approach. At 600°C, a slight displacement evolution exists during the second level, combined with a sudden increase in the third level; this may be contributed from plasticity effects which are not accounted for in the applied modelling. At 800°C, the numerical computation delivers good results compared to the experiments but unfortunately the simulation diverged before the third stress level.
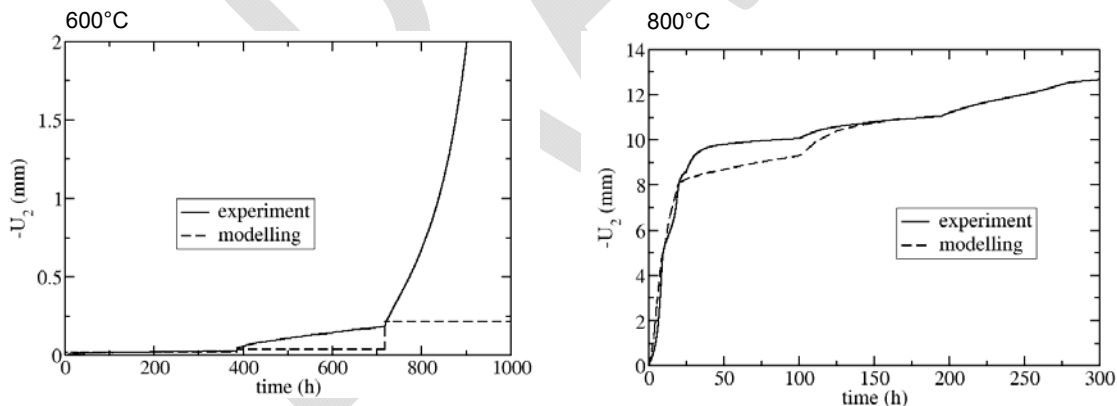
Fig. 37: HTS creep compression tests (simulation vs. experiments)

3.3 Ceramic matrix composites

Within the scope of this project, two different types of ceramic matrix composites (CMCs) were investigated by DLR: SiC/SiCN (non-oxide) and WHIPOX (oxide).

SiC/SiCN was manufactured via a PIP (polymer infiltration pyrolysis) process: SiC-fibre fabrics were infiltrated with a preceramic polysilazene precursor via a resin transfer moulding (RTM) process. After curing, plates were pyrolysed leading to a ceramisation (formation of SiCN) of the matrix. Ceramisation is intrinsically tied to a mass loss and volume shrinkage, which create pores in the CMC. To reduce porosity (which leads to a higher oxidation resistance), several re-infiltration and pyrolysis cycles were performed (in total six). The evolution of density and open porosity

during PIP-process is given in Fig. 12 (a). After six PIP-cycles, density and open porosity were ~2.3 g/cm³ and ~7.5 vol.%, respectively.

WHIPOX material is manufactured using computer-controlled winding techniques, whereas the winding pattern can be varied in a broad range. A Nextel™ 610 fibre bundle is infiltrated with water-based slurry. The infiltrated fibre bundle is pre-dried and wound-up on the winding mandrel. After the winding-process the wound bodies are dried or cut-up and removed from the mandrel. The sintering process is generally conducted at temperatures up to 1300 °C in air.

For the envisaged materials, samples have been prepared for

- oxidation resistance tests (arc-heated facility L2K and HVOF facility ERBURG[k])
- basic characterisation, only SiC/SiCN (tensile at room temperature, coefficient of thermal expansion, heat capacity, heat conductivity)
- extensive characterisation (4-point bending creep, tensile creep, fatigue, DNS, ILSS, tensile at high temperature, notch sensitivity)
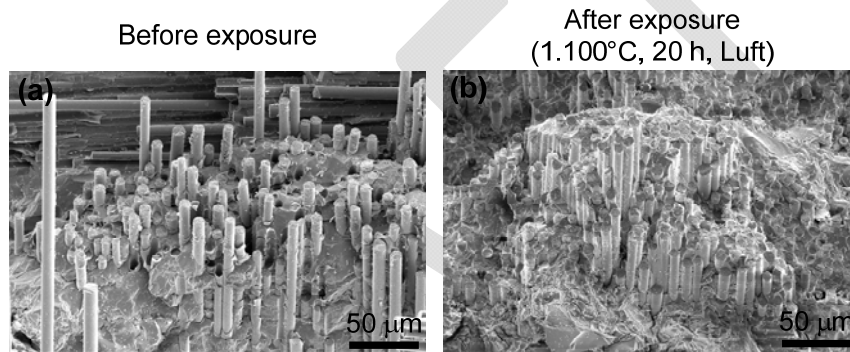
Fig. 38: CMC analysis; SiCpyc/SiCN fracture surfaces from bending tests

Basic thermo-mechanical properties of SiC_{pyc}/SiCN were determined before and after exposure to air (1100°C, 20 h). Before exposure to air, SiC_{pyc}/SiCN material exhibits high specific strength (tensile strength ~230 MPa) and high fracture toughness (strain to failure ~0.36 %), no abrupt failure after maximal stress in bending test. After air exposure however, strength and strain to failure decreased to appr. 30% compared to the unexposed case. The exposed material showed much more brittle fracture behaviour, which can be identified by less fracture toughness (less strain to failure) as well as less fibre-pullout as depicted in Fig. 38. Furthermore, SEM-micrographs indicated active (PyC-coating at temperatures >450°C in air) and passive (silica SiO_2 formation from SiC-fibres and SiCN-matrix at temperatures >800..1000°C) oxidation effects supporting SiC_{pyc}/SiCN embrittlement and strength degradation.

a) SiC_{LaPO4}/SiCN   b) SiC_{PyC}/SiCN   c) WHIPOX $CoFe_2O_4$ d) WHIPOX SiC
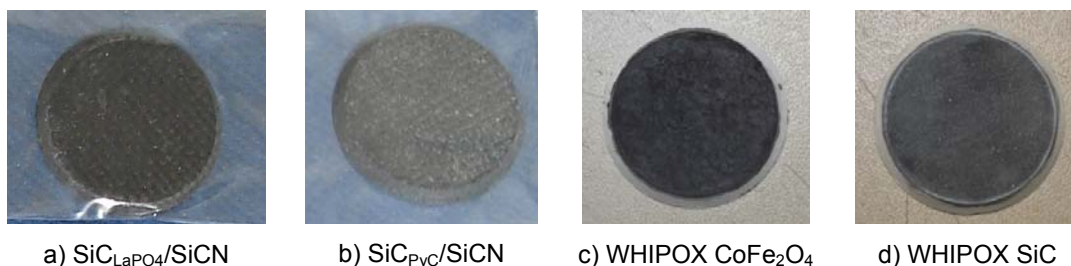
Fig. 39: CMC samples for oxidation tests in L3K
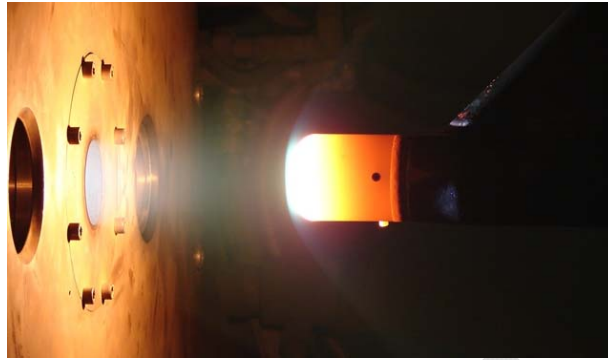
Fig. 40: CMC oxidation resistance test at arc heated facility L2K (SiC/SiCN at 1650°C)

In order to improve the material's oxidation resistance, the CMCs were additionally coated. For SiC/SiCN material (Fig. 39ab), the fibre coatings pyrolytic carbon (PyC) and monazite ($LaPO_4$) were applied to receive high fracture toughness with specific strength and an improved oxidation resistance, respectively. The same was done for WHIPOX material (Fig. 39cd), which was externally coated with silicon carbide (SiC) and a spinel based top coat ($CoFe_2O_4$) yielding in higher emissivity behaviour and oxidation resistance. To assess the oxidation resistance of the CMC materials, samples were prepared for tests at DLR's arc-jet heated facility L2K. Following, two test campaigns have been conducted for the coated CMC samples at temperatures up to 1650 and 1250°C for SiC/SiCN and WHIPOX materials, respectively. Fig. 40 shows exemplarily a test with a SiC/SiCN sample at a stagnation point temperature of about 1650°C. During these tests, both materials showed no major differences between each fibre coating and none to only minor cycling effects during the start-up phase of the tests. These tests indicated the high performance of SiC/SiCN materials but the detected mass losses demand to have an external EBC (environmental barrier coating) to withstand harsh oxidative environments. WHIPOX material exhibited nearly zero mass losses, however it was not comparable as it was tested at significantly lower heat flux conditions.

CMC materials are designed to be damage tolerant. A way to characterise this is to conduct tests with stress intensifying elements. For this reason, samples with artificial slot and holes geometries (Fig. 41) were prepared and tested for SiC/SiCN and WHIPOX. The tests indicated that both materials are insensitive or only poorly sensitive against such weakened regions.

Fatigue tests of WHIPOX at high temperature showed degradation effects of its stiffness and a development of hysteresis in the loading-unloading cycle. Based on current findings, a forthcoming failure cannot be predicted.
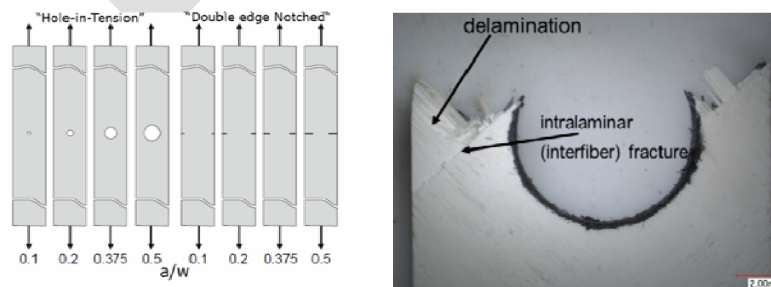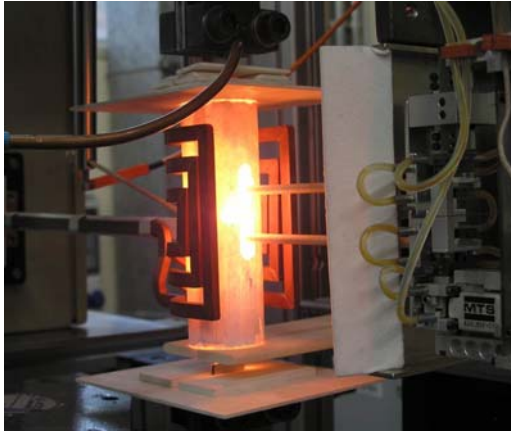

Fig. 41: CMC test on stress intensifying elements (right: WHIPOX)

Tensile tests on SiC/SiCN materials (Fig. 42) indicated a high strength of 244 MPa at room temperature. However, at elevated temperatures the samples tended to oxidise which resulted in a significantly decreased tensile strength; this is also due to a missing EBC coating.

sample #	strength [MPa]	ε max [%]	Temp. [°C]	
487-1 / 4SH129C	244	0.44	23 (RT)	
488-1 / 4SH134C	(≥82)	(≥0.18)	1000	Sample/platelets slipped
489-1 / 4SH139C	87	0.18	1200	
504-1 / 4SH149C	71	0.28	1000	
504-2 / 4SH150C	76	0.27	1000	
504-4 / 4SH152C	58	0.12	1200	
504-5 / 4SH153C	53	0.12	1200	

(a) experimental setup   (b) experimental results

Fig. 42: CMC RT/HT tensile tests (SiC$_{pyc}$/SiCN)

Like for tensile tests on SiC/SiCN materials, fatigue tests delivered similar results (Fig. 44). The fatigue strength at room temperatures is with about 200 MPa at a load cycle number of 10^5 very favourable. However, as for tensile tests at elevated temperatures, the fatigue strength tends to decrease to about 80 MPa at a load cycle number of 10^5 as the samples are being oxidised during the tests and no EBC was existent.

Fatigue testing of WHIPOX showed a distinct scatter in experimental results. Because of this, no reliable predictions can be made for load peaks beyond the linear-elastic regime.

(a) RT   (b) HT (1000°C)
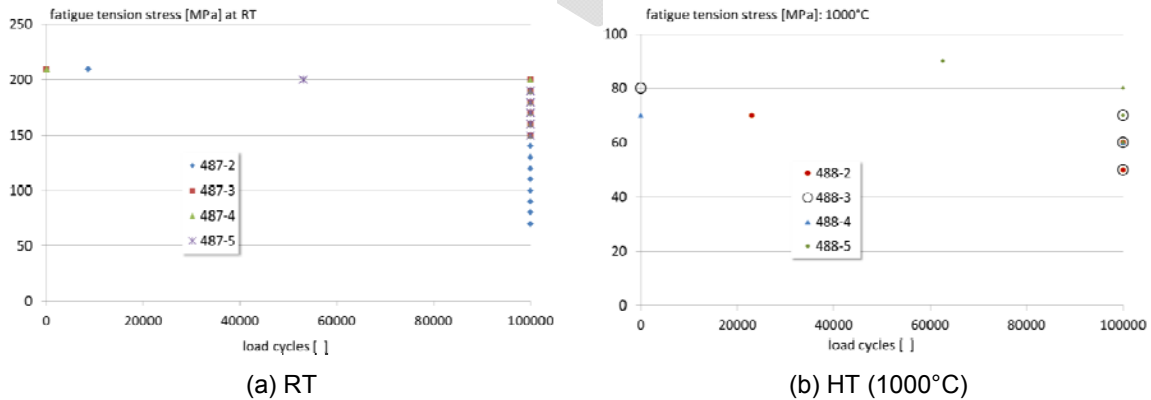
Fig. 43: CMC fatigue tests (SiC$_{pyc}$/SiCN)

Finally, long-running creep tests were performed on SiC/SiCN material, as seen in Fig. 44. Sample 506-1 could be tested at 1200°C with a stress of 20 MPa for 684 h until the furnace failed. At 300h creep time and 0.17% creep strain a steady state creep deformation was established with a creep rate of ~8·10-10/sec. Sample 507-1 was tested at 1275°C with the same stress of 20MPa. At 0.5% creep strain the load of sample 507-1 was increased to 40 MPa, but the sample failed 1 hour later, therefore no stress exponent could be derived from this. Sample 507-3 was tested at 1275°C with

a stress of 10 MPa. Based on the three characteristics, all Norton creep parameters were determined for SiCpyc/SiCN material which makes future creep predictions possible.
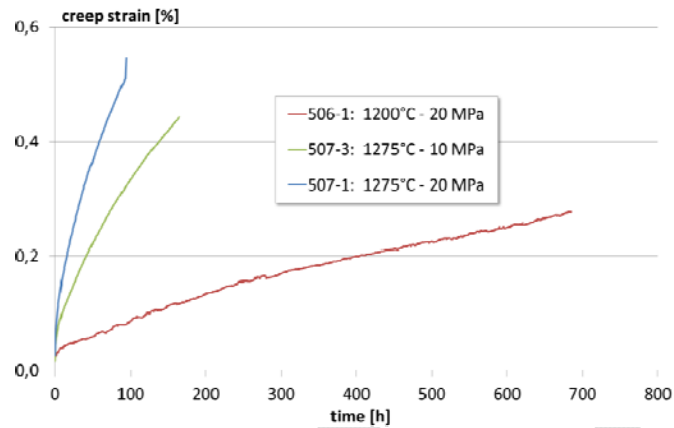
Fig. 44: CMC creep tests (SiC/SiCN)

It must be emphasized that oxidisation effects of the uncoated SiC/SiCN material will have its influence on the creep rates, but the quantity of the possible effect of course is unknown. This is being reflected for all high temperature tests on SiC/SiCN. In general, this material offers a very high potential for high-temperature and long-duration applications. However in future, an EBC becomes crucial for this type of materials in order to protect the material against hot gas infiltration.

3.4 Ultra high temperature ceramics

Ultra high temperature ceramics (UHTC) manufacturing efforts concentrated on the spark plasma sintering (SPS) method. ONERA manufactured monoliths for three different compositions:

1. ZrB_2 / 7.5% vol. SiC
2. HfB_2 / 20% vol. SiC
3. HfB_2 / 20% vol. SiC / 3% vol. Y_2O_3

First manufacturing trials were performed in the MATEIS facility (Lyon, F). For the manufacture of larger samples, further manufacturing was conducted at the ICB facility (Dijon, F). The achieved densities were quite promising as 96% of the theoretical density was detected. However, it was decided to skip the composition "ZrB_2 / 7.5% vol. SiC" due to a lack of process reproducibility and structural integration issues. Besides samples for extensive characterisation, bigger discs of 60 mm diameter and 12 mm thickness could be successfully manufactured. Such geometries enable to extract bigger parts as foreseen in other workpackages; Fig. 45 shows the sintered hafnium-based materials.

Fig. 45: UHTC Hf-based sintered discs

Diamond machining trials were performed via WEDM (wire electro-discharge machining) in order to check the feasibility of machining this material. In doing so, small-diameter holes and round-shaped (leading edge) geometries were successfully applied. Furthermore, several samples were machined for characterisation reasons, as can be seen in Fig. 46.
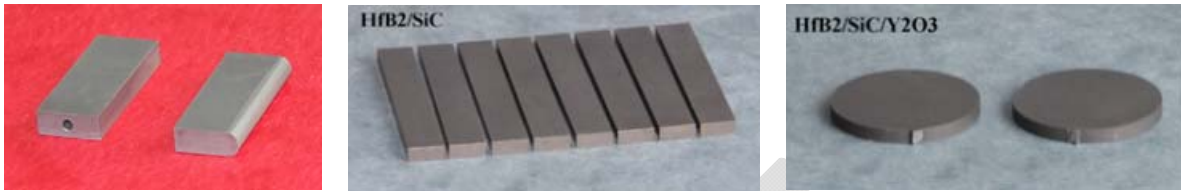
Fig. 46: UHTC EDM machined samples

The characterisation of UHTC material was conducted at various levels:
- Physical properties (densification state by water impregnation)
- Microstructure
    - SEM observations
    - X-Ray diffraction
- Mechanical properties
    - Young's modulus by impulse excitation technique
    - Flexural stress and modulus of elasticity at 20°C (bending tests)
    - Vickers Hardness
    - Fracture toughness
- Thermal properties
    - Coefficient of thermal expansion
    - Thermal diffusivity by laser flash technique
- Oxidation resistance
    - Thermogravimetric analyses at lab under air
    - Blox4 facility at ONERA
    - L2K arc-jet at DLR
    - METHYLE DMR test bench at MBDA
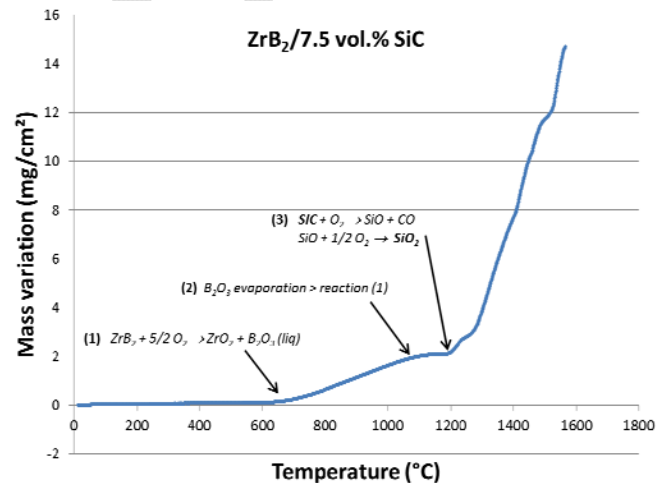
Fig. 47: UHTC TGA investigation for ZrB$_2$/SiC

For instance, thermogravimetric analyses up to 1550°C indicated multiple simultaneous mechanisms when ZrB_2/SiC material is exposed to oxidation effects in air atmosphere (Fig. 47): While the formation of ZrO_2, B_2O_3 and SiO_2 results in a weight gain, the vaporisation of B_2O_3, Si_2 and CO results in weight losses.

At the end, the oxidation resistance of selected UHTC compositions was investigated in the Blox4 facility at ONERA at various heat flux environments, see Fig. 48. Thereby, a CO_2 type laser with a power of 2 kW is used to heat up samples up to 2000°C surface temperature. The atmosphere can be controlled with respect to pressure and composition. For the current tests, the atmosphere consisted of 70% Ar and 30% H_2O. Typically, the samples have a diameter of 20 mm.
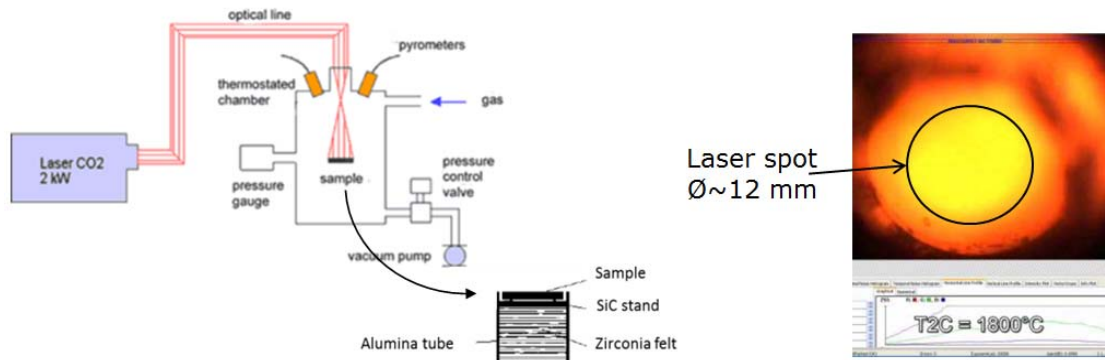
Fig. 48: UHTC oxidation resistance test bench Blox4

For Blox4 tests, all three UHTC compositions have been investigated with average laser fluxes of 4.8 to 7.2 MW/m² resulting in surface temperatures of 1800 to 2000°C. This is fully representative for operational heat fluxes of hypersonic airbreathing propulsion systems. Fig. 49 shows the appearance of some samples after different testing conditions and durations. Extensive microstructural analyses were connected to these oxidation tests. It could be observed that UHTC materials the formation of oxide layers (SiO_2 and HfO_2) on the outer surface and HfB_2-based layers in the core structure depends heavily on both heat flux levels, test duration and testing atmosphere.
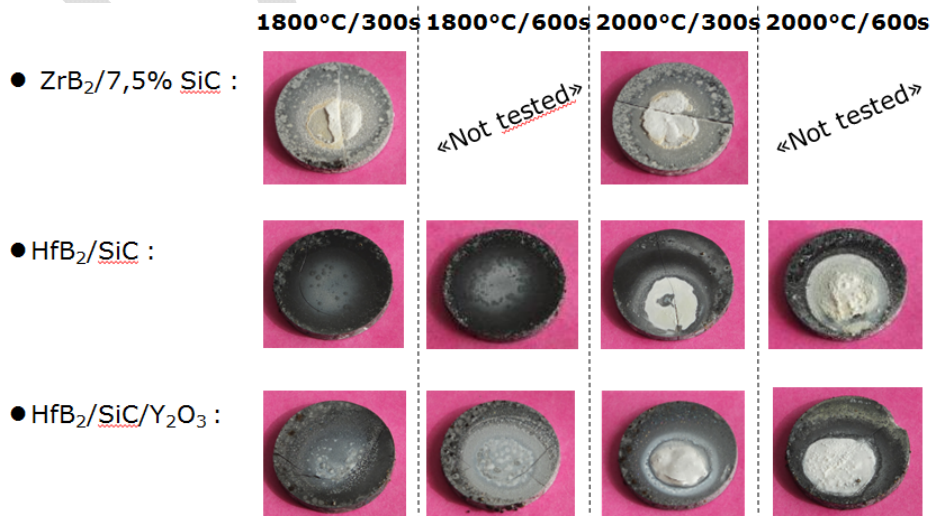
Fig. 49: UTHC Blox 4 sample appearance after tests

Besides CMC materials, UHTC materials were foreseen for strut injector components of ram- or scramjets. Therefore, tests in the METHYLE facility, a dual-mode ramjet test bench, were envisaged in WP4.3. Due to the SPS manufacturing process, UHTC materials cannot be manufactured in bigger sizes like other ceramics. Hence, it was considered to provide the pure strut injector part only. However, manufacturing trials were not satisfactory, as can be seen in Fig. 50a. Also, the dovetail connection along with its sealing concept shown in Fig. 50a was of high risk. Hence, the injectors were redesigned so that only the injector's leading edge section (being the most exposed region) was made from UHTC. For this reason, CMC base parts were additionally provided by DLR, as shown in Fig. 50b.

a) initial UHTC design   b) final design: UHTC leading edge with CMC base
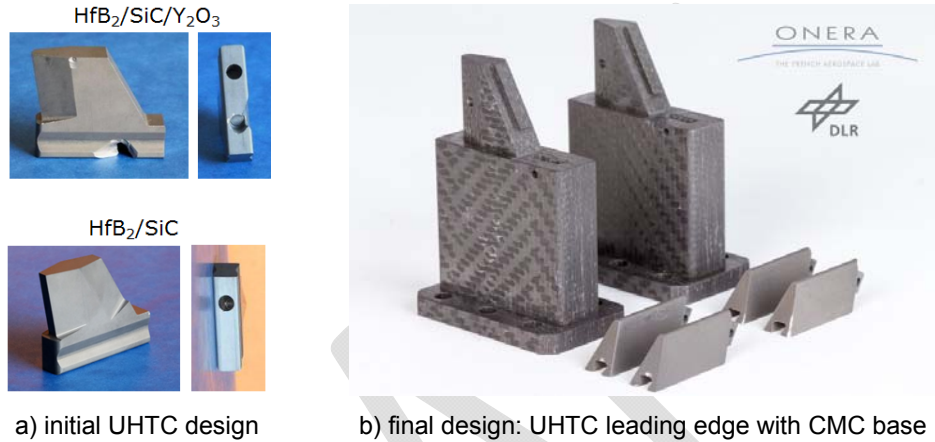
Fig. 50: UHTC strut injector manufacturing

3.5   Structures and Materials

With regard to sustained flight, a transferability study was performed by DLR on its SHEFEX II approach of thermal protection system (TPS) panels. It turned out that for the occurring aero-thermal and mechanical loads, this design approach is suited in general, but needs to be adapted to other boundary conditions. Environmental impacts were considered critical as there is only minor knowledge available: water-proof barrier coatings become necessary and different types of impact (bird, hail, lightning strikes) need to be considered for future applications. Additionally, dynamic fatigue tests need to be performed to identify weak spots as the current TPS approach which was designed for short-term (re-entry) applications only.

a) test article with laser displacement sensors   b) measurement locations
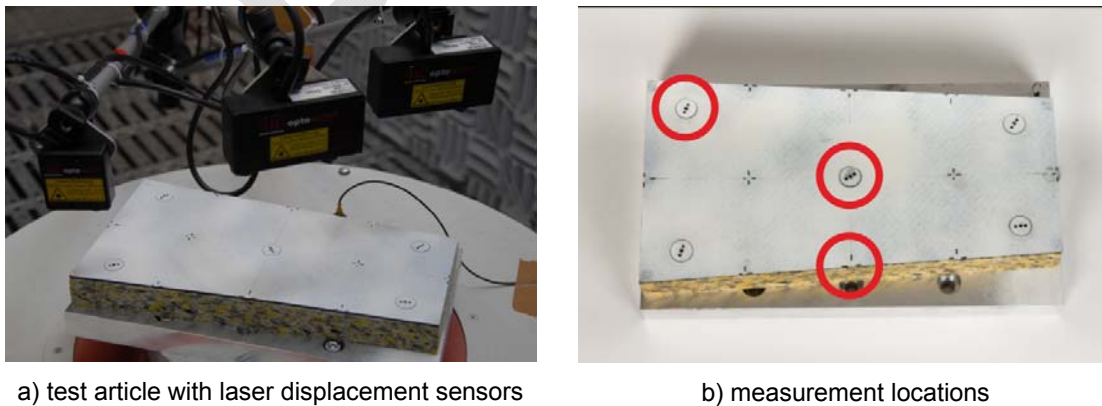
Fig. 51: Structures and materials – SHEFEX II TPS panel shaker tests

For this reason, a shaker setup was manufactured for the SHEFEX II TPS panel. Fig. 51a shows DLR's electrodynamic shaker facility with the installed panel setup installed for tests at room temperature. The input of these tests was analytically determined as there is hardly data available in the open literature. Thereby, a cone with a half angle 6° and length of 90 m was considered flying at Mach 6 at an altitude of 32 km. This resulted in the PSD spectra "Load 1", which can be seen in Fig. 52a.

Using this load spectrum, the setup was tested for about an accumulated 100 h test time, which corresponds to ~25 flights of 4 h duration each. It could be stated that after this test period, no change in structural response was measured (Fig. 51b; Fig. 52b) and hence no damage was existent. In a second test series, the load spectrum was doubled to "Load 2". After another 4 h test, a deviation of mechanical responses was detected and further testing was stopped as one connection got loose. Nevertheless, this did not result in any failure of the structural parts.

a) load spectra   b) measured response at start (15) and after 100 h (26)
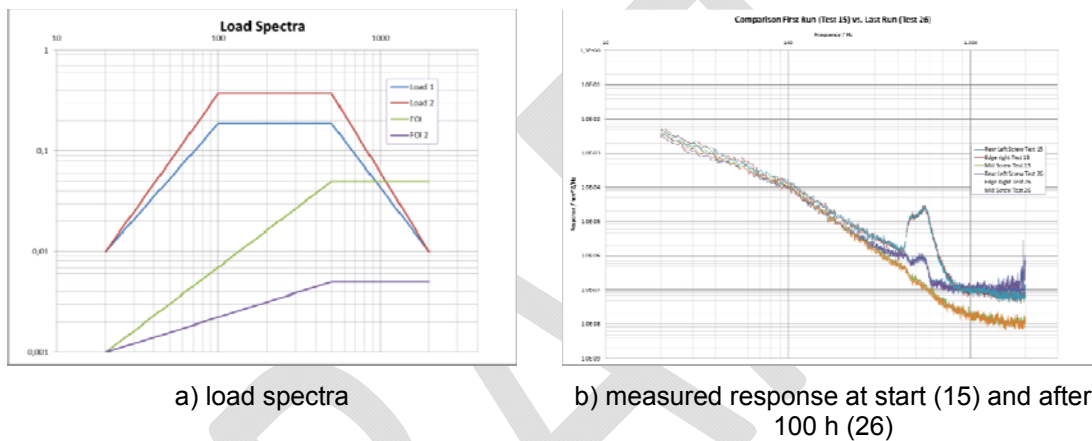
Fig. 52: Structures and materials – load spectra and results after 100 h

a) generic TPS panel model   b) SHEFEX II panel simulation
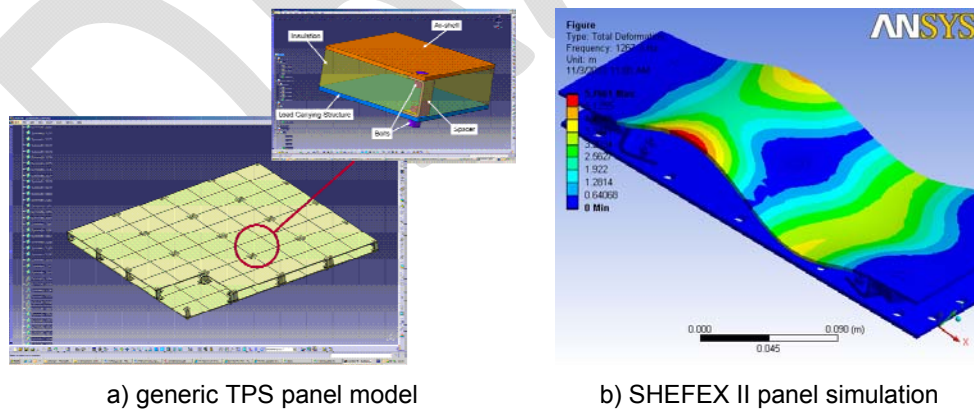
Fig. 53: Structures and materials – aeroshell connection

In addition, theoretical work on the connection of hot aeroshells to cold substructures was performed. Fig. 53a shows a typical setup of a generic TPS panel with integrated spacers, based on a symmetric finite element model. Thereby, ceramic composites were applied for components with extreme heat exposure. It turned out that the trajectory of hypersonic cruisers may be determined by the heat cycles to prevent severe thermal shock to the structure. The heat protection layer may be significantly thicker than that of the re-entry vehicles due to the prolonged exposure to the high heat input. Extensive grounding time may be required to prevent excessive over heating in the sub structures for the following flight. This may put a limit on the total economy

of vehicle operation. Those investigations were continued whereby the SHEFEX II setup was simulated based on a modal approach, see Fig. 53b.

Furthermore, the contribution of single TPS systems to the overall global stiffness was considered as well; a top-down conceptual approach was considered here.

3.6   Discussion

Based on experiences made in ATLLAS I, lightweight airframe materials were supposed to be developed further with respect to long-term applicability. As materials are exposed to high thermal and structural loads (especially regions like nose structures, wing leading edges and air intakes), they need to be tailored for this application. Hence, certain components demand for high specific strength, high ductility and toughness, increased oxidation resistance as well as high creep and fatigue resistance at elevated temperatures.

The focus was directed towards material design, investigation of oxidation resistant coatings and investigation of long-duration characteristics such as creep and fatigue properties, as recommended at ATLLAS I reviews. Following materials were under investigation along with their mechanical integration issues and their specific application.

- Titanium Matrix Composites (TMCs)
- Hollow Sphere Structures / Tube Stacking Structures (HSSs / TSSs)
- Ultra High Temperature Ceramics (UHTCs)
- Ceramic Matrix Composites (CMCs)

TMCs were manufactured and tested at realistic, operational relevant conditions. Here, the focus was to push the limits for high thermal and mechanical loading environment. TMC materials were characterised at such testing conditions in a TGMF (thermo-gradient-mechanical fatigue) facility. These tests were accompanied by corresponding finite element analyses. Furthermore, a generic leading edge canard wing was designed including internal impingement cooling and a TMC-based design. TMC canard manufacturing routes were assessed and four canard wings were and provided for arc jet tests. Finally, tests were conducted in the arc-jet heated facility L3K to assess to identify the feasibility of such TMC-based components at increased heat loads. However, it turned out that the applied impingement cooling was not sufficient to achieve steady-state conditions.

– It becomes therefore important to consider effective cooling techniques for potential future TMC-made components.

HSS and TSS materials were manufacture and thoroughly characterised at both room and high temperature conditions, with a special focus on creep compression behaviour. New high-temperature architectures in form of TSS were considered; this resulted in sandwich like structures capable for different applications. The numerical simulation of such structures was further optimised using quantitative constitutive material data which enabled an enhanced prediction of such structures.

– The switch from random to regular oriented structures enables to better predict such structures; the use of tube structures corresponds to quasi 2D-extruded structures with a favourable, distinctive material behaviour.

As **CMC** materials, SiC/SiCN and WHIPOX were manufactured and thoroughly characterised for basic thermo-mechanical and damage tolerance behaviour at both room and high temperatures. For life-time prediction reasons, dynamic fatigue and creep tests were performed as well. Furthermore, the material's oxidation resistance was investigated in the arc jet facility L2K and in the atmospheric burner rig ERBURIG[k].
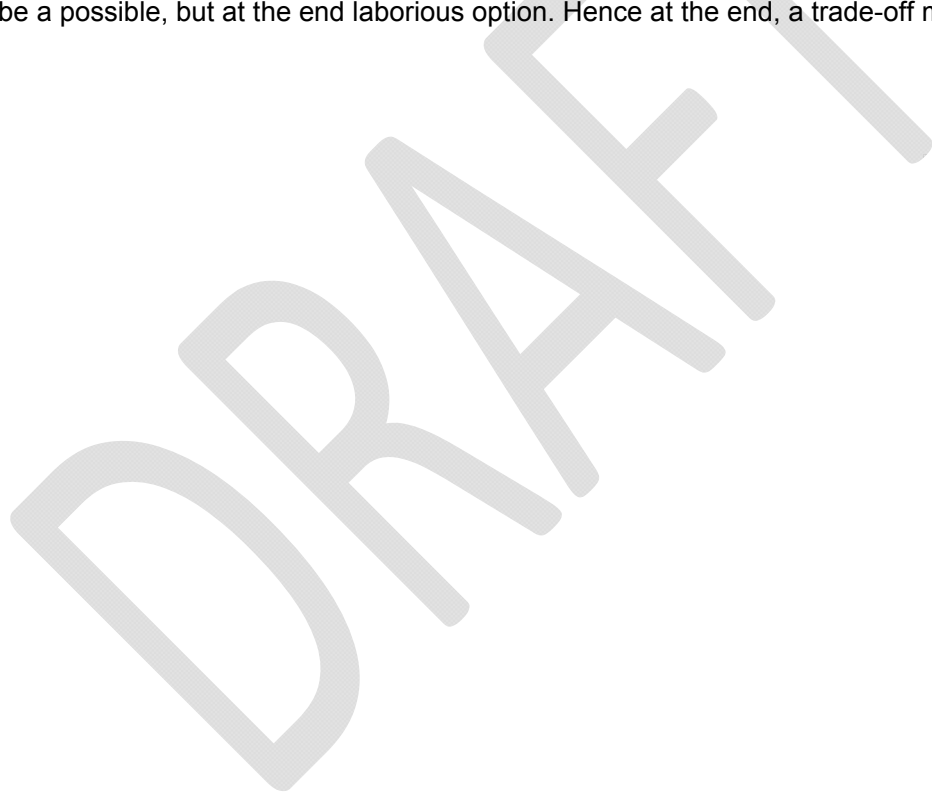
– SiC/SiCN materials indicate an excellent performance; for long-term applications however, the material demands for a sophisticated EBC to improve its oxidation resistance. WHIPOX proved to be applicable for long-term applications in the medium temperature range up to 1200 °C.

The selection of **UHTC** candidate compositions was finalised; three different compositions were thoroughly characterised. Furthermore, bigger sample geometries were manufactured and the feasibility of UHTC was proved in operational relevant conditions, such as the BLOX4 and METHYLE facilities.

– In order to increase their operational feasibility, it would be worth to think about reinforced UHTC materials in future to increase their damage tolerance behaviour.

For **structures and materials**, a TPS panel was set-up was tested at a shaker facility at room temperature. The tests performed successfully proved the feasibility for long-term applications of up to 100 hours, corresponding to about 25 flights of 4 hours flight duration each at Mach 6 and cruise altitude of 32 km. Within an accumulated test time of 100 hours, no failures were detected. In addition, theoretical work on the connection of hot aeroshells to cold substructures as well as on the contribution of single TPS systems to the overall global stiffness was considered.

– Small TPS panels successfully proved their applicability for long-term application. For realistic hypersonic cruiser vehicle lengths however, bigger panels may become necessary which come along with increased thermal expansion effects and manufacturing issues. Reducing the TPS size would be a possible, but at the end laborious option. Hence at the end, a trade-off must be found.

4   Combustor and Material Integrations

The deliverable concerns the overview of the Combustor and Material Integrations investigated in a generic way and in relevant testing environment or detailed analysis. These technologies can be used in a high speed airliner, supposed in ATLLAS2 to fly at Mach 5 or 6 with hydrocarbon fuel. Examples of these aircraft studied in WP2 are given on the figure below:

Generic ATLLAS1 vehicle (Mach 6 : Ti0 = 1650K)

Generic ATLLAS2 vehicle (Mach 5.1 : Ti0 = 1200K)
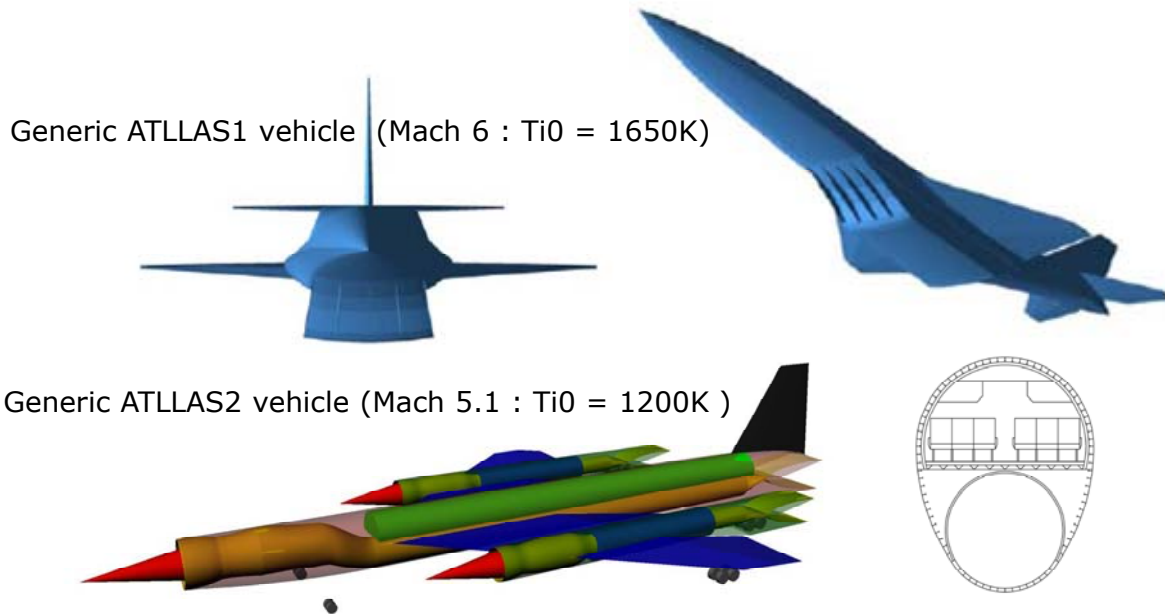
Figure 1 : generic high speed aircraft projects used for technology guidance in ATLLAS projects

5.1   Objectives and tasks of WP4

The objective is to study material and structures for combustors and advanced hot structures

The work package WP4 is split up into 3 tasks dealing with:

  4.1. Durability for Combustion loaded Non-Metallic Liners

  4.1.1 Flat samples and PTAH-SOCAR axisymmetric samples in long duration test in ERBURIG^K test facility

  4.1.2 Permeability measurements in addition to existing characterization of these porous structures

  4.1.3 Pin fin channel well documented

  4.2. Durability for Combustion loaded Panels with Metallic Cores

  4.3. Integration and Testing of (Un)Cooled Injectors (CMC or UHTC material)

WP4 work is connected with the other work packages of ATLLAS-II: System studies from ATLLAS-I and WP2 results of ATLLAS-II will be used as guidelines to define the architecture and the test condition of WP4 samples. WP4 will use the materials enhanced and characterized in WP3. WP4 will provide an interesting data base for numerical simulations in WP5.2. For possible application on the WP4 structures on the future high speed airliner, a dedicated meeting was organised during PM8 with actors from WP2, WP3, WP4 and WP5. The scheme below summarized its results.

nose   Leading edges   rudder

Fuel (kerosene) tank   aftbody

fuselage   wing

intake

canards

elevator

Internal nozzle

Movable ramp for throat

Circular « transfer duct »   combustor

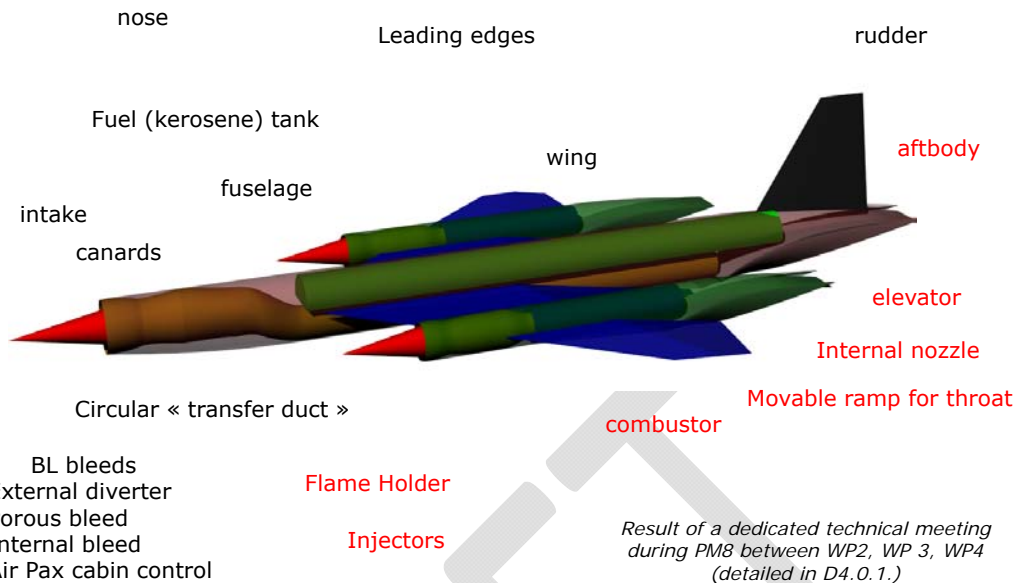BL bleeds
- External diverter   Flame Holder
- Porous bleed
- Internal bleed   Injectors
- Air Pax cabin control

Result of a dedicated technical meeting during PM8 between WP2, WP 3, WP4 (detailed in D4.0.1.)

Figure 2 : system studies as a guideline for structures to be used in different sub-systems

WP4 material and structures investigated in WP4 will be tested in laboratory then in actual environment : long duration test in the ERBURIG[K] test facility in Airbus Group Innovations (Germany) and industrial METHYLE dual-mode ramjet test facility in Bourges (France).

These tasks allow to experimentally and numerically investigate, in a generic but relevant way, different combinations of materials and cooling techniques, as summarized in the following section.

5.2   Different advanced technologies with future applications

Material and structures for combustors and advanced hot structures within ATLAS2 allow to investigate:

- Different **structures** (pin fin, injectors, uncooled CMC, HSS panel…)
- Different **cooling techniques** (pin fin, convective, transpiration, radiative)
- Different **materials** (metallic foams and skins, CMC including PTAH-SOCAR, massive UHTC)
- Different **test environments** (from lab to industry engine, from isolated phenomena to full real complex)
- Different **level of test documentation** (instrumentation)
- Different levels of pre-test and post-test **computations** (engineering, CFD…)
- Different **durations** (but generally minutes to hours)
- Different **applications** on future high speed airliner.

The following table and figure illustrate in a synthetic way the different systems and materials investigated.

Table 1 : list of material and structures successfully investigated in WP4

Type	cooling	Material	Technique	In ATLLAS1	In ATLLAS2	Status at end of ATLLAS2
Pin fin channel	convective	CMC	PTAH-SOCAR	PSR at TUM	PSH at ERBURIG long duration	Test finished on 4 ducts (PSH1 to PSH4)
		perspex	generic	computations	Detailed basic experiment	Tests and CFD performed
Injection struts	Transpiration Convective*	CMC	/	none	METHYLE Industrial TF	5 injectors sucessufully tested in METHYLE with CH4/H2 combustion
	convective	UHTC	/	Material sample	USTUTT (academic) METHYLE (industrial)	2 injectors with UHTC leading edge tested with success in METHYLE with CH4/H2 combustion *USTUTT test no more relevant*
External wall	None (radiative)	**CMC**	different	Material charac.	ERBURIG flat plate test + METHYLE* + IR lamps*	IR lamps performed and analysed Sucessfull test of CMC panel performed in METHYLE
HSS panel	Transpiration /convective	metallic	Porous hollow spheres sandwich	HSS manufacturing	METHYLE industrial TF + IR lamps*	IR lamps performed and analysed Sucessfull test of HSS panel performed in METHYLE with 2 different coolant rates

* : test series not planned initially

The design structures were tested with different levels of environment representability on one hand and instrumentation on the other hand, as sketched below.
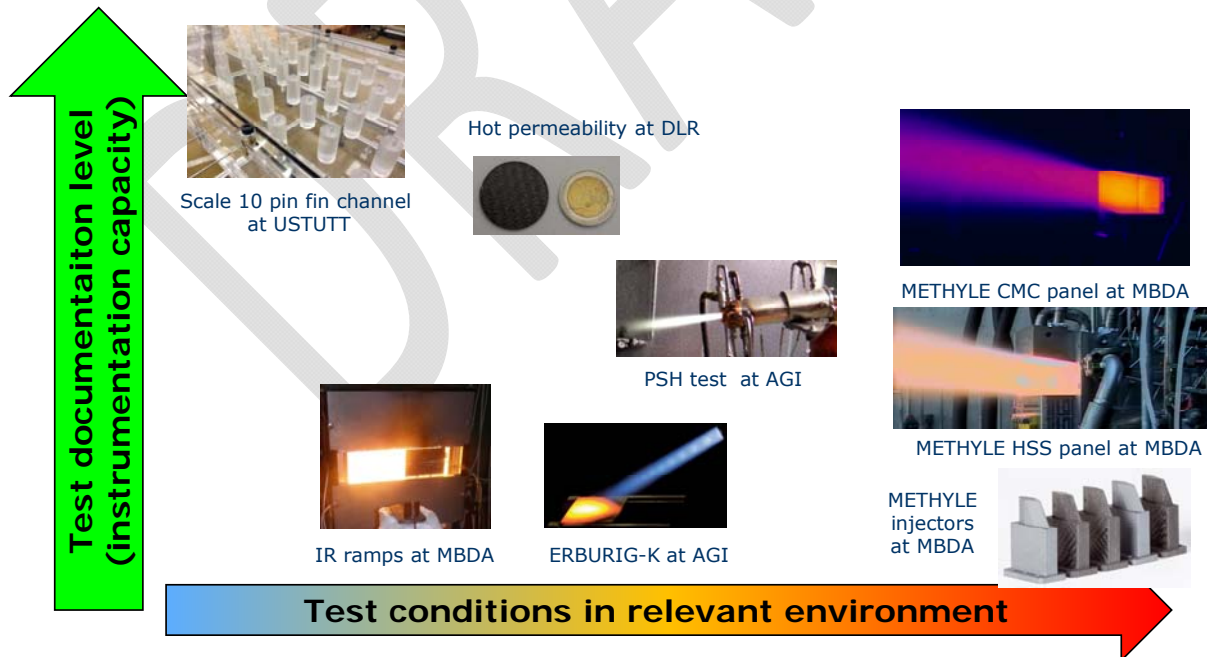

Figure 3 : testing chart for Combustor and Material Integration in ATLLAS2

The WP4 test series were prepared and analysed with design tools and with respect to possible use in high speed combustion environment and integration.

The WP4 tasks lead to intensive design of generic components and relevant successful testing, mostly realized in period 2 and period 3.

The benefit between previous ATLLAS1 program and current ATLLAS2 results is summarized in Table 1 and detailed in the following sections.

5.3   Pin fin channels

This technique is already used by heat exchangers, turbomachinery components, PTAH-SOCAR composite monobloc technique. Its application on future high speed airliners mainly deals with zones in contact with high heat fluxes from combustion process, and possibly in some other areas like hot boundary layer bleeds (Figure 4).

The work performed in ATLLAS2 in this area allows to significantly increase the scientific know how in two directions:

- Long duration testing of CMC cooled structures where pin fins in the cooling channel are generated by perpendicular stitching

- Detailed documentation of pressure drop as well as local heat transfer of staggered pin fins channels.

nose
leading edges
rudder

Fuel (kerosene) tank

wing

aftbody

fuselage

intake

canards

elevator

Internal nozzle

Movable ramp for throat
combustor

Circular « transfer duct »

BL bleeds
- External diverter
- Porous bleed
- Internal bleed
- Air Pax cabin control
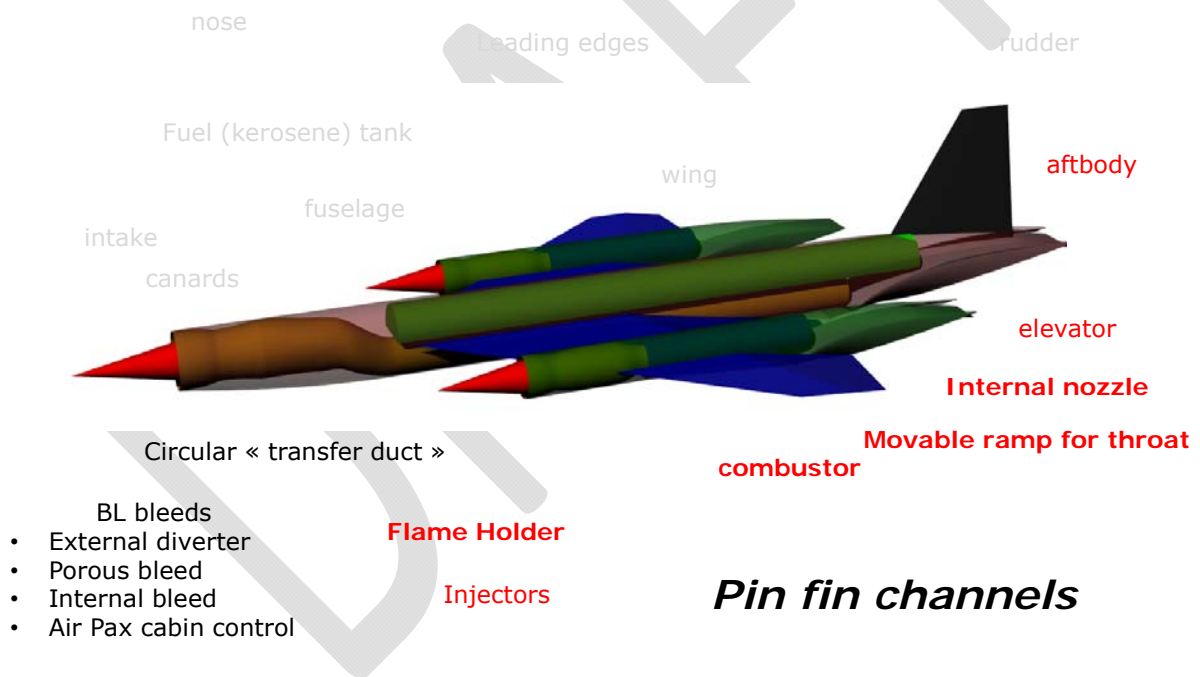
Flame Holder

Injectors

Pin fin channels

Figure 4 : synthesis view of pin fin channels possible use of high speed airliner

A unique experiment with warm air and perspex channel, associated with advanced measurement techniques, was set at University of Stuttgart.
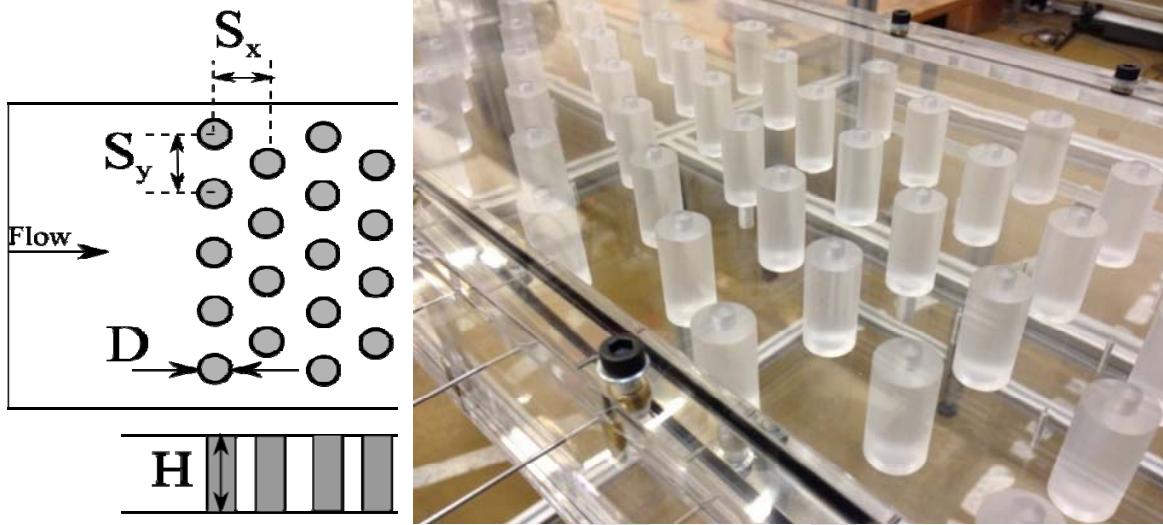
Figure 5 : pin fin channel at USTUTT and pattern definition

Three different channels were defined with different X/D – S/D – H/D geometrical parameters, summarized below:

Figure 6 : different pin fin patterns in 2D channels investigated at USTUTT

The detailed experimental work allows to document a huge amount of data on pressure drop, wall heat transfer, pin fin local heat transfer.

Figure 7 : example of measured heat transfer coefficient map in pin fin generic channel

Figure 8 : Instrumented aluminium pin fin

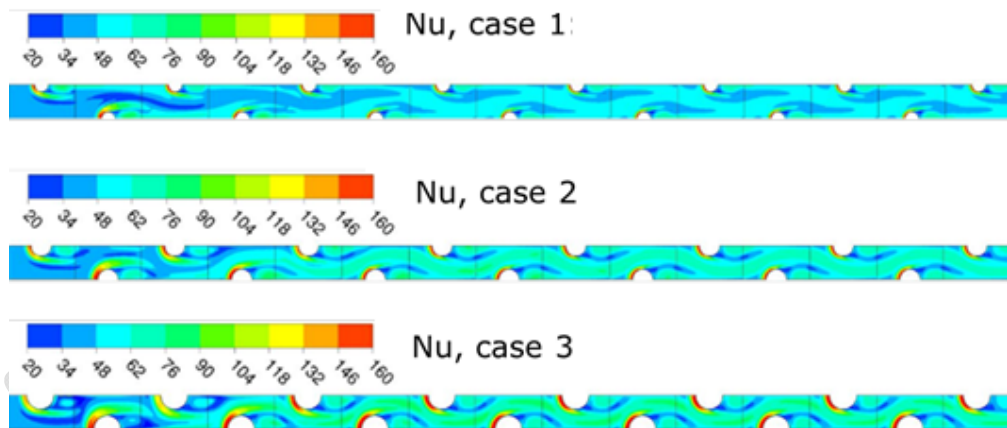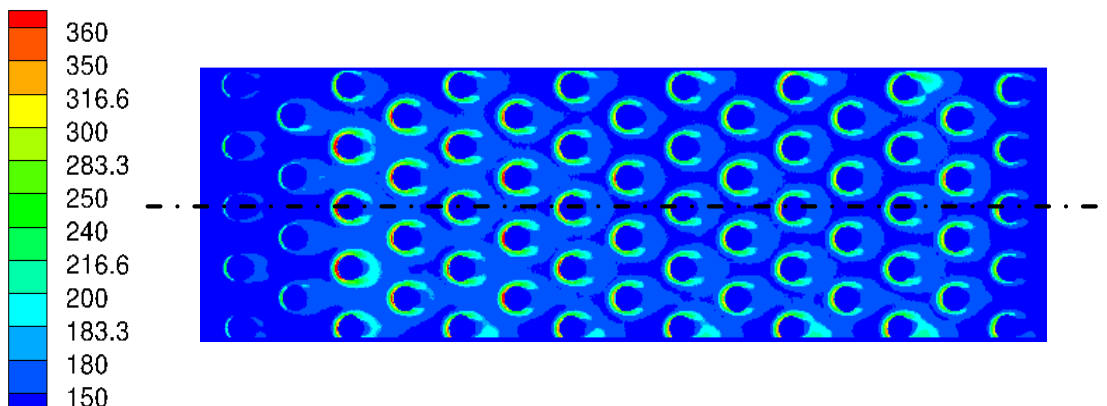Further, the lumped heat capacitance method is applied to determine the heat transfer coefficient on the pin fin for the configuration $S_x/D = S_y/D = 2.5$ and $H/D = 2$. Error! Reference source not found. shows the experimental results plotted against the literature data for one row at a Reynolds number of $Re_{D,max} \approx 10000$. Because of the stagnation point, the quadrant 1 shows always the maximum heat transfer. The experimental data is in good agreement with the experiments of Metzger & Haley and also Ames et al. The symmetry condition between quadrant 2 and 4 is satisfied. However quadrant 3 has significantly higher Nusselt number than in quadrants 2 and 4.

Metzger and Haley observed this behaviour for the first row at $Re_{D,max} = 25000$. The slight heat transfer increase in quadrant 3 can be explained by the turbulence in the wake of the pin fins.
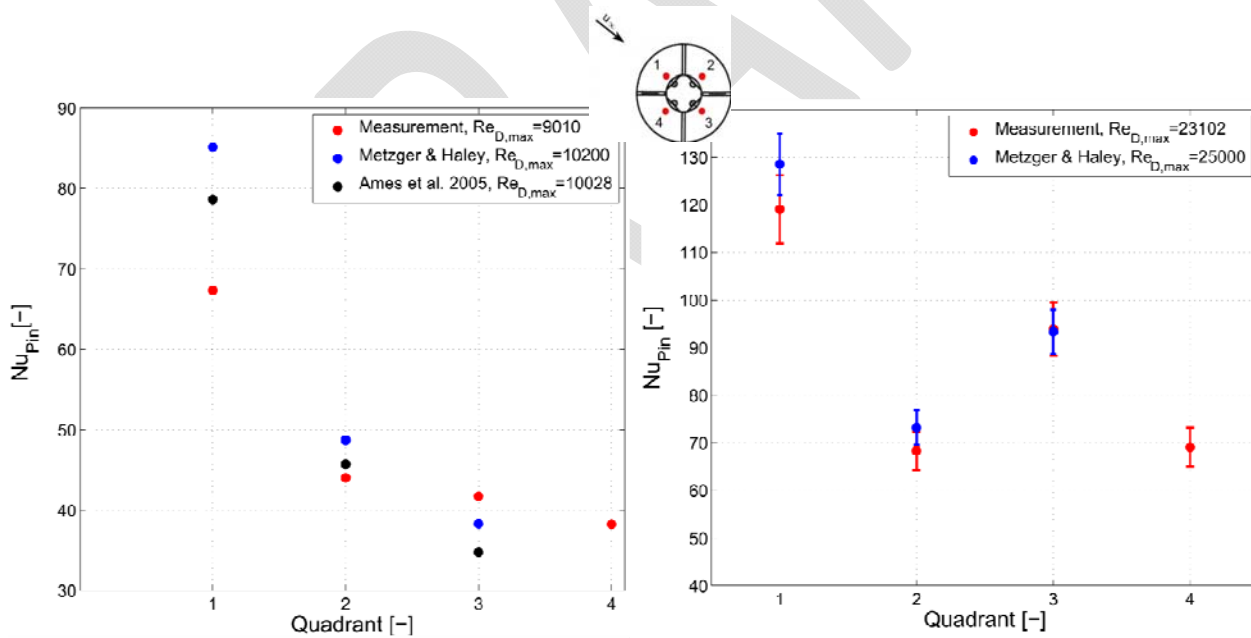
Figure 9 : Comparison of experimental local data in row 1 with data of Metzger&Haley and Ames et al.

An array averaged pin fin Nusselt number is determined for each Reynolds number for all rows. The experimental data is compared with correlations from the literature as shown in Error! Reference source not found.. The experiments agree very well with the correlations of the literature for low Reynolds numbers as well as for higher one. The overall deviation of the Nusselt number experimental data from the correlations is due to the different considered array configurations.
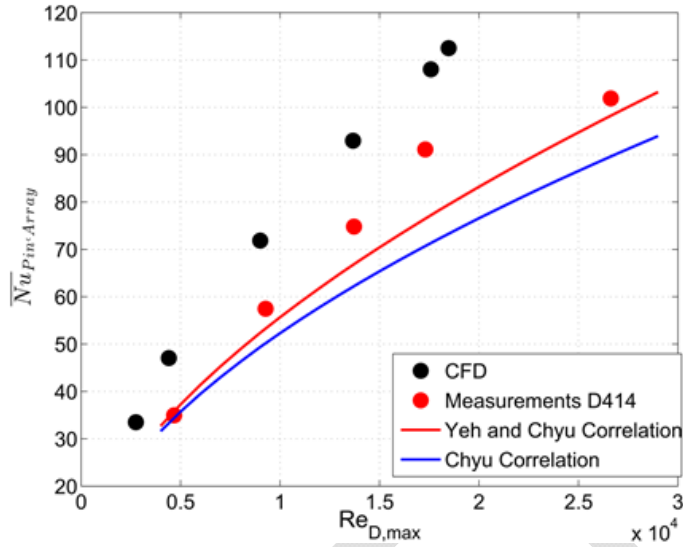
Figure 10 : Array averaged pin fin Nusselt number compared with correlations and CFD from WP5.2

With the same logic as in ATLLAS-I, some round PTAH-SOCAR monobloc cooled pin fin structures were manufactured and tested in ATLLAS2. The conical PSH samples were tested during several hours, while in ATLLAS-I the cylindrical PSR similar ducts were tested during several minutes.
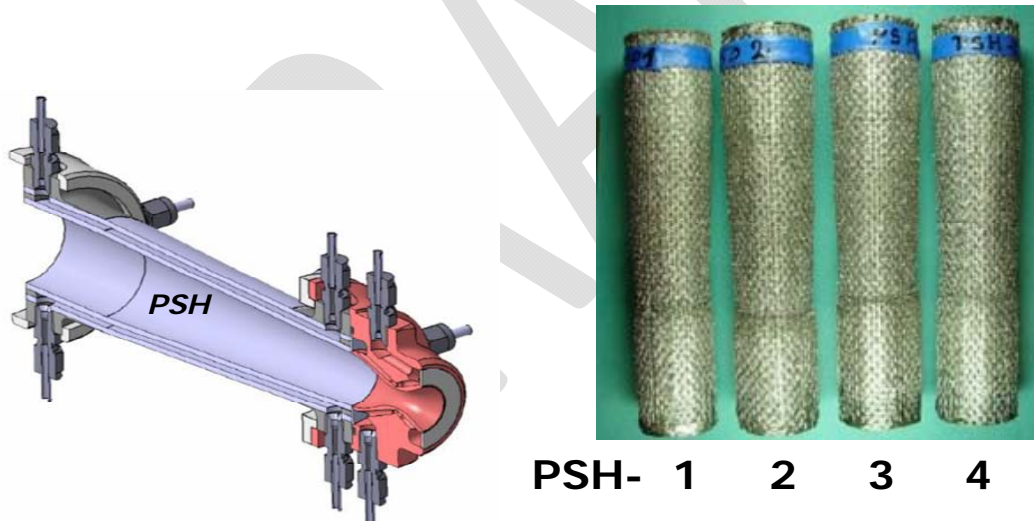
Figure 11 : pin fin cooled CMC testing in ERBURIG-K

The existing and previously checked modeling (MBDA NANCY empirical code) of such PTAH-SOCAR structures was used to compute the hot wall temperature, about 1800K, as only the coolant temperature can be measured in such experiments.

Figure 12 : modeling of PSH pin fin cooling hot experiment

In this chart, the coolant temperature is Tfluide (green curve) and the associated hot wall temperature is Tpint (blue curve), in Kelvin. The red dash curve (hgazbrules) illustrates the 2500 K hot gas heat transfer coefficient contour in the PSH conical duct, upstream from the sonic throat of the water-cooled nozzle and downstream the ERBURIG injection head.
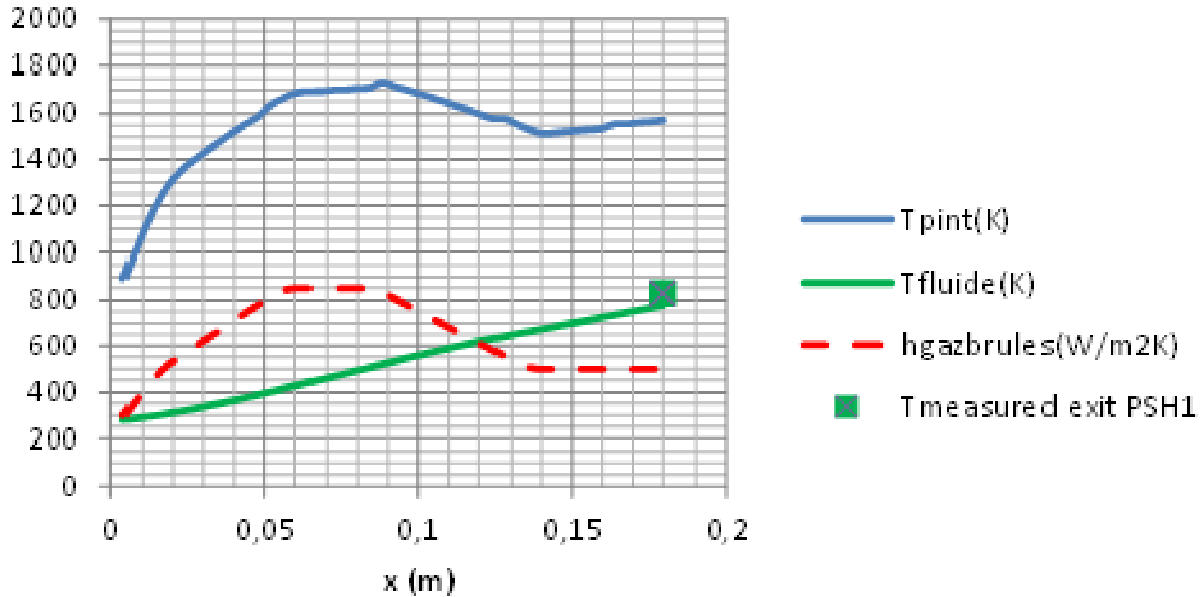
Post-test analysis was made on the tested components, for instance the SiO2 layer created by oxidation on the inner hot wall was measured.

These results will be useful to define in possible future R&T programs solutions (refined coating, for instance) to ensure thousands of hours operating with combustion of such cooled CMC structures (from ATLLAS-I to ATLLAS-II we already demonstrated minutes to hours life duration in strong oxidative environment, but this has to be continued for application on future high speed airliners).

Besides the possible applications summarized on the Figure 4, the pin fin results of ATLLAS2 can benefit to:

- Knowledge on pin fin heat exchangers (metallic ones, PTAH-SOCAR ones…)
- Passenger area cooling
- Equipment's cooling
- CFD and coupled simulations enhancement / verification (difficult test case family for local heat transfer computation).

These new results may be used on different applications in aeronautics as well as electronics, as summarized in the examples below:
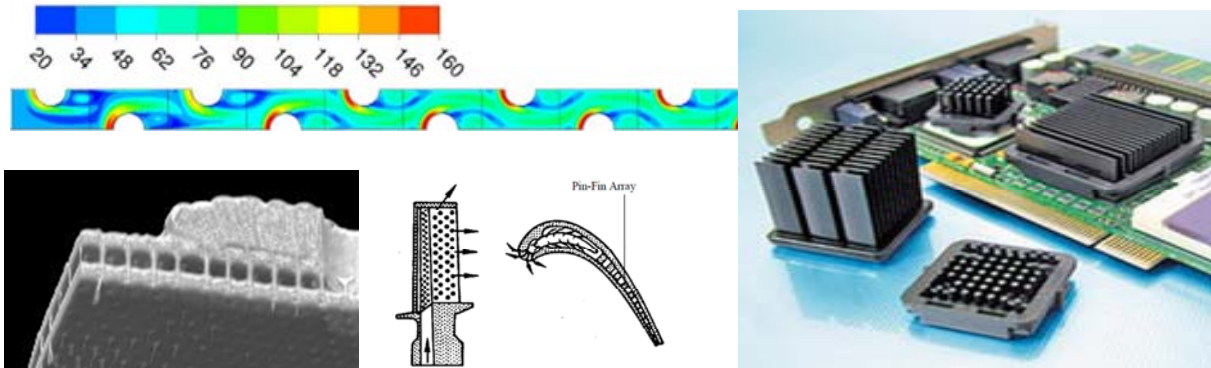
Figure 13 : examples of pin fin cooling systems

5.4   Multifunctional porous wall

A HSS panel was designed, tested in hot conditions in METHYLE under Mach 6 flight conditions with combustion. Associated computations were performed, and the design capability is claimed to be sufficient to design any multifunctional metallic hollow sphere sandwich on various applications. One again, this multifunctional design capability was realized through work in different subtasks, as summarized in the figure below: the upper part illustrates the testing devoted to hot permeability understanding while the medium part illustrates the different works performed on defining and testing a multifunctional sandwich which was computed as illustrated on the bottom part of the same figure.

● **Porous materials and multifonctionnal HSS**
  – Caracterization of porous material with GN2, GH2, temperature, stress (DLR)

  – **Multifunctional hollow sphere materials** (ONERA, MBDA)
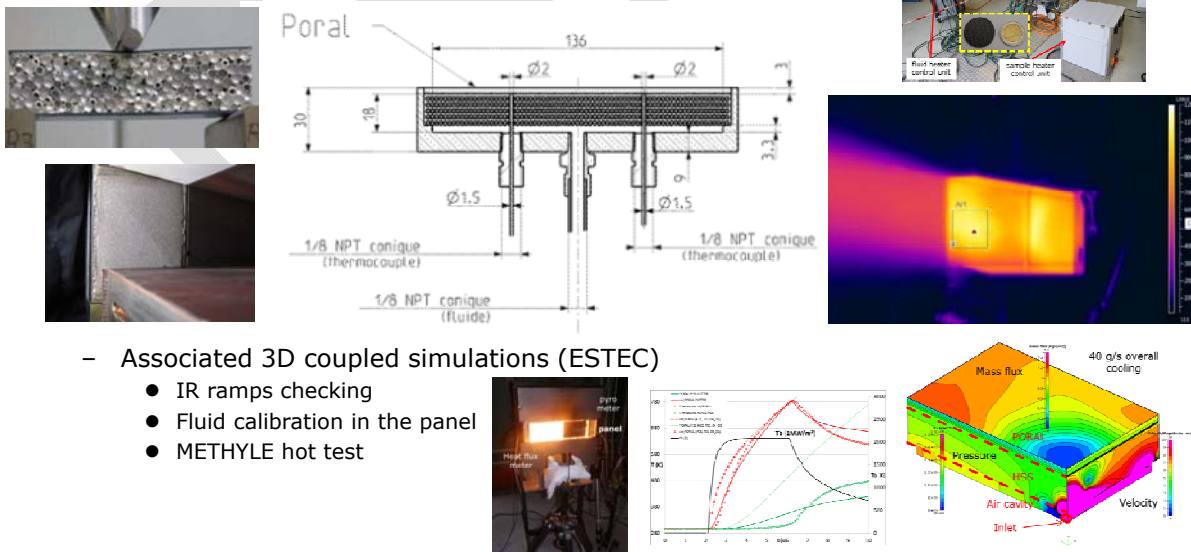
  – Associated 3D coupled simulations (ESTEC)
    ● IR ramps checking
    ● Fluid calibration in the panel
    ● METHYLE hot test

Figure 14 : permeable materials for advanced multifunctional structures in WP4
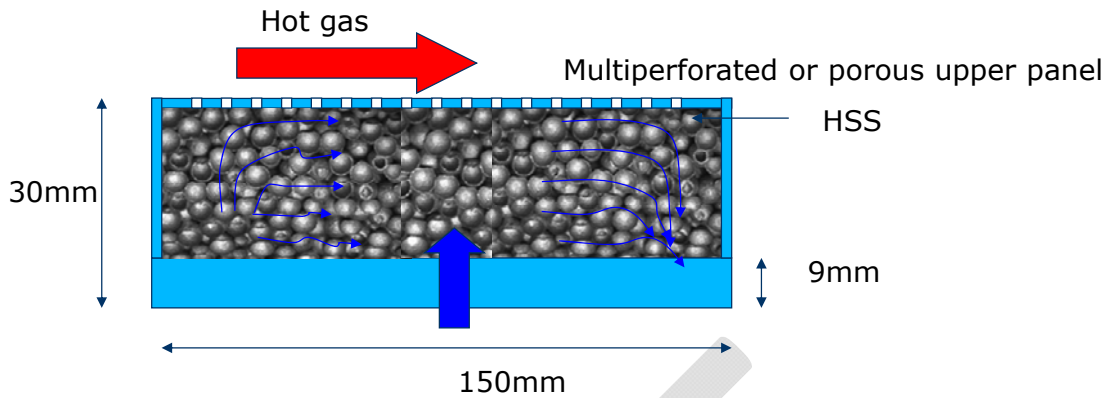
Figure 15 : principle of HSS multifonctional panel designed and tested in ATLLAS2

A generic HSS panel was designed and manufactured for cold and hot characterization. Some details are given below, for the test preparation as well as the material point of view.
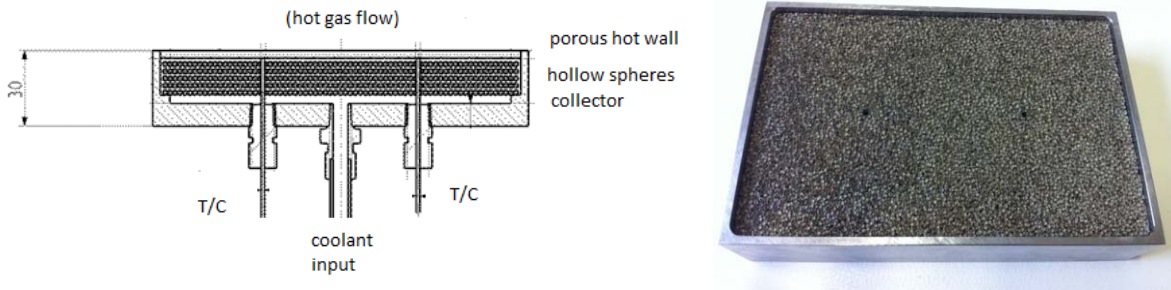
Figure 16 : HSS panel to be tested in METHYLE

The HSS panel is composed with a box with thermocouples (T/C) and coolant input and collector at the bottom part. The porous hot wall is in contact with the hot gases, with a low permeability. The hollow sphere core is welded to it and has a higher thickness and a higher permeability. The shell thickness of the hollow spheres (diameter = 2 mm) is around 50μm, and the resulting apparent density is 0,6 g/cm³.

This multifunctional sandwich is then composed of two layers of different porous material. The permeabilities of the two porous materials are very dissimilar: around 5.10^{-11} m2 for the thin porous layer in contact with hot gases, and around 100 times greater for the hollow spheres material, core of the sandwich material.

During period II, the HSS panel was designed and manufactured, then tested under IR lamps and its integrating to METHYLE test facility was checked
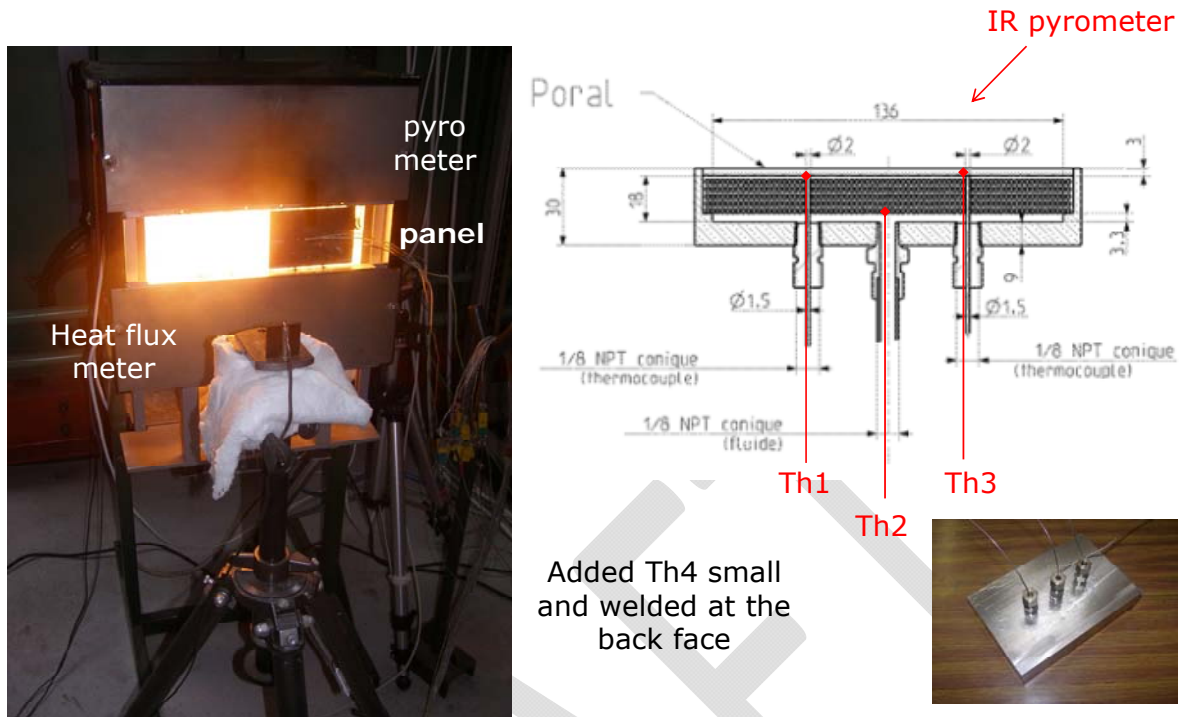
Figure 17 : uncooled thermal testing of HSS panel

The methods of computing the complex structure of double layer HSS panel from the thermal point of view were checked on these experimental results. From geometric pattern and row material characteristics (here stainless steel or alloy) it was possible to derive the density, but also the specific heat capacity, the effective conductivity of each porous layer. Afterwards, in 1D (cutter code from MBDA) and in 2D or 3D (CFD ACE code by ESTEC), the thermal modeling was also checked, based on these effective properties.
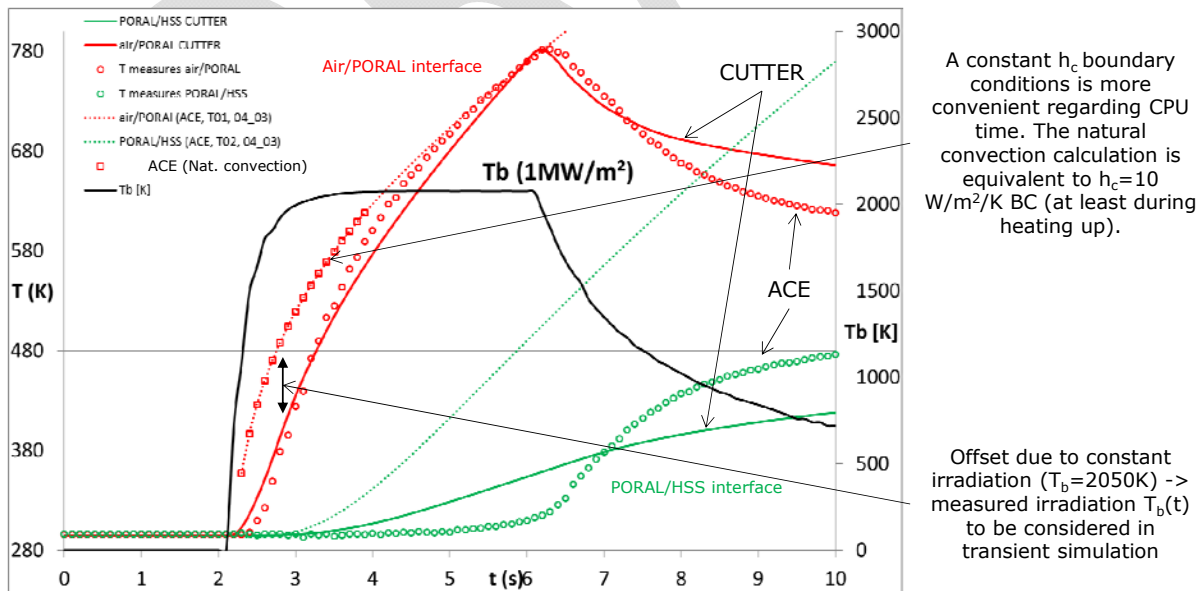
Figure 18 : temperatures computed and measured during IR lamp test of HSS panel

ESTEC did the same kind of computations with coolant flow in the HSS panel to simulate the METHYLE test (here computational domain is one quarter of the panel).
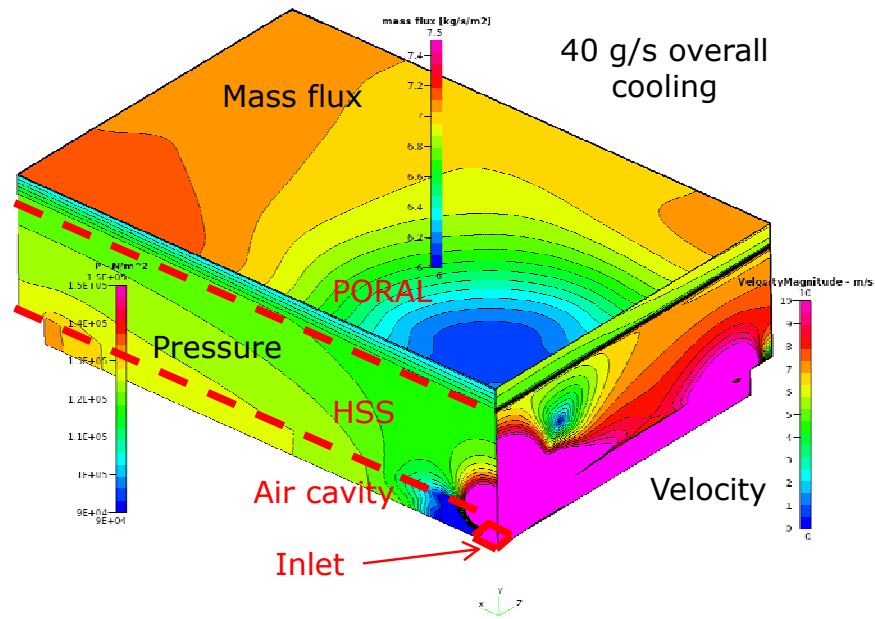
Figure 19 : example of 3D transpiration cooling computation of HSS panel

The panel was successfully tested during period III in METHYLE with two different mass flow, at the exit of the MBDA dual-mode ramjet, with stoichiometric combustion with flight conditions of Mach 6.
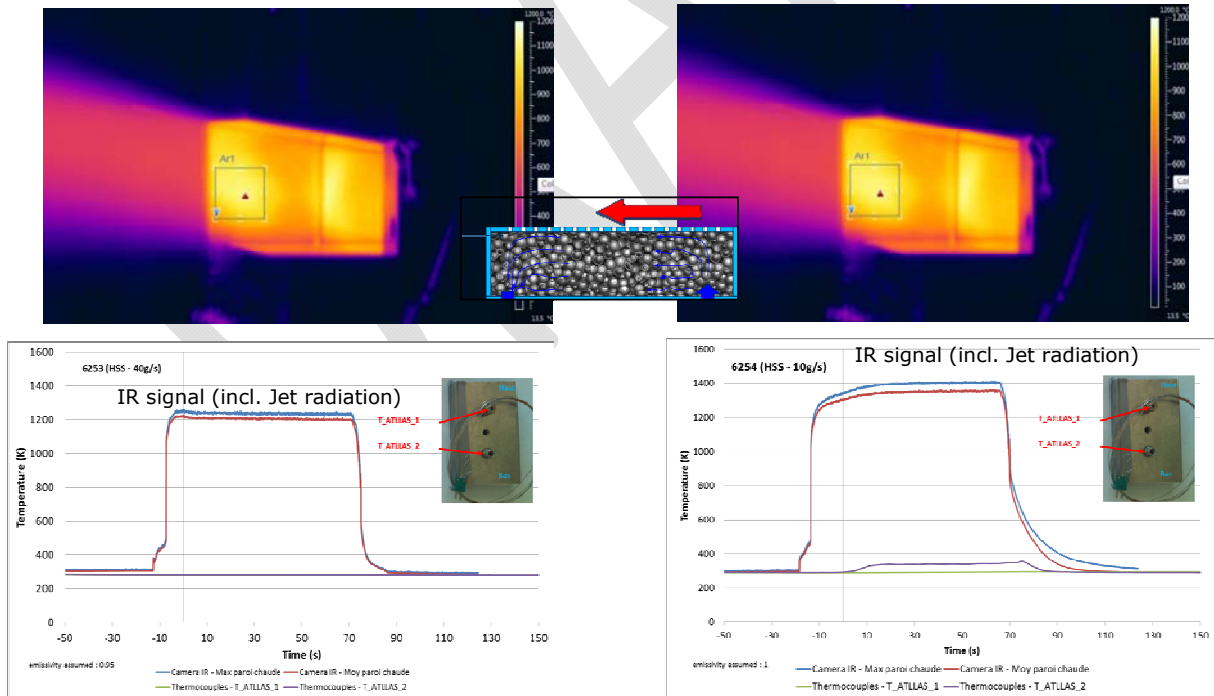
Figure 20 : hot testing of multifunctional generic HSS panel at Mach 6 with combustion

Post-test analysis of the apparently not damaged panel allows to check any possible oxidation of the upper layer as well as minor change of permeability.

Panel positioning in the duct of SMR test

Top of the panel Back side

	Density (g/cm³) before the test	Density (g/cm³) after the test
HSS	0,55	0,59
Poral	4,24	4,37

=> Small oxidation of the materials

Poral layer before test Poral layer after test (zone 4)
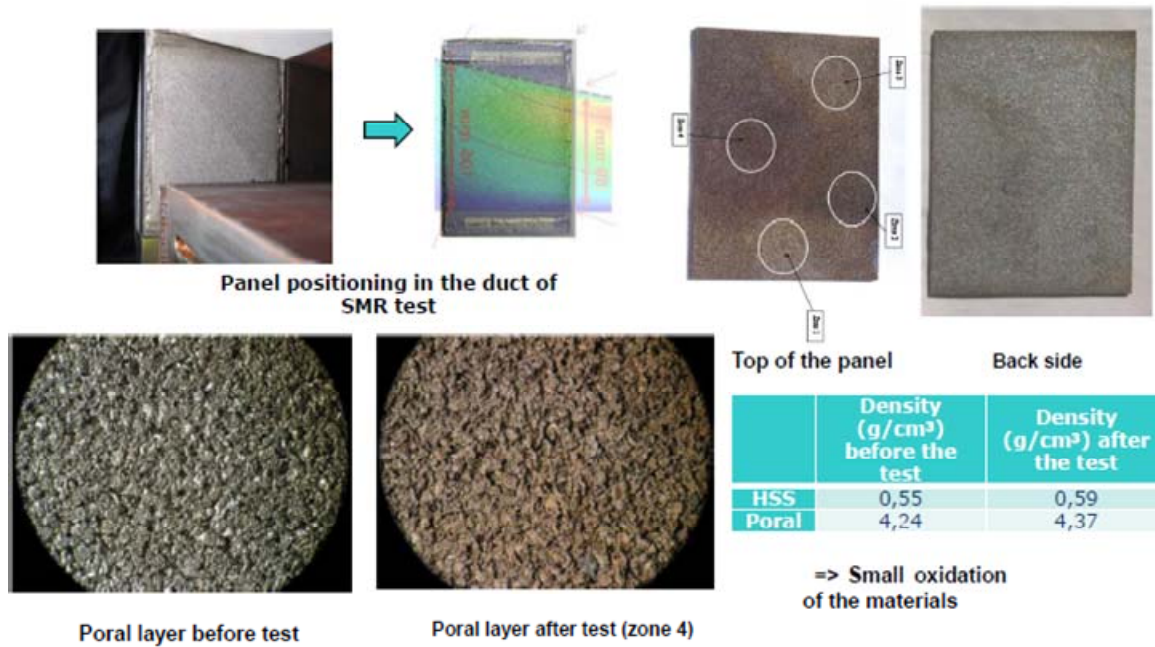
Figure 21 : post-test analysis of HSS panel

A small decrease of permeability was registered after the test, probably due to dust deposit in the inner wall through incoming GN2 coolant and to soot deposit on the hot porous layer.
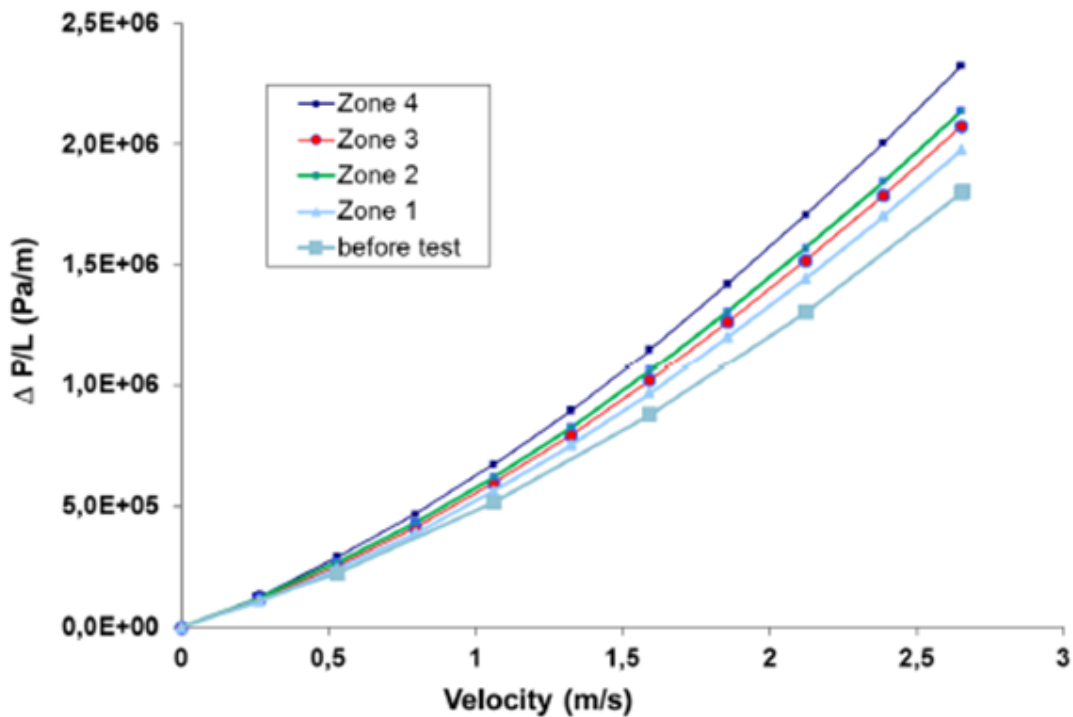
Figure 22 : effect of hot testing on ambient permeation of HSS panel

The methods to predict the mechanical, fluidic, thermal characteristics of different multifunctional HSS structures with different materials were checked during ATLLAS1 and ATLLAS2. Acoustic behaviour of HSS was investigated and proven but the associated design methods are still to be developed for such industrial design. These methods can be used to prepare suitable customized

multifunctional structures, for instance in our future airliner: after- body, wing skin, boundary layer bleed:
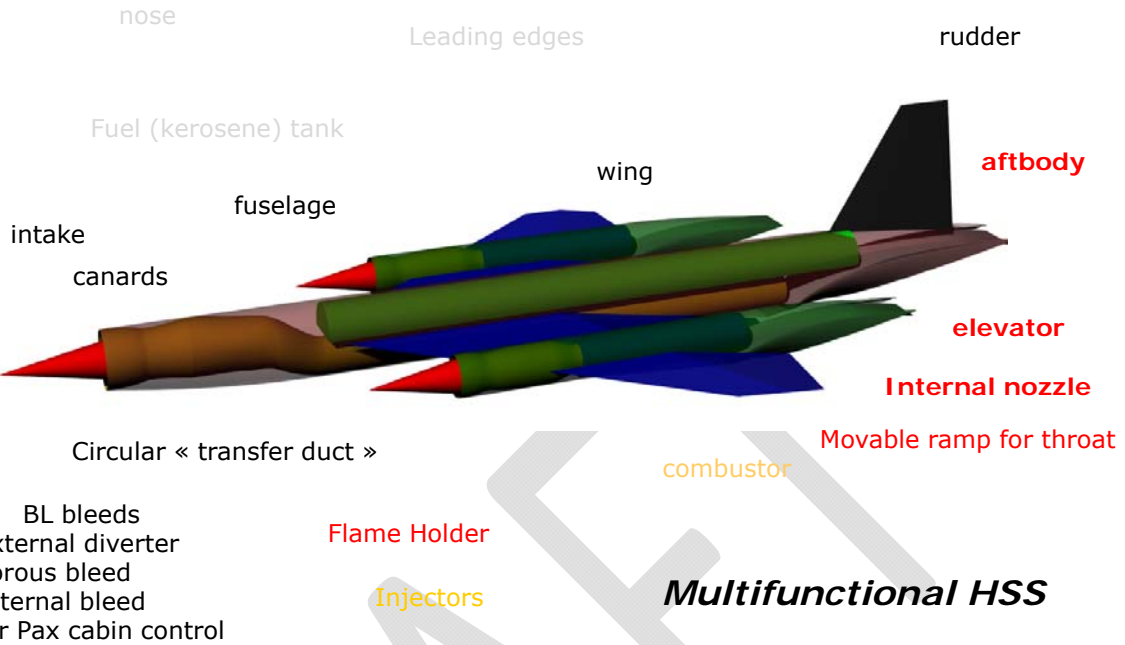
Figure 23 : synthesis view of HSS possible use of high speed airliner

In future studies, additive manufacturing may also participate to extend the usability of such multifunctional structures.

The present HSS technology, investigated in ATLLAS, is one of the possible solutions to organize cores of advanced structures, as it can be drawn on the following figures extracted from the Ashby metal foam "bible".
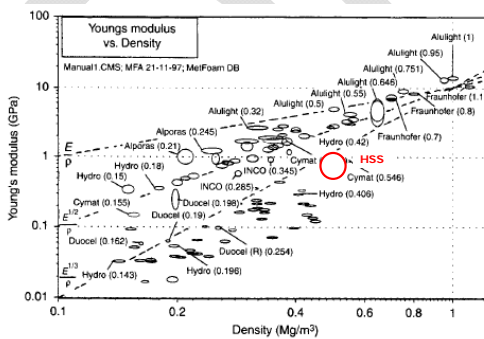
Figure 4.6 *Young's modulus plotted against density for currently available metal foams. Output from CES3.1 with the MetFoam '97 database*
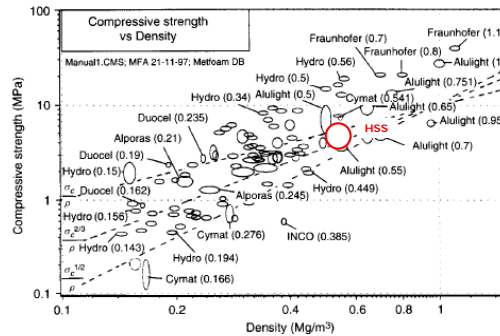
Figure 4.7 *The compressive strength plotted against density for currently available metal foams. Output from CES3.1 with the MetFoam '97 database*

Figure 24 : HSS possible use for metal foam sandwiches

5.5   Injection struts technology

Based on different projects and published results, and on the test facilities capacities, a generic diamond shape injection strut was defined. Different technologies of cooling (convective, transpiration) and different materials (UHTC and CMC) were applied to manufacture these samples.
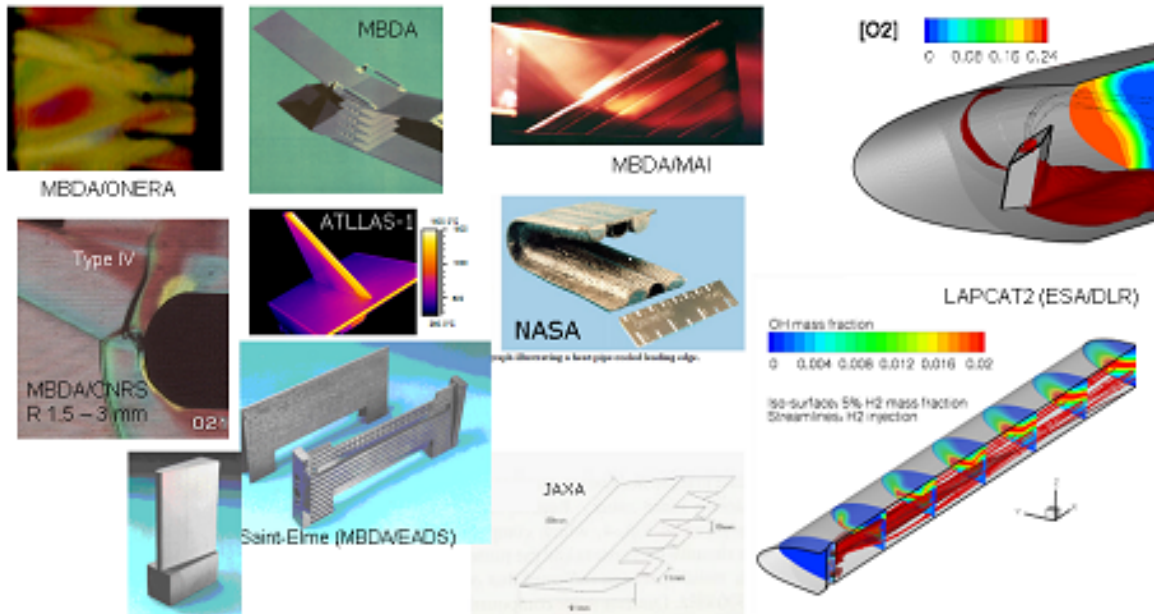
Figure 25 : examples of injection struts taken into account to define the ATLLAS2 generic fin injector

This generic injector was defined to address the technology challenges on possible actual systems, without any combustion or injection optimization which was out of the scope of ATLLAS-II and would depend on each propulsion system. Based on this generic design, different technologies were considered which led to a modified injector shape in order to cope with actual possibilities. Especially the swept back part was progressively moved to an unswept one for CMC manufacturing limits with the techniques used in ATLLAS II.
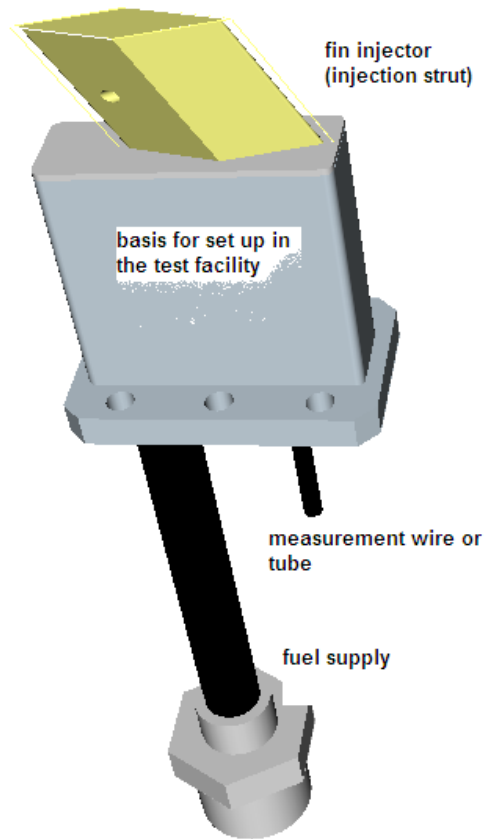
Figure 26 : CAD view of ATLLAS2 generic injector on its test facility basis

Two ways were to be investigated in ATLLAS-II for such injectors : CMC (convective or transpiration cooled) and massive UHTC.
An important work has been carried out on the manufacturing of the injector with UHTC. At the end, all the attempts to manufacture such a complete injector in massive UHTC failed.
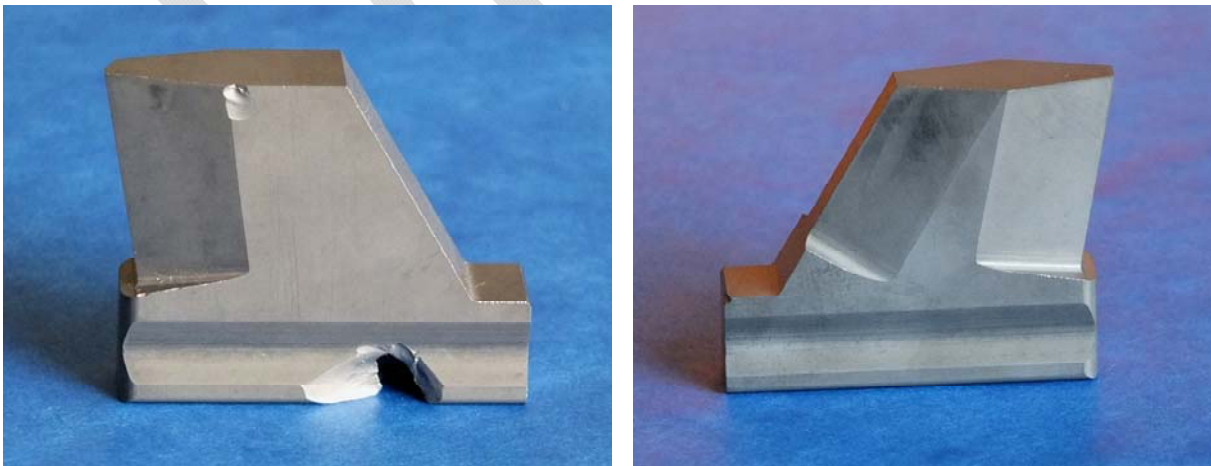
Figure 27 : examples of complete UHTC struts (at left, HfB2/SiC/Y2O3 prototype broken during fuel tube drilling and at right HfB2/SiC sample stopped before the machining finalization)

ONERA and DLR redesigned a CMC-based injector with a blunt (R1) UHTC leading edge. 4 leading edges with two different UHTC compositions were successfully manufactured and adapted to the on CMC injector base parts.
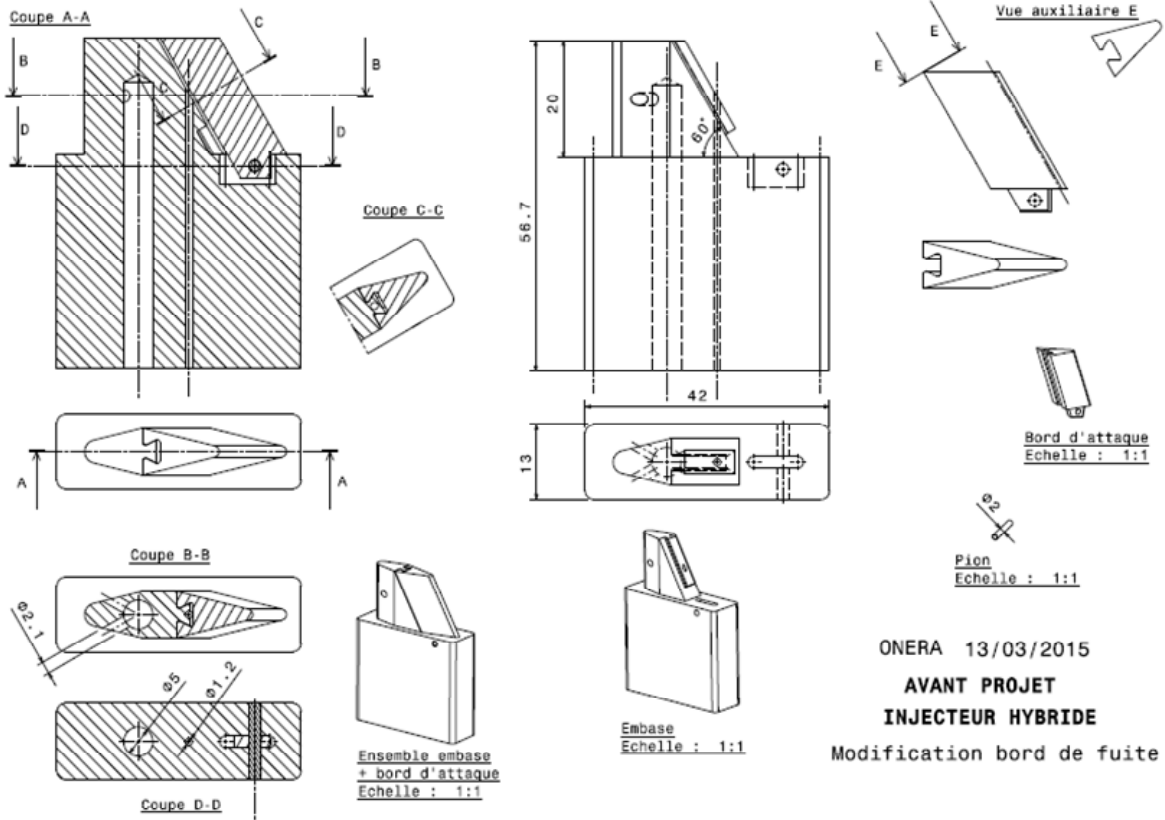
Figure 28 : final design of UHTC technology injectors

Figure 29 : UHTC/CMC injectors before hot test

Subsequently, the hybrid UHTC-CMC design was adapted to pure CMC-based designs. Different injectors were manufactured by DLR, with convective (passive but internal cooling by fuel) and transpiration (embedded porous wall at the leading edge) cooling, with and without coating and with sharp or blunt (R1) leading edges.
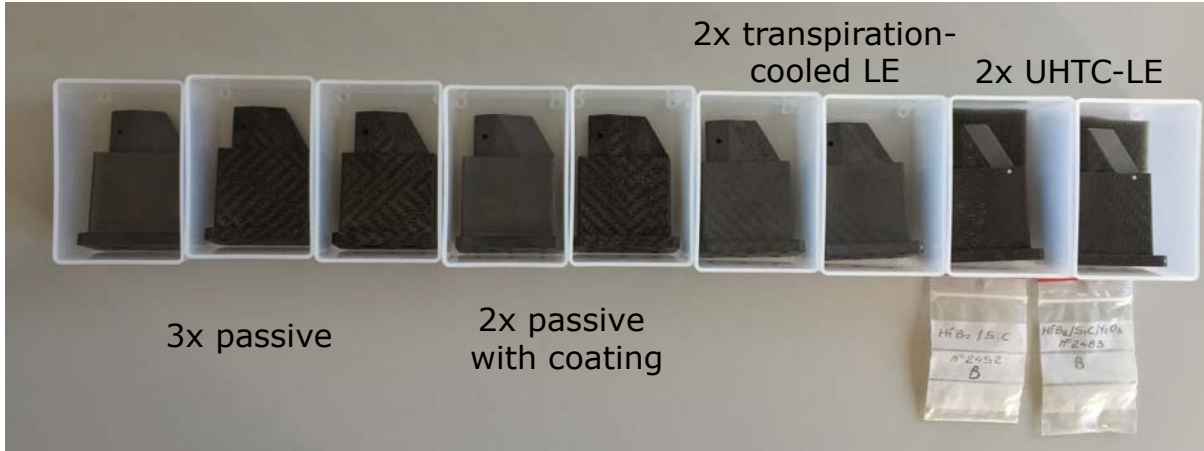
Figure 30 : generic injectors manufactured in WP4

Preparation of the USTUTT and METHYLE testing of the injectors was performed during period II. Due to later than expected injectors availability date, test can only occur in period III, in METHYLE. UHTC injectors cannot be fully realized and then the preparatory "one UHTC strut" test was not performed at USTUTT. Detailed CFD analysis was nevertheless performed by USTUTT with the generic ATLLAS-II injectors.
All different technologies of ATLLAS2 injectors were tested under METHYLE Mach 6 combustion.

The 7 following injectors were tested:

- DLR_6) LE_3_01_A : C/C-SiC injector with transpiration cooled leading edge, R1 – T_ATLLAS_1 (not available)

- DLR_8) LE_4_01_UHTC : C/C-SiC injector with UHTC leading edge and MACOR locking pin, adapted for UHTC material HfB2/SiC (0NERA N° 2492 A) – T_ATLLAS_2

- DLR_9) LE_4_01_UHTC_Y2O3 : C/C-SiC injector with UHTC leading edge and MACOR locking pin, adapted for UHTC material HfB2/SiC/Y2O3 (0NERA N° 2483 A) – T_ATLLAS_3

- DLR_2) LE_1_01 : C/C-SiC injector,R1 – T_ATLLAS_6

- DLR_3) LE_1_02_gew : C/C-SiC, Thread, R1 – T_ATLLAS_5

- DLR_5) LE_2_01 : C/C-SiC injector, R0 – T_ATLLAS_7

- DLR_7) LE_3_01_B : C/C-SiC injector with transpiration cooled leading edge, R1 – T_ATLLAS_4.

They correspond to Mach 6 flight conditions, with a stoichiometric fuel injection in the SMR dual-mode ramjet chamber, with a H2/CH4 gaseous fuel (20% in weight of H2).

Some views from the hot test are given below:
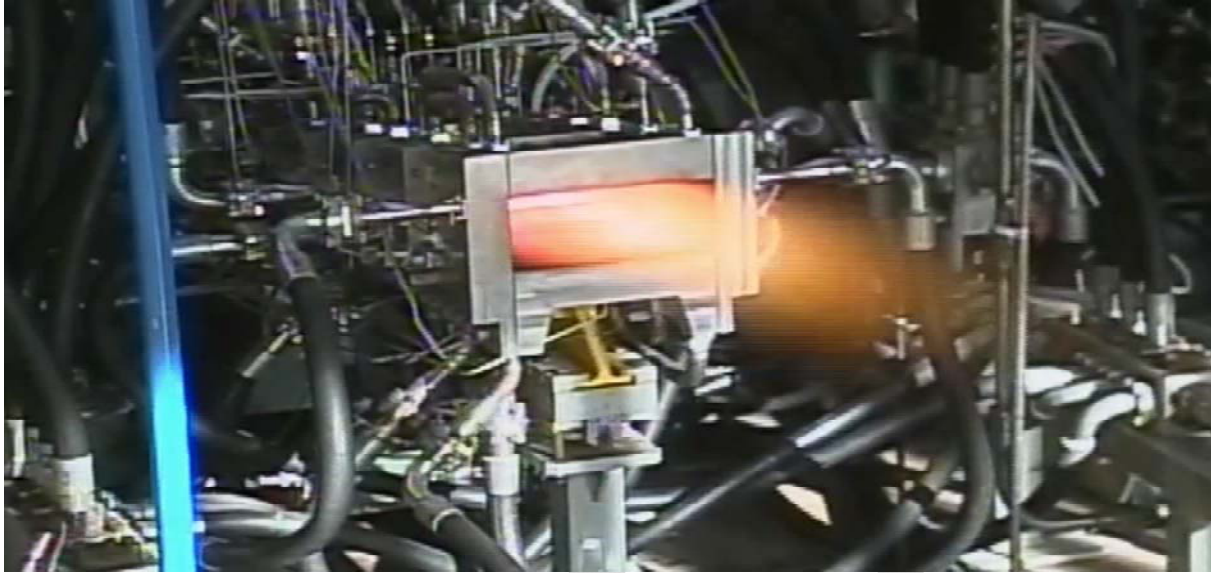
Figure 31 : view of METHYLE test with some ATLLAS2 generic injectors

Figure 32 : another view of METHYLE test with some ATLLAS2 generic injectors

Each injection strut was fed during the METHYLE test series by a 20%H2 80% CH4 gaseous mixture. The mass flow per ATLLAS2 strut is about 12 g/s.

The thermocouples implemented in the leading edge give the expected qualitative values:
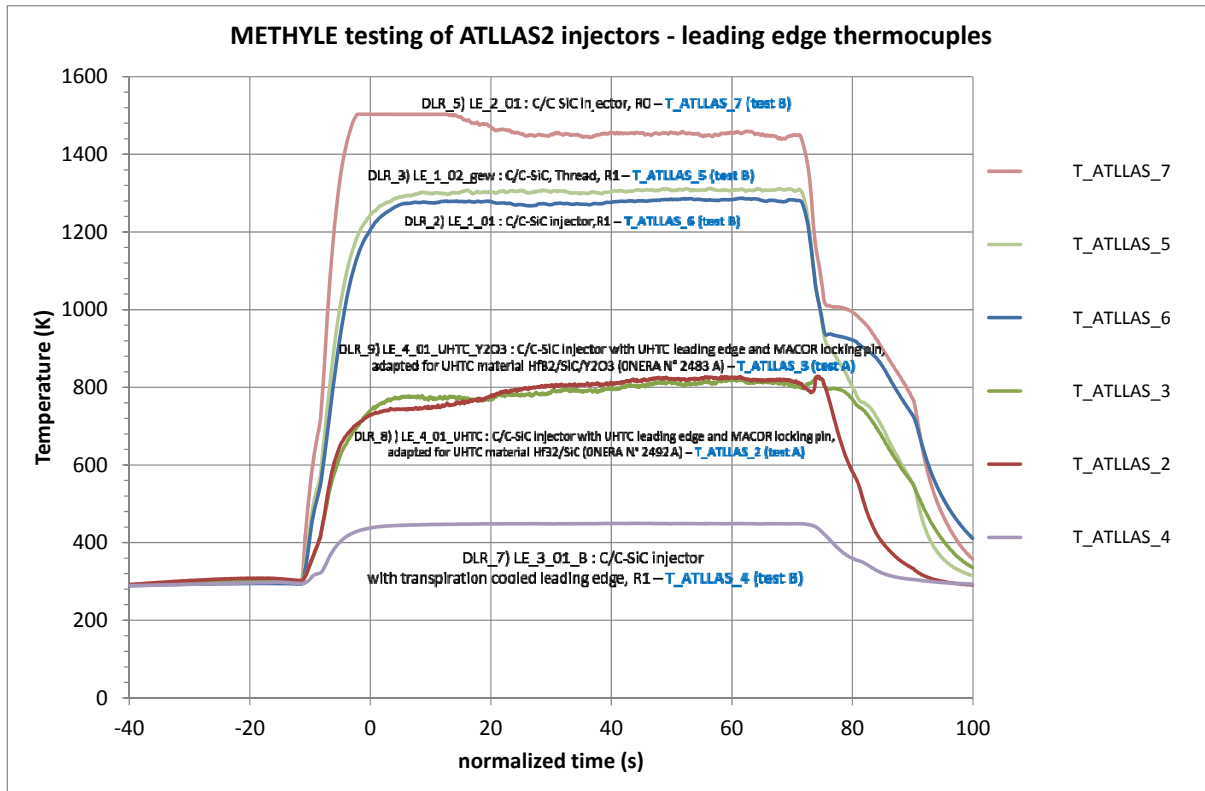
Figure 33 : injector leading edge inside temperature leading edge during METHYLE testing

The similar technologies lead to similar temperatures:

- DLR_2 and DLR_3: C/C-SiC injectors with radius 1 mm
- DLR_8 and DLR_9: UHTC injectors

The differences in technology lead to quite different temperatures :

- DLR_5 with radius R0 gives higher temperature than the DLR_2 and DLR_3 with R1
- DLR_7 with transpiration cooling gives very low temperature.

It shall be noticed than the incoming air has a recovery temperature of about 1600 K, and that no cooling by radiation is possible: the SMR wall are water-cooled but covered with a thick thermal barrier coating, leading to nearly adiabatic wall temperatures.

After the test series, the injectors were dismounted and given back to DLR for post-test analysis. No one was noticeably damaged, which is an important result (and yet it was really challenging especially for monolithic UHTC components).

Two examples of post-test photos of struts are given below.

Figure 34 : post-test view of transpiration-cooled CMC generic strut
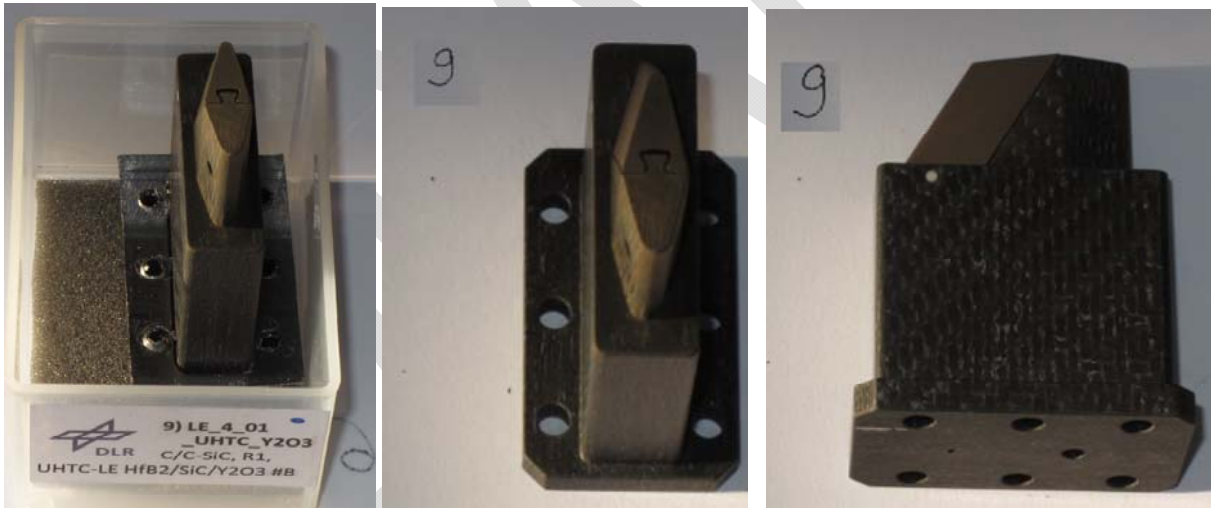
Figure 35 : post-test view of UHTC/CMC generic strut

This technological effort may be used for different applications, not only injection struts, in a future high speed airliner:

nose   Leading edges   rudder

Fuel (kerosene) tank   aftbody

                                    wing

                            fuselage

intake

canards

                                                        elevator

                                                        Internal nozzle

Circular « transfer duct »   Movable ramp for throat

                                            combustor

BL bleeds
- External diverter   **Flame Holder**
- Porous bleed
- Internal bleed   **Injectors**   *Injection struts*
- Air Pax cabin control   *technology*
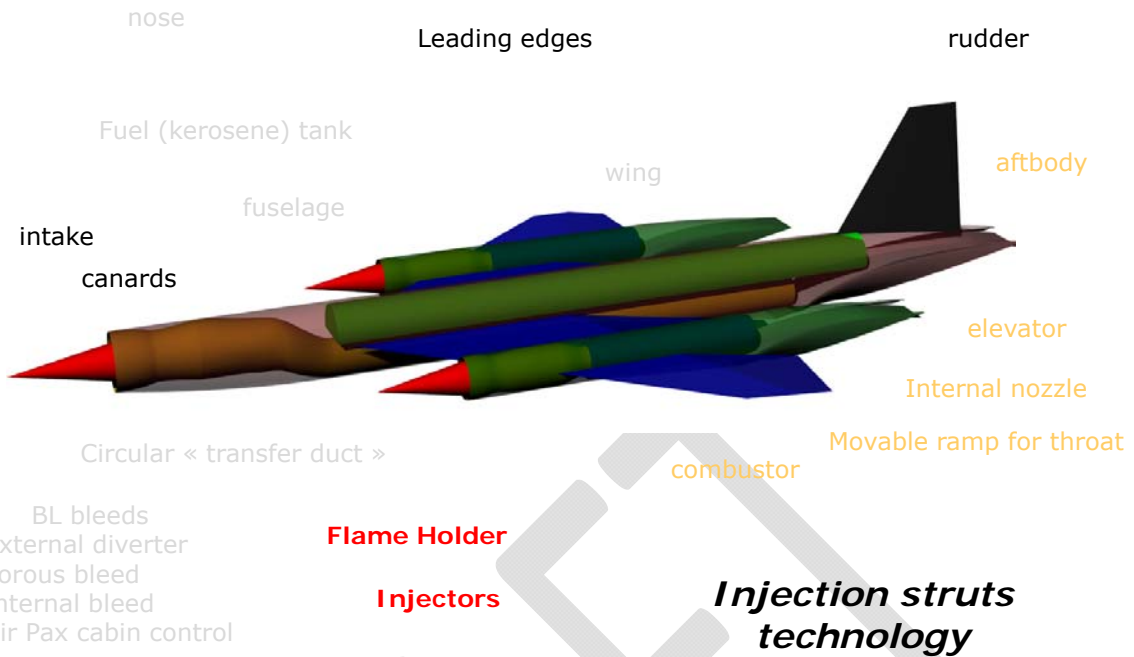
Figure 36 : synthesis view of CMC/UHTC fin technologies possible use of high speed airliner

5.6   CMC characterization

More generally, CMC materials are possibly and sometimes mandatory used on future high speed airliner:

nose   **Leading edges**   **rudder**

Fuel (kerosene) tank

                                    wing   **aftbody**

                        fuselage

intake

canards

                                                        elevator

                                                        Internal nozzle

Circular « transfer duct »   Movable ramp for throat

                                            combustor

BL bleeds
- **External diverter**   **Flame Holder**
- **Porous bleed**
- **Internal bleed**   **Injectors**   *CMC characterization*
- **Air Pax cabin control**
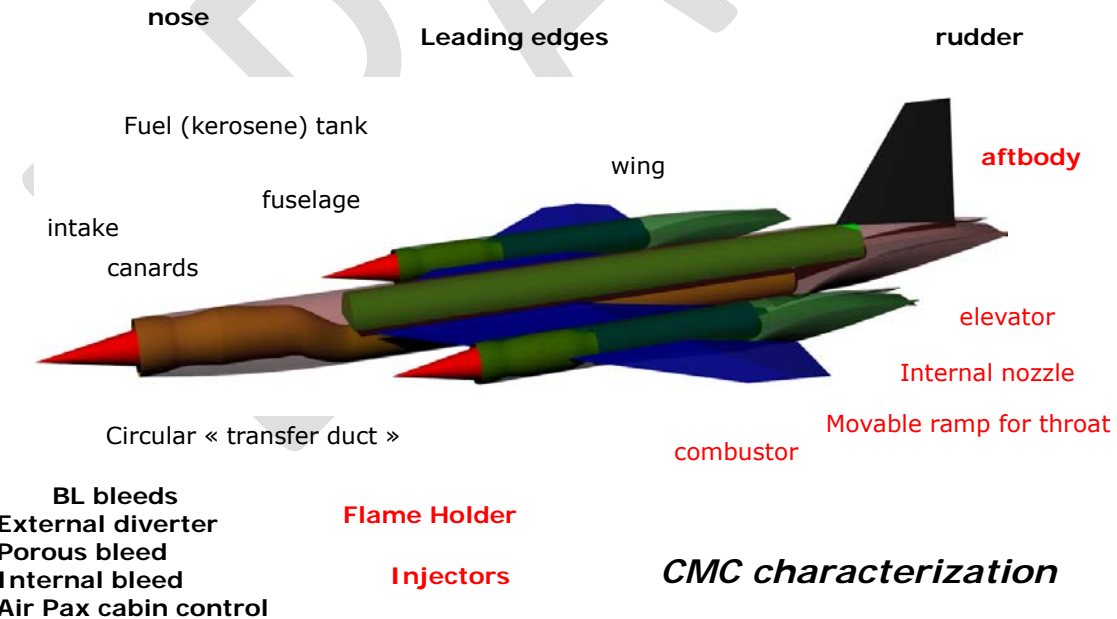
Figure 37 : synthesis view of CMC possible use of high speed airliner

Different activities were performed, leading to better understand CMC behaviour for high speed oxidative environment (Figure 38) :
- Erburig flat plates (AGI, DLR)
- Permeability in hot conditions (DLR)

- CMC uncooled panel in scramjet nozzle environment (DLR, MBDA)
- Injectors manufacturing (DLR).

Some of them were already described above in the present report, some others are presented in the present chapter.
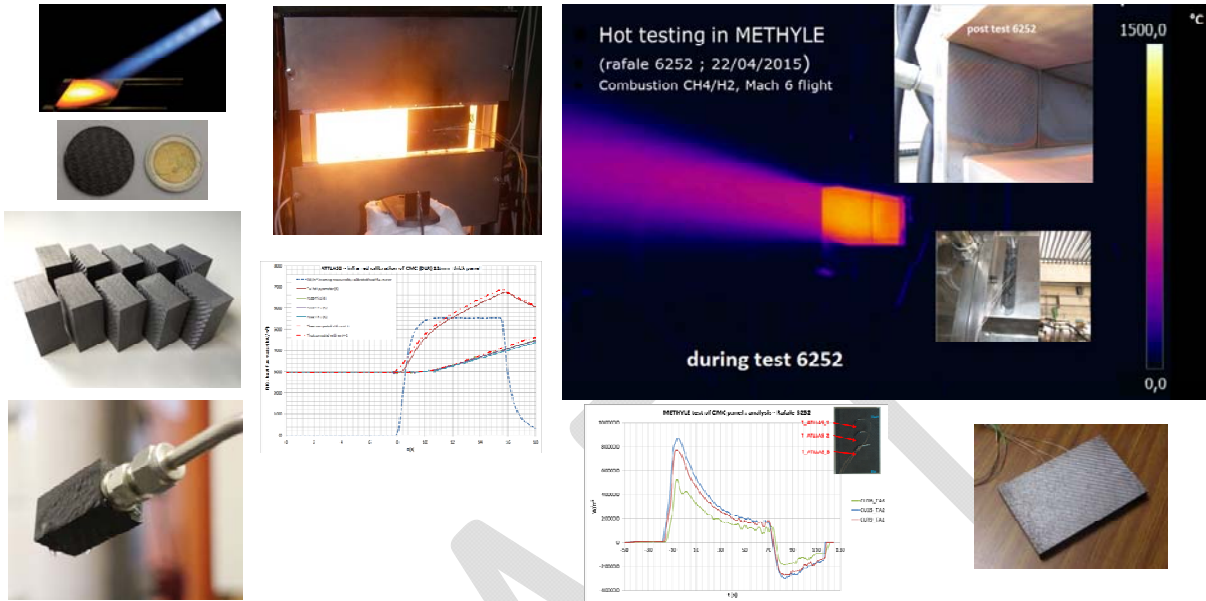
Figure 38 : overview of CMC activities in WP4 of ATLLAS2

In WP4.1.1, after developing the test plans and overall design of the CMC material samples in period I, different CMC material samples were manufactured by DLR and Airbus and tested in ERBURIG-K.

Figure 39 : flat sample testing at the ERBURIG^K test facility

During period II, the flat CMC material samples provided by DLR were tested according to the test plan (Table 2). The testing was conducted in a temperature range from 1050-1700°C. Post-test analysis of the tested DLR flat CMC material samples was conducted by the manufacturer.

Table 2 ERBURIG^K test plan for flat CMC material samples of DLR.

System	Tradename	Temperature [°C] / Time [h]	Amount of Samples
C/C-SiC w/o coating	---	1500 / 1 1700 / 1	2
C/C-SiC w/ CVD-SiC	---	1500 / 4 1700 / 1	2
SiC/SiCN (LaPO4)	---	1300 / 4 1500 / 4 1700 / **1,5**	3
SiC/SiCN (pyC)	---	1300 / 4 1500 / 4 1700 / **4**	3
Ox./Ox. (RBAO-SC)	WHIPOX	**1050** / 4 1200 / **0,5**	2
Ox./Ox. (RBAO-CF)	WHIPOX	**1050** / 4 1200/ **0,5**	2
Total		**37,5 h (planned: 35h)**	14

During period III, other CMC samples, provided by Airbus GI, were tested under the same type of conditions (**Error! Reference source not found.**).

Table 3 : ERBURIG^K tested flat CMC material samples of AGI

Temperature*	No Coating (T_{ave}**)
~1500°C	04min 24s (1394°C)
~1300°C	08min 15s (1216°C)
~1100°C	15min 09s (1112°C)

before test   after test (1757°C, Coat I)
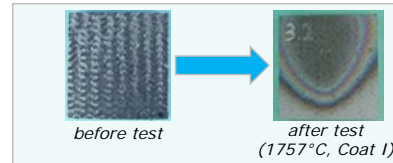
Temperature*	Coating I (T_{ave}**)	Coating II (T_{ave}**)
~1900°C	06min 20s (1757°C)	08min 21s (1740°C)
~1750°C	26min 15s (1622°C)	53min 07s (1620°C)
~1500°C	59min 01s (1502°C)	59min 58s (1484°C)
~1300°C	47min 05s (1338°C)	133min 15s (1313°C)

Benchmark: SICARBON w/ CVD-SiC

Temperature*	Time (T_{ave}*)
~1900°C	03h (1925°C)
~1750°C	13h (1787°C)

Test segment length: 0,5h
Abort criterion:
- 4h (acc. testing time)
  or
- rapid increase in sample temperature

* Temperature on SICARBON w/ CVD-SiC w/ adjusted ε

**Temperature measurement w/ ε=0,875

Nota : DLR materials results presented in Mid-Term Review and period 2 report

Computations of the ERBURIG test on a generic flat sample were achieved during period II and refined during period III. This problem was confirmed as a difficult one for CFD and coupled simulations, in 2013 some engineering students worked (with the support of a CFD senior scientist from University) on a generic case derived from the ERBURIG experiment, and they face a lot of difficulties to obtain results without physical inconsistency! The computations within ATLLAS2 eventually gave with CEDRE and with CFD-ACE relevant results, but once again after unplanned computational effort. These results are summarized below, they help to analyse the past and future ERBURIG test of CMC flat samples.

Preliminary computations were performed in 2013 under student projects with Fluent (generic case, 3 months) and it was confirmed a difficult test case for CFD (jet impingement). In WP5 "ATLLAS2 industrial tool box "work, ESTEC and MBDA professionals confirmed this difficulty, and solved it after some unexpected effort, with adequate choice of boundary conditions types at freeflow limits.
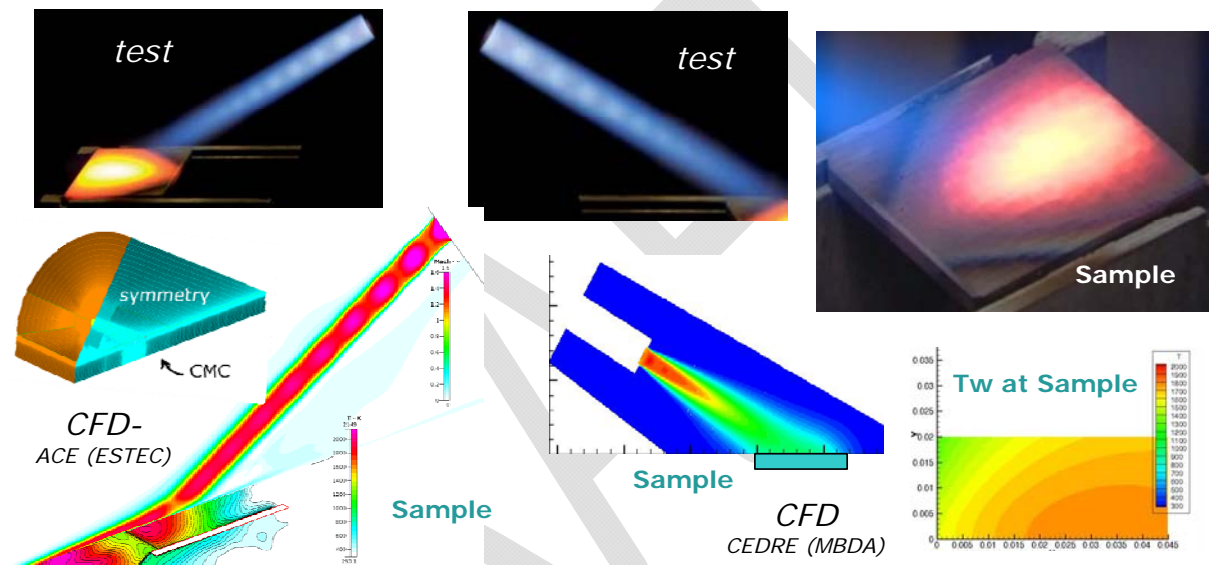
Figure 40 : Summary of 3D CFD simulations of the ERBURIG test

In WP4.1.2, investigation of Hot permeability measurements of CMC samples was held on different CMC samples (C/C and OXYPOL).

In the framework of the ATLLAS II project, DLR Lampoldshausen has investigated the dependency of the permeability of porous materials on temperature and stress by performing various permeability tests using the DLR Lampoldshausen test bench P6.1. Approximately cylindrical ATLLAS test samples made of C/C random (±15°) and OXIPOL 3x pyrolysed (0|90°) with two fibre designs (parallel and perpendicular penetration) have been used in the test campaign. Two approaches for the determination of the permeability parameters have been compared.

In comparison to the previously used ambient temperature permeability test set-up (in ATLLAS-I and in ATLLAS-II for instance), the elevated temperature permeability test set-up used here additionally contains a test fluid heating system (based on copper tubes wound around cartridge heaters as shown on the left-hand side of **Error! Reference source not found.**) as well as a flow probe heating system (based on flexible line heaters) as shown on the right-hand side of figure 8.

Cartridge heaters as used (together with copper tubes wound around them) for fluid heating:
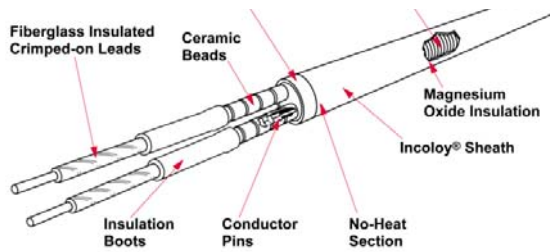
Flow probe holder (made from copper) including flexible line heaters:

channels for 3 flexible line heaters

magnified inner part of the sample holder (holds conical flow probes)
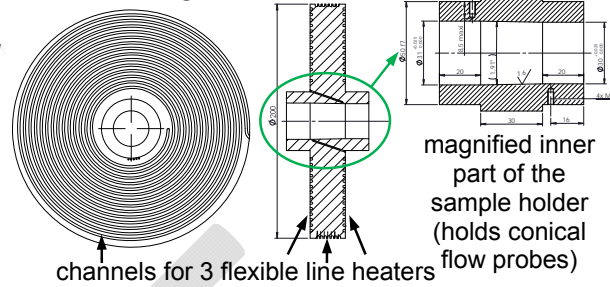
Figure 41 : Additional devices necessary for measuring the material permeability under elevated temperatures.

Before the start of each elevated temperature permeability test, the (closed loop) control units of the fluid heater and the sample heater are set to the intended temperature levels. During the test, a variation of the mass flow rate trough the flow probe and the total pressure level in the flow probe is obtained by a wide variation of the opening levels of control valves situated upstream and downstream of the flow probe as indicated on the left-hand side of **Error! Reference source not found.**. As the main test objective is to obtain a large number of stationary values for the mass flow rate, the total pressure level as well as the differential pressure between the inlet and the outlet of the flow probe, pre-defined control valve opening setting sequences are used instead of a closed loop control of the valves. A photograph of the complete test set-up is shown on the right-hand side of **Error! Reference source not found.**.
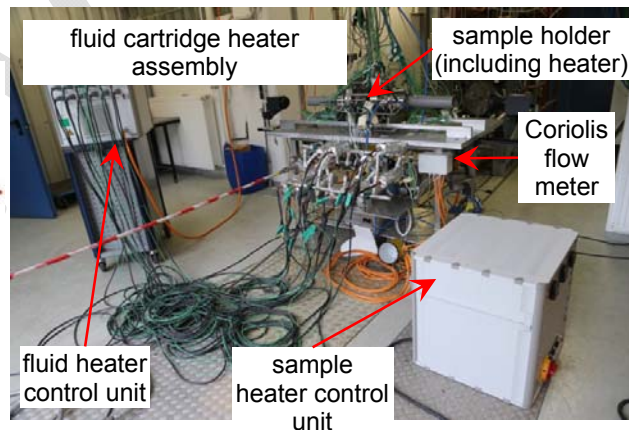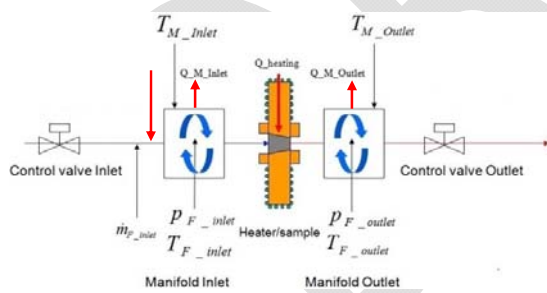
Figure 42 : Flow scheme (left) and photograph (right) of the elevated temperature permeability measurement set-up.

Darcy and Forcheimer permeabilities (Kd and Kf) of each sample are derived from the "mass flow vs pressure drop" measurements.
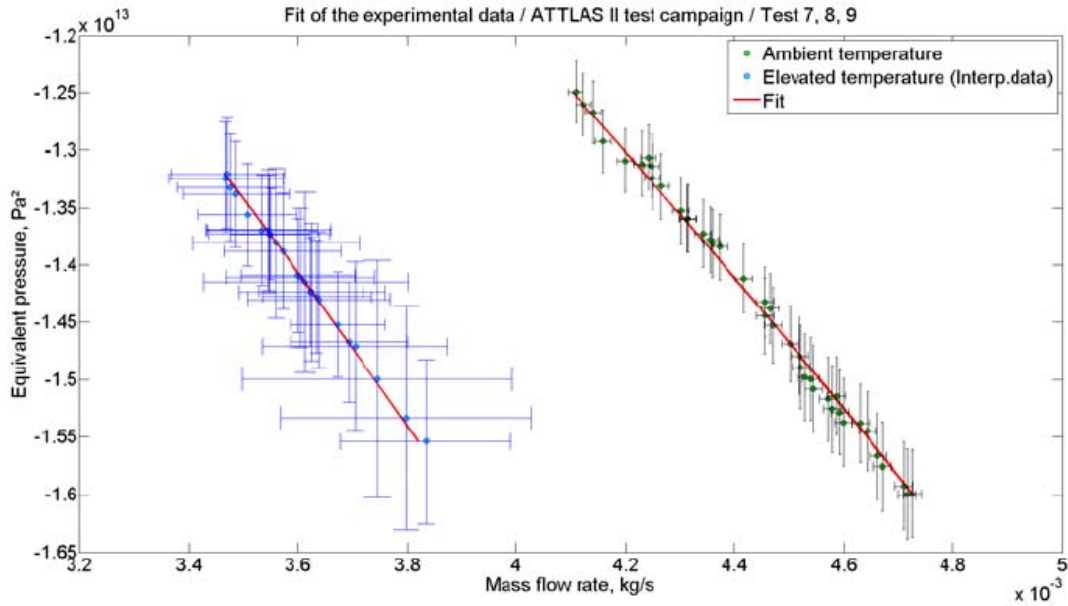
Figure 43 : Fit of the experimental data for the ATLLAS test sample C/C random perpendicular at ambient temperature (300 K) and at "isothermal elevated" temperature (360 K)
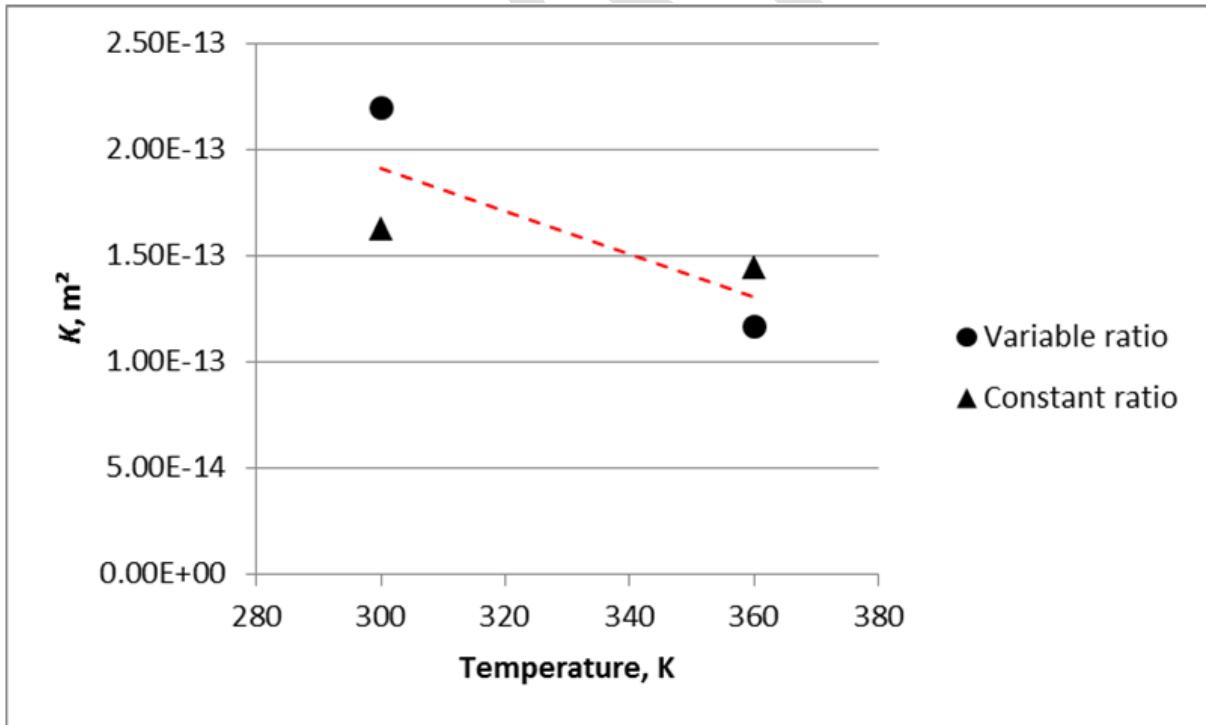
Figure 44 : example of effect of temperature on Kd Darcy permeability (here for C/C sample)

These results seem to show than the permeability decreases with (a rather small) temperature. This result is in line with some published results, and absolutely opposite from other ones. A specific effort was made to clarify in D4.1.5 the details of the analysis of mass flow versus pressure drop measurements, because the permeability parameters derived from them rely on the viscosity and the density assumed for the fluid when it is heated and depressed within the sample…

Some test series were repeated and the possible modification of the sample permeability was checked, according to the test method used for instance for advanced cooled structures testing at MBDA. As summarized below, the possible stress of the conical sample could explain the difference that was shown by these –not initially planned- test series. Between each hot permeability test (here on Figure 45, test b in orange), an ambient permeability test is made (here on Figure 45, test a in blue and afterwards test c in red).
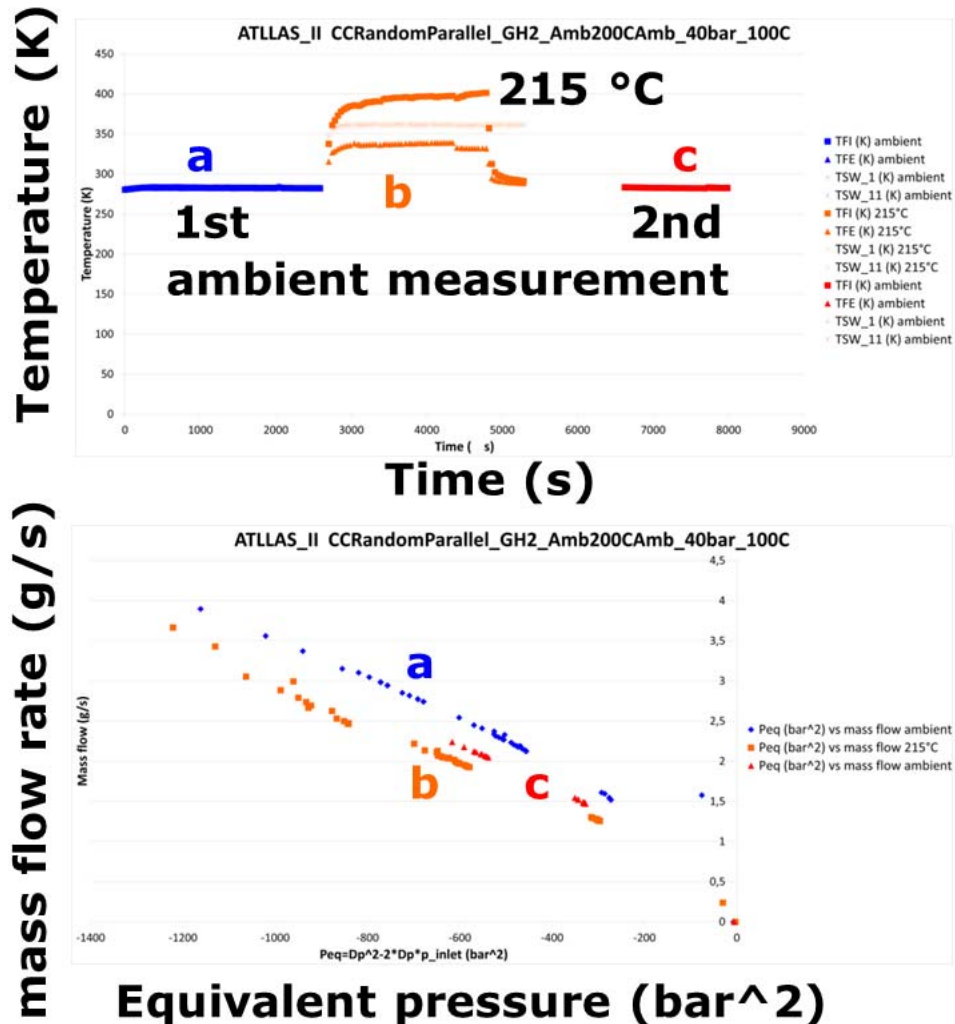
Figure 45 : example of DLR warm permeability measurement

Particular analysis was made in period III, leading to the possible explanation that the thermal stress has changed the sample permeability from one test to another:

- Before the first "hot" run, the sample is assumed **stress free**

- At high temperature, the sample holder will expand and release the sample which will be dragged downstream by the flow

- After cooling, the sample holder will contract **compressing the sample**
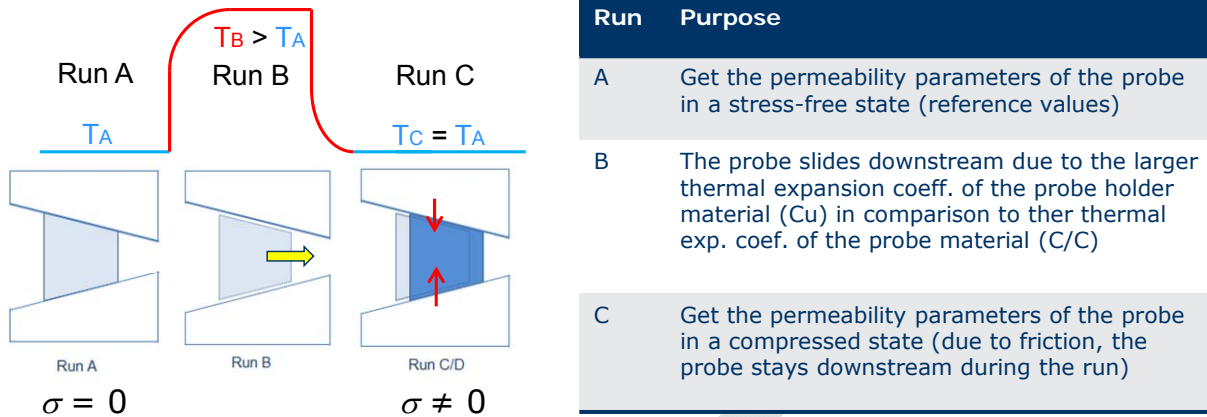
Figure 46 : possible explanation of permeability change during hot test : stress

FEM computations and sample test show that the more the sample is compressed, the more the mass flow is reduced: the permeability of the sample seems to be linearly dependent on the sample stress state based upon a simplified FEM analysis.

The previous test were analysed with the assumption that the ratio between Kd and Kf (laminar and turbulent porous flow parameters) remains constant with temperature. In period III, this assumption was investigated and was shown to be non-mandatory: even we do not assume this assumption, the results remain very similar, as shown below on one example:

α/β	CR	NCR avg.	Diff.
Test 19,20,21	3.19e-6	3.79e-6	+18.9%

$$NRC\ avg = \left(\prod_{i=1}^{N} x_i\right)^{1/N}$$
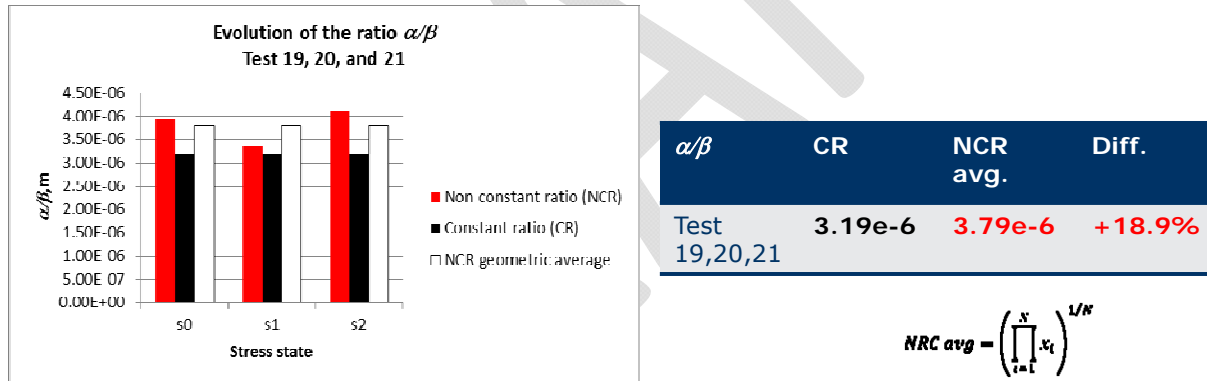
Figure 47 : effect of Kd/Kf ratio assumptions on permeability test analysis

The results of these investigations imply that the permeability of a porous material is dependent on temperature and on stress. Although the number of the investigated test conditions (number of temperature cases and/or number of stress state cases) was narrow, the fit of the permeability parameters values shows that the dependency with temperature and stress of the Darcy´s permeability K and Forchheimer´s permeability G can be cast in the following general equation

$$\begin{cases} K(T, \sigma) = aT + b\sigma + c \\ G(T, \sigma) = a'T + b'\sigma + c' \end{cases}$$

where a, b, c, a´, b´, and c´ are constants.

This experimental study contributes to the difficult question of CMC porous behaviour in ambient or hot temperature with different coolants. It cannot be yet considered as a conclusive one.

This work performed on CMC will be also useful for porous metallic multifunctional structures as the HSS family explained earlier in the report.

In WP4.2 and WP4.3, even if it was not planned in the contract, DLR provided a CMC 12 mm thick panel which was able to be mounted through a special tooling manufactured by MBDA on METHYLE. MBDA tested also the CMC panel under the IR lamps at the end of period2. Post-test analysis allowed to check the thermal properties obtained in ATLLAS-I and in WP3 (data base in D3.0.1).
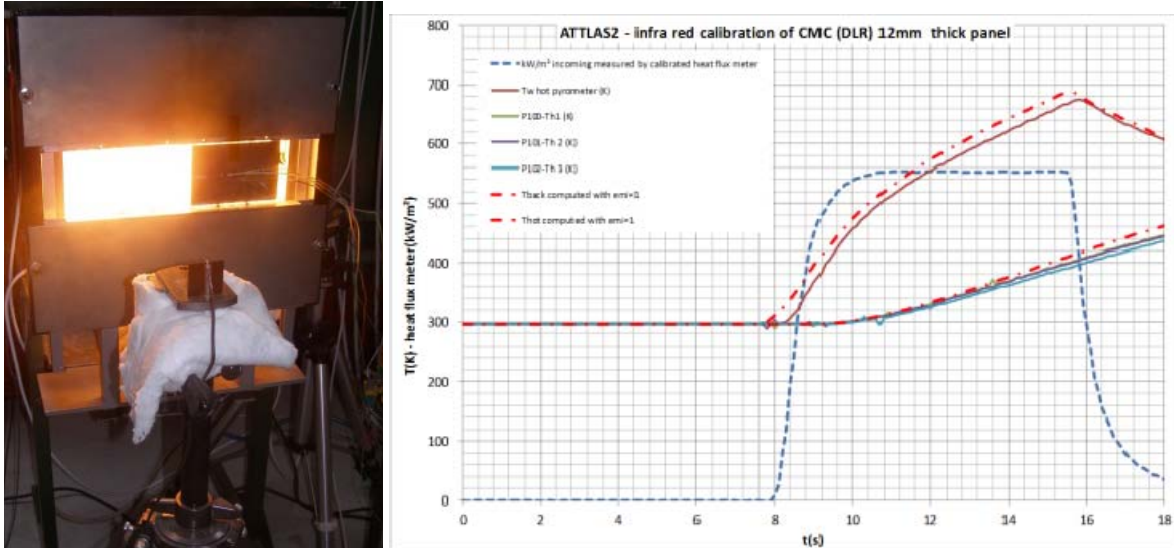
Figure 54 : IR lamp testing and associated post-test analysis with D3.0.1 data base

The panel was successfully tested without any coolant (only radiative cooling through the flame), at the exit of the MBDA dual-mode ramjet, with stoichiometric combustion with flight conditions of Mach 6.
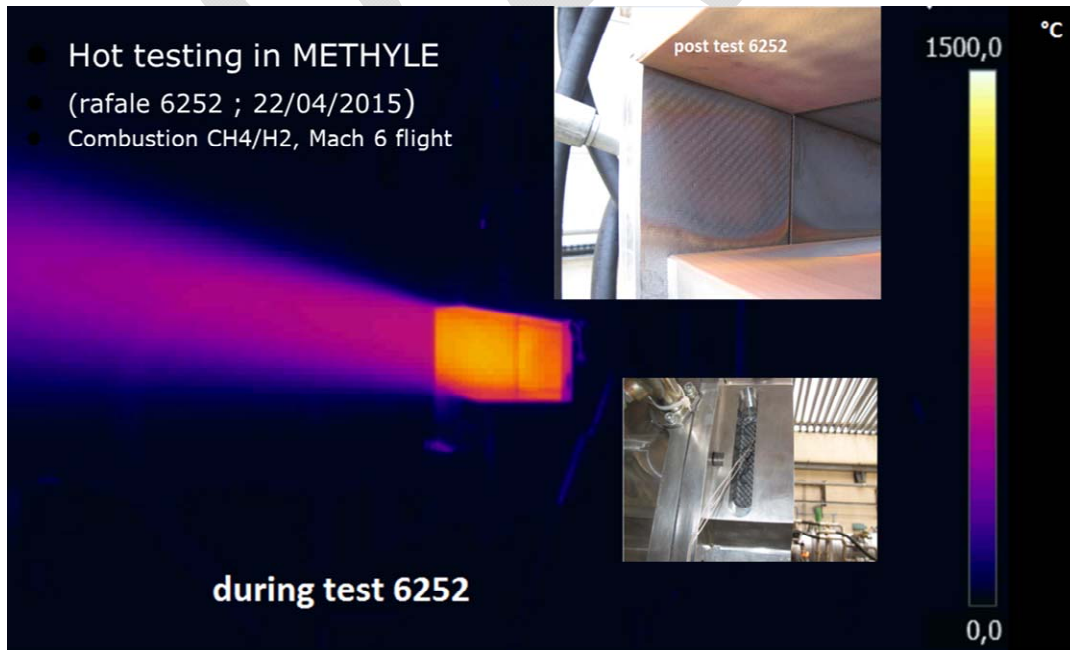
Figure 55 : hot testing of uncooled generic CMC panel at Mach 6 with combustion

5.7   Conclusion/discussion

The following table and figure illustrate in a synthetic way the different systems and materials investigated.

Type	cooling	Material	Technique
Pin fin channel	convective	CMC	PTAH-SOCAR
Injection struts	Transpiration Convective*	CMC	/
	convective	UHTC	/
External wall *	None (radiative)	**CMC**	different
HSS panel	Transpiration /convective	metallic	Porous hollow spheres sandwich
	* : test series not planned initially		
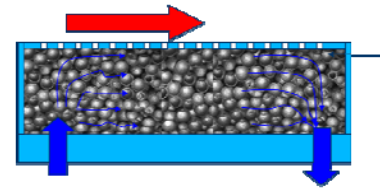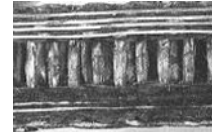
Table 4 : overview of material and structures successfully investigated in WP4

The design structures were tested with different levels of environment representability on one hand and instrumentation on the other hand.

The test were prepared and analysed with design tools and with respect to possible use in high speed combustion environment and integration.

The WP4 tasks lead to intensive design of generic components and relevant successful testing, mostly realized in period 2 and period 3.
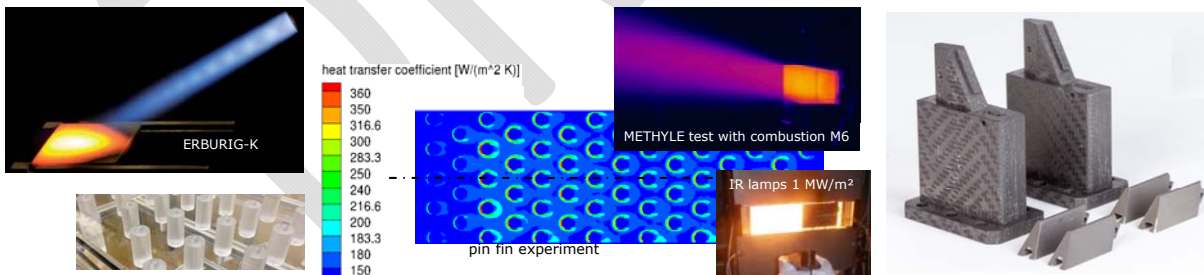
Figure 48 : ATLLAS provides a unique set of results on several advanced structures hot gaz or combustion environments

Besides the current program, benefit and further development is expected by the partners on most of this unique basis.

5   Aero-Thermal-Structural and High-Speed Transition Investigations for External Components

The aero-thermal-structural design for a hypersonic vehicle is a very challenging task and depends on detailed knowledge of the loads (mechanical and thermal), which are significantly different from knowledge and observations coming from subsonic aircrafts. To address these aspects different experiments were setup during ATLLAS2 using the experience from ATLLAS1, LAPCAT1 and 2. In the High Enthalpy Shock Tunnel (HEG) at DLR Göttingen detailed SWBLI investigations addressing geometrical aspects as well as surface temperature effects on boundary layer transition were performed. High frequency instrumentation allowed to analyse the intermittency behaviour from local heat flux data. The same approach was used for supersonic transition experiments at SITAEL with specific focus on roughness induced transition for flat plates and cones. On the computational side detailed Direct Numerical Simulation was applied by SOTON. These data were used for stability analysis methods by SOTON and FOI. Finally improved RANS-modelling approaches has been developed by ESA-ESTEC for design analysis with respect to high-speed transition physics for pressure and heat loads on vehicle structures.

5.1   Experimental Studies for Aero-Thermodynamics on Control Surfaces

The experimental investigations on SWBLI using heated surfaces were performed in the High Enthalpy Shock Tunnel Göttingen (HEG) at DLR. Detailed CFD analysis was performed in advance at ESA-ESTEC to define the requirements for the test model as well as the operating conditions (Fig. XX1).

Test Conditions

| Condition	Unit	XV
p_0	[bar]	290
T_0	[K]	2570
h_0	[MJ/kg]	3
M_∞	[−]	7.46
Re_m	[1/m]	$6.4 \cdot 10^6$
p_∞	[Pa]	2970
T_∞	[K]	243
ρ_∞	[g/m³]	42.4
u_∞	[m/s]	2340
μ_∞	[Pa·s]	$1.56 \cdot 10^{-5}$

$\sim$ 25 km (* U.S. Standard Atmosphere 1976)

$\sim$ 35 km, dT < 20 K
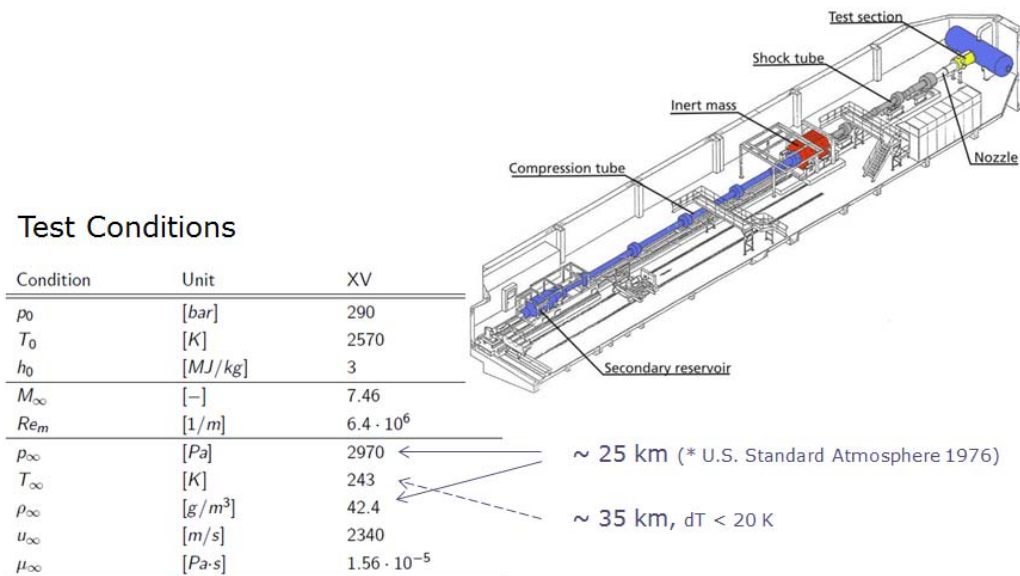
Fig. XX1: Schematic of the HEG and test conditions

The model specification followed several aspects, e.g. impact of boundary layer transition on SWBLI upstream of a flap at angle of attack considering surface temperature effects and the influence of open/closed gap. Thereby high-frequency heat flux and pressure measurements were taken to obtain from the data analysis the intermittency distributions and turbulent spot production rates and to define the transition starting points and the transition lengths. Further details are provided in D5.1.8 [RR1]. The therefore instrumented model is shown in Fig. XX2.
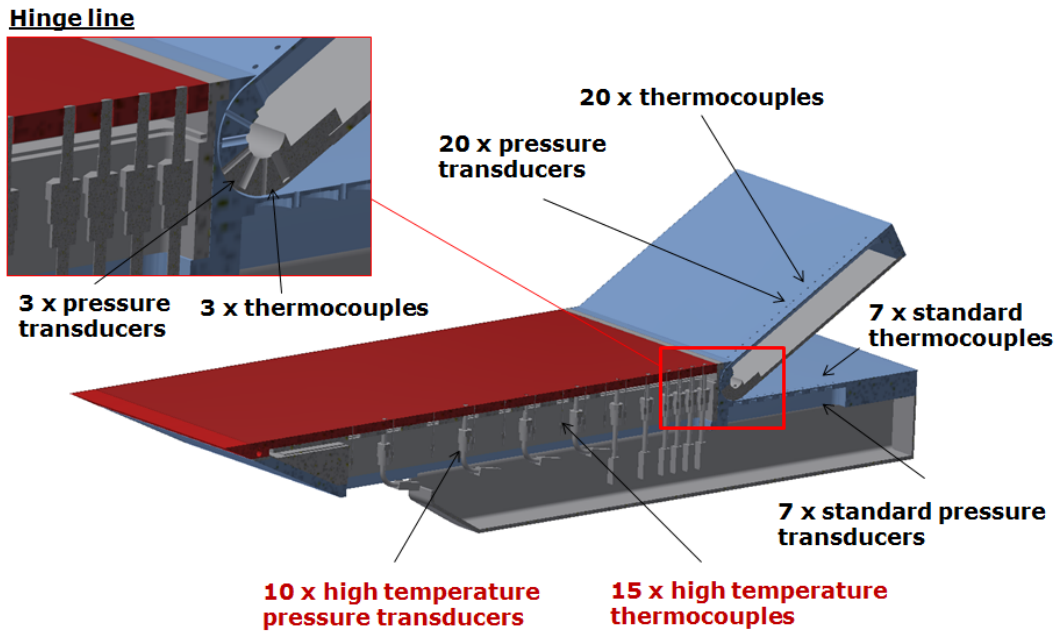
Fig. XX2: Instrumentation selected for SWBLI investigations in HEG

After several commissioning tests the boundary layer intermittency behaviour was confirmed using the approach by Narasimha [RR2] based on the surface heat flux data for unheated and heated wall surface conditions on a flat plate (Fig. XX3).
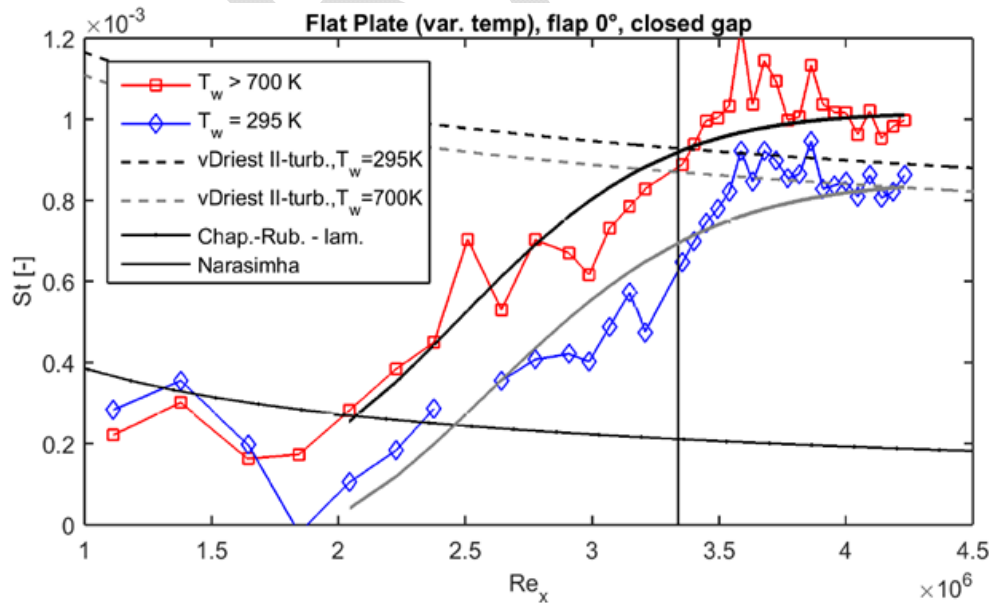
Fig. XX3: Intermittency according to Narasimha based on the measured heat flux distribution

The measured influence of surface wall temperature is well in line with the modelling by Narashima and slightly larger as the predictions by the well-known van Driest-correlation for a fully turbulent

boundary layer. A detailed test matrix setting the different conditions according to the objectives and allowing possible intercomparisons was defined and all experiments performed accordingly. It has been shown, that the surface temperature has a significant effect on the investigated flow situations. The obtained database provides detailed information on this effect and design approaches for a hypersonic cruise vehicle should account for the surface temperature influences on the aero-thermodynamic behaviour on control surfaces.

5.2 Experimental Studies of Roughness Effects on High-Speed Transition

The effects of different roughness configurations have been investigated in the Supersonic Transition Onset Experiments at SITAEL. Thereby the intermittency approach has been used for data analysis as well. Table TT1 provides the methodology used for the data analysis.

| Intermittency (q= heat flux)	$\gamma = \dfrac{q_{meas} - q_{lam}}{q_{turb} - q_{lam}}$	
Spot production rate and transition starting point	$\gamma(x) = 1 - \exp\left[-\hat{n}\sigma(\mathrm{Re}_x - \mathrm{Re}_{xt})^2\right]$ valid for $x \geq x_t$	
Turbulence level	1st method)	$\mathrm{Re}_{\theta_t} = 420 \cdot Tu^{-0.69}$
	2nd method)	$\hat{n}\sigma = 1.5 \cdot 10^{-11} \cdot Tu^{7/4}$
Compressible-to-incompressible equation set	$\mathrm{Re}_{\theta_t,inc} = 0.664 \cdot \sqrt{\mathrm{Re}_{xt}}$	
	$\mathrm{Re}_{\theta_t,M} = \sqrt{1 + 0.38M^{0.6}} \cdot \mathrm{Re}_{\theta_t,inc}$	
	$\hat{n}\sigma_M = \hat{n}\sigma_{inc} \cdot \left[1 + 0.58M^{0.6}\right]^{-2}$	

Table TT1: Equation set used during the post-process

For these studies a new Mach 6 nozzle has been manufactured and qualified in detail verifying, that the flow uniformity is excellent and close to the expected values from the design phase. Using high frequency thin film heat transfer gauges developed at SITAEL within the first two periods of ATTLAS2 has been very successfully used to investigate the effects of several roughness configurations on hypersonic laminar-turbulent transition behavior for flat plates and cones related to different structural parts for a hypersonic vehicle (see Fig. XX4). The tests provide a dedicated database and the associated analysis using intermittency-modelling.
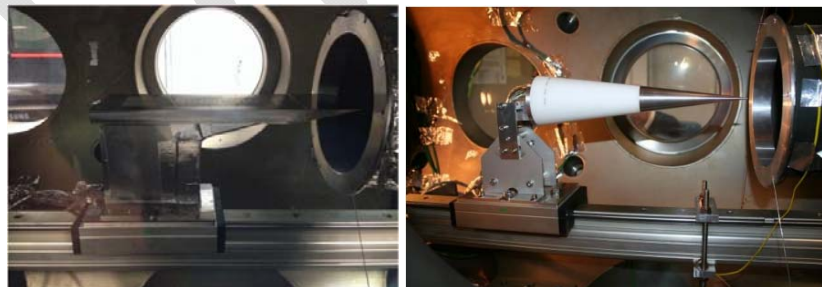
Fig. XX4: Plate and cone test articles installed in Mach 6 nozzle facility

At the end of the experimental test campaigns, post-processing of the data was performed. In particular, estimations of the intermittency distributions (γ), spot production rates ($n\sigma$) and turbulence level (Tu) were carried out and used to calculate the transition starting points (x_t) and the transition lengths, both for the flat plate and the cone. An overview is given in Table TT2. All details are presented in D5.3.3 [RR3].

Test Article	Leading Edge Radius	Total Pressure	Twall	Unit Re	Roughness height	x_t	nσ	nσ_inc	Reθ_M	Reθ_inc	Tu1 (Reθinc)	Tu2 (nσ)
[-]	[mm]	[bar]	[K]	[m^{-1}]	[mm]	[m]	[-]	[-]	[-]	[-]	[%]	[%]
Flat Plate	0	11.80	330	2.64E+07	0	0.184	1.30E-13	9.29E-13	1.46E+03	1.01E+03	0.28	0.20
Cone	0	5.24	293	1.35E+07	0	0.2037	1.40E-13	9.30E-13	1.10E+03	1.03E+03	0.27	0.20
Cone	0	7.58	293	1.93E+07	0	0.1663	1.80E-13	1.20E-12	1.19E+03	7.72E+02	0.41	0.24
Cone	0	9.76	294	2.51E+07	0	0.14	2.70E-13	1.79E-12	1.24E+03	8.35E+02	0.37	0.30
Cone	0	11.85	293	3.06E+07	0	0.1325	6.70E-13	4.45E-12	1.34E+03	8.73E+02	0.35	0.50
Cone	1	9.78	293	2.52E+07	0	0.21	3.05E-13	2.03E-12	1.53E+03	9.37E+02	0.31	0.32
Cone	1	11.91	293	3.06E+07	0	0.205	4.35E-13	2.89E-12	1.66E+03	1.07E+03	0.26	0.39
Flat Plate	0	7.22	332	1.62E+07	1	0.168	7.05E-13	5.04E-12	1.09E+03	7.56E+02	0.43	0.54
Flat Plate	0	9.56	330	2.14E+07	1	0.132	5.50E-13	3.93E-12	1.12E+03	7.71E+02	0.41	0.47
Flat Plate	0	11.47	329	2.55E+07	1	0.119	1.95E-13	1.39E-12	1.16E+03	8.00E+02	0.39	0.26
Flat Plate	0	7.28	325	1.63E+07	1.5	0.202	3.35E-13	2.40E-12	1.21E+03	8.32E+02	0.37	0.35
Cone	0	5.31	293	1.36E+07	0.5	0.2025	4.50E-12	2.99E-11	1.10E+03	8.45E+02	0.36	1.48
Cone	0	7.55	293	1.93E+07	0.5	0.1688	1.22E-11	8.11E-11	1.20E+03	7.74E+02	0.41	2.62
Cone	0	9.78	293	2.52E+07	0.5	0.145	3.33E-12	2.21E-11	1.27E+03	8.41E+02	0.37	1.25

Table TT2: Summary of the intermittency analysis results

5.3 Numerical Investigations on High-Speed Transition

Different aspects were investigated by Direct Numerical Simulations at SOTON in close relation to the above experiments. Thereby the mechanisms involved in the receptivity and linear growth of disturbances in a Mach 6.0 boundary-layer in the presence of individual roughness elements have been analysed in a parametric study including the effect of roughness height, disturbance type, position with respect to the boundary layer, wall temperature and roughness shape.
The sharp-edged roughness induces a pair of counter-rotating stream-wise vortices, which lead to the formation of a low velocity streak through the lift-up of low momentum fluid from the wall. The roughness wake is shows regions of highly detached shear, which are receptive and develop instability modes for a broad frequency range. The chosen computational domain for these studies is shown in Fig. XX5.
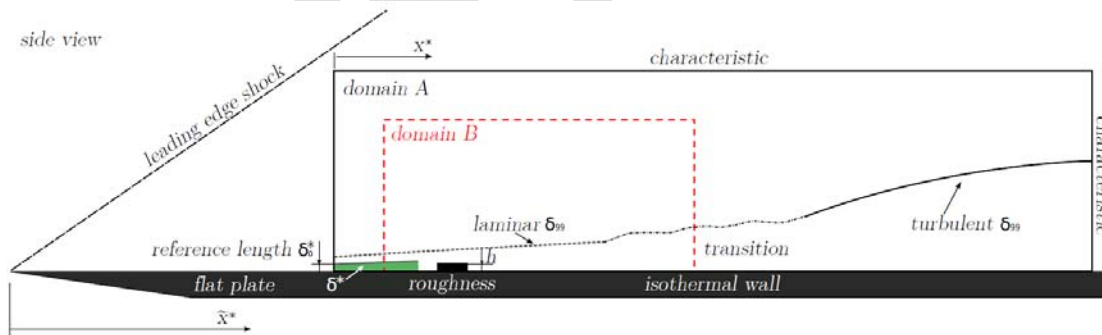
Fig. XX5: Numerical domain for DNS studies

With these full-domain simulations the whole transition process can be investigated. While a sharp-edged roughness element showed significant effects on disturbance growth rates, a smooth bump of similar height and frontal area has been found to have little effect. In accordance to the above experimental studies, it was determined, that there is a considerable difference between the "ramp-cases" (upward or downward see Fig. XX6). An upward ramp does not generate a more unstable wake than the similar roughness element without ramp. A downward ramp at the aft section of the roughness element damps strongly the wake modes and the generated wake is much less unstable. This is illustrated with the different growth rates for disturbance energy shown in Fig. XX7. These results are especially important as both configurations have the same values of Reynolds number based on height or frontal area, such that current empirical models based on these parameters would predict the same effect on transition.

Fig. XX6: Ramp-Up and Ramp-Down configurations investigated

Fig. XX7: Growth of disturbance energy behind the ramp-up (triangle) and ramp-down (inverted triangle) roughness elements

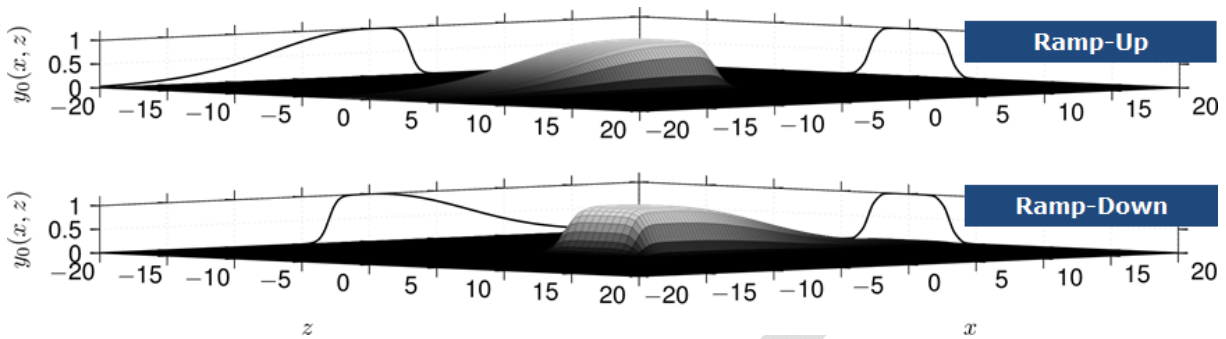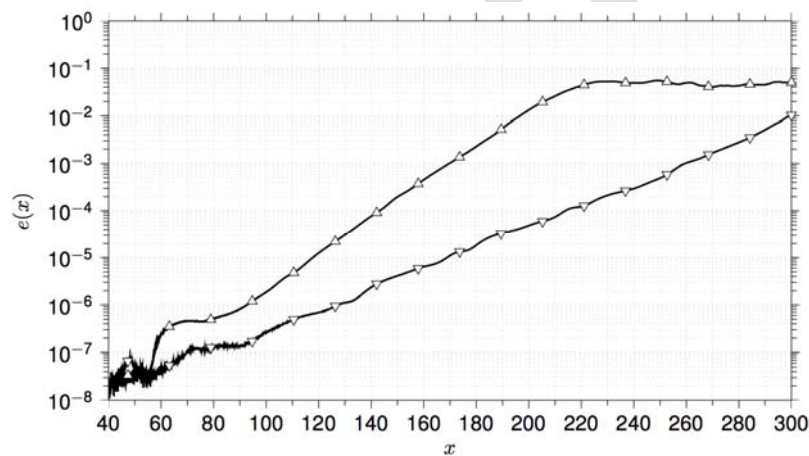Transition criteria for the flat plate and the cone were determined and compared with available criteria and the results obtained during ATLLAS1. Observed specific effects are very well in line with the detailed DNS-analysis of SOTON. The associated bi-local linear stability analysis as described in D5.3.2 [RR4] showed the main characteristics regarding instability modes from DNS-data. Detected shortcomings at high Mach numbers were identified and possible improvements using e.g. PSE-3D methods analysed (as detailed in D5.3.5 [RR5]) to guide further developments in this area.

The comprehensive experimental databases achieved in ATLLAS2 at DLR and SITAEL with the associated intermittency based data analysis and reduction provides in combination with these detailed numerical simulations and physical understanding a new excellent base for the development and validation of engineering models applicable to general design aspects. This path was followed by ESA-ESTEC. The intermittency based approach was used here for improved transition modelling in the TAU-code developed at DLR. Thereby a decoupled approach between turbulence and transition modelling was decided on, to allow the consideration of various physical phenomena (e.g. compressibility, surface temperature, pressure gradients) by specific engineering correlations, which can be easily adopted without changing the available turbulence model implementations. The developed overall model was successfully validated using well-defined literature test cases (see D5.3.6 [RR6] and Fig. XX8). This approach and the achieved generic modelling is unique at present, especially for the aspects concerning supersonic-hypersonic flows.
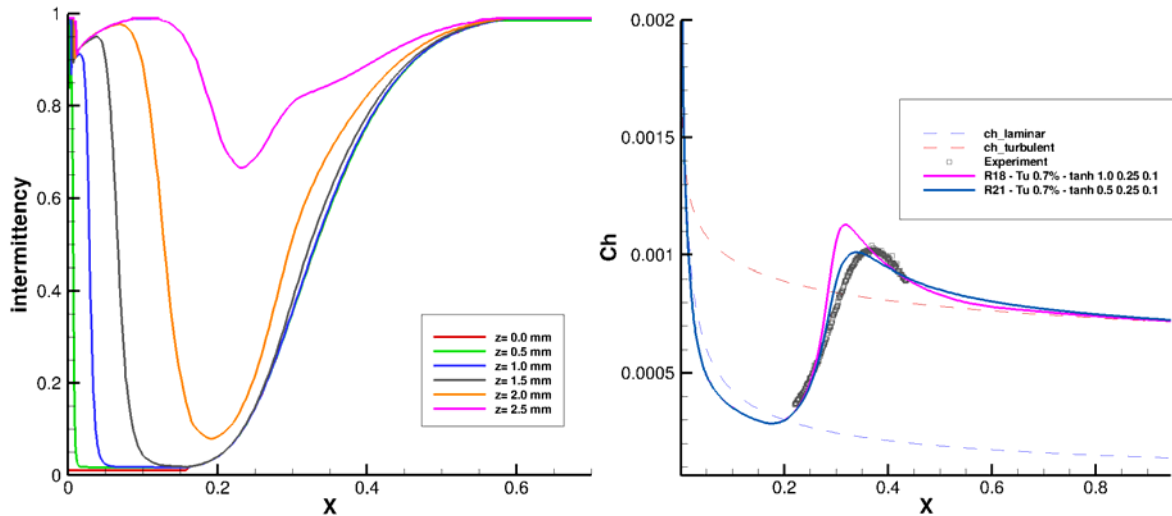
Fig. XX8: Example of results for the RWG Hypersonic case: intermittency evolution over the plate (left) and surface Stanton number (right)

5.4 Shock Wave Boundary Layer and Fluid-Structure Interactions

The experiments for the investigations on unsteady fluid-structure-interaction were undertaken in the trisonic test section (TMK) at DLR in Cologne (see Fig. XX9). The impact of dynamic loads on relatively thin metallic structures were analysed with high-speed schlieren and high-frequency pressure measurements. The structural response was measured with different deformation sensors (optical and capacitive) and strain gauges. The shocks of different strength were generated using a movable wedge structure above the test panels.
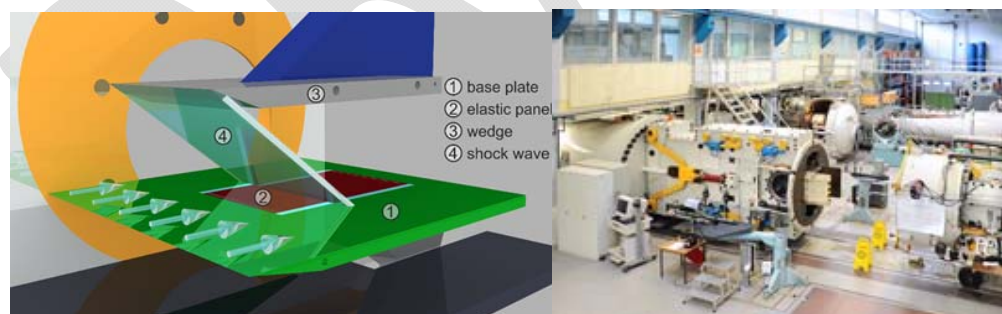
Fig. XX9: Sketch of model for shock induced FSI (left) used in TMK at DLR Cologne (right)

First, a SWBLI investigation on a rigid panel with static and dynamic pressure sensors was performed yielding detailed static pressure distributions for Mach numbers of 2.5, 3.0, 3.5 and 4.0. The frequency behaviour of the static pressures was investigated using dynamic pressure sensors. Second, a combination of the SWBLI with fluid-structure interaction was set-up using an elastic panel. Therefore, CFD simulations were performed using a static aero-elastic coupling modal analysis based on a finite element (3D ANSYS FE) model built at DLR and applied at FOI. This structural finite element model was coupled to a CFD analysis using the CFD code "Edge" [RR7] at FOI (see Del 5.1.5 [RR8]).
Finally additional excitation was imposed on the elastic panel using oscillating magnetic fields applied from underneath the panel. Fig. XX10 shows the elastic panel with the installed sensor

configurations used for displacement measurements by laser sensors in the experiments without excitation (left) and the sensor configuration for the experiments with excitation (right). Details on the sensors and results are given in deliverable D5.1.6 [RR9].
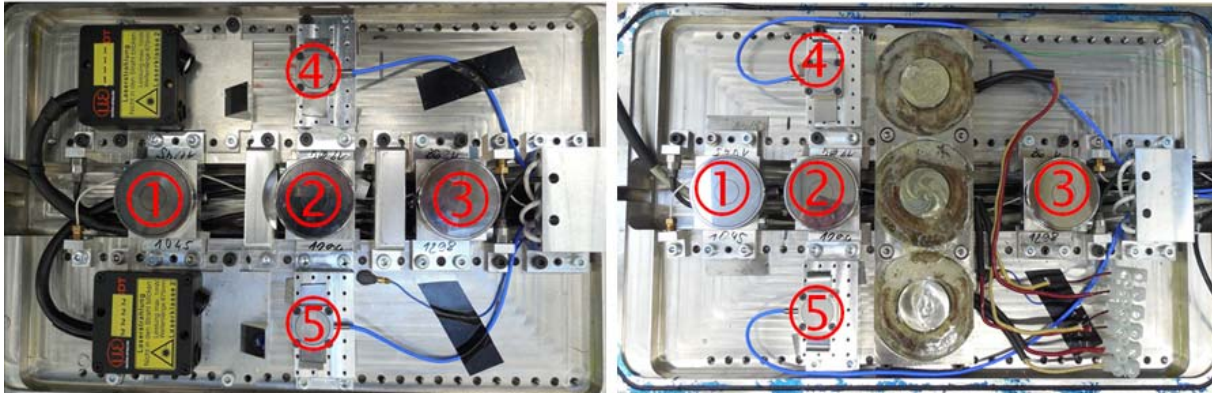
Fig. XX10: Instrumentation in the sensor pod underneath the elastic panel

The measured static pressure distributions for the rigid panel of the shock wave boundary layer interaction in this case for the Mach numbers investigated are shown in Fig. XX11. As expected the impinging shock wave leads to a steep pressure increase. The effect of the separation bubble with the separation shock upstream of the maximum pressure is well detected. It is also seen, that the size of the separation region decreases with an increasing Mach number.
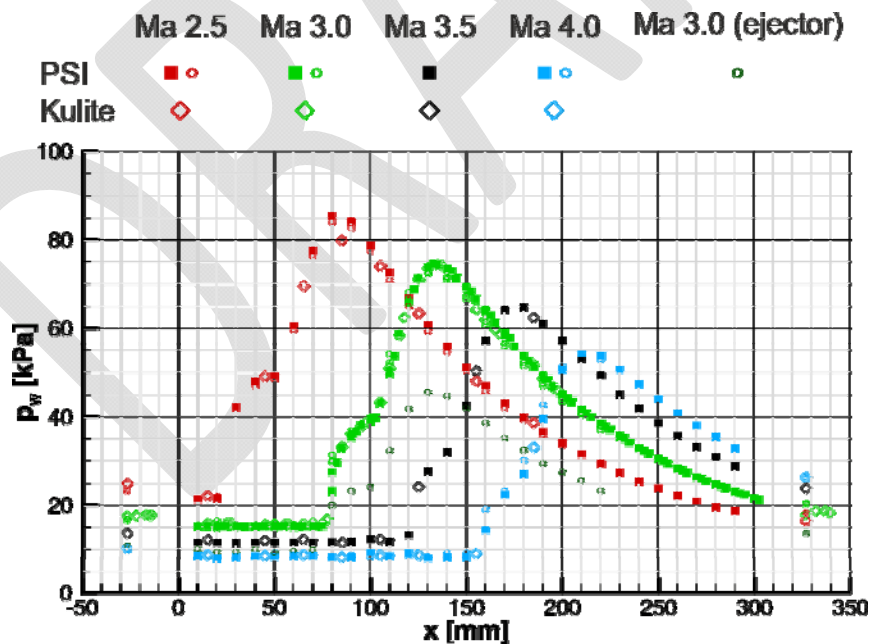
Fig. XX11: Static pressure distributions of the SWBLI on the rigid insert

From the high-frequency Kulite sensors the power spectral density of the pressure could be obtained and analysed. Figure XX12 shows exemplarily the oscillations on the rigid and elastic panel for Ma=3.0.
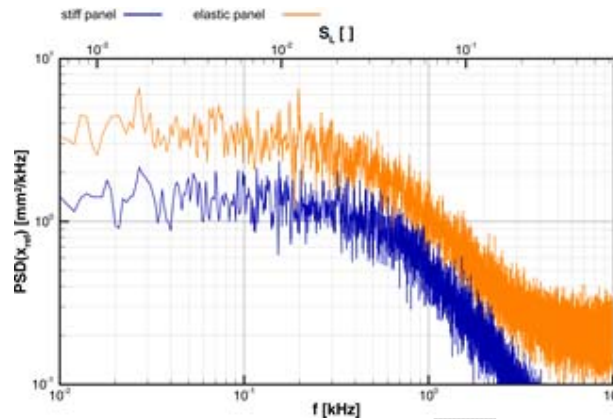
Fig. XX12: Oscillations of the reflected shock at Ma=3.0 on the rigid and elastic panel

This situation has been addressed with detailed DNS-analysis at SOTON for a Mach 4 boundary layer. Two different methods have been used to generate the turbulent boundary layer base flow: a synthetic turbulence (ST) approach simulating bypass transition and a digital filter (DF) approach. The base flows resulting from these two methods indicated to have the correct turbulence intensities and mean velocity profiles. Details are presented in D5.1.4 [RR10]. The comparison of the results from the experimental and the numerical "pseudo- schlieren" is shown in Fig. XX13. These schlieren images show the shock system of impinging and reflected shocks. The instantaneous separation bubble is illustrated by the contour of zero stream-wise velocity in the numerical results. The comparison with the CFD analysis at FOI is given in the bottom picture of Fig. XX13. Although of course very much "diffusive" due to the numerical methodology, the main features are also captured here.

Error! Hyperlink reference not valid.
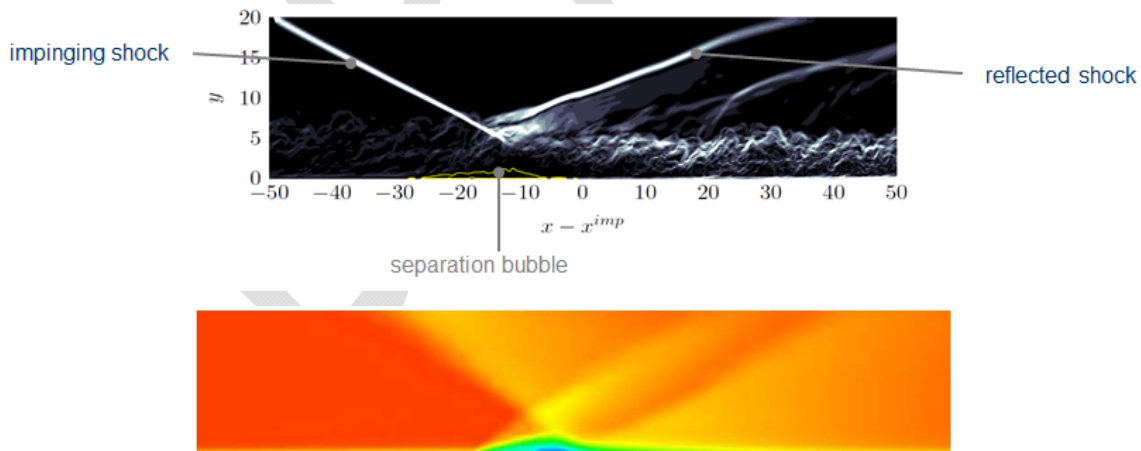
Fig. XX13: Schlieren pictures for SWBLI from experiment (upper), DNS simulation (middle), and CFD (bottom)

The second experimental investigation combined the SWBLI with FSI by applying it to an elastic panel. The deflection of the elastic panel showed a large static component and only a small dynamic component. The deflection is well two-dimensional with the measures along the centerline (y=0) and offset. This is illustrated in Fig. XX14 for one shock generator position at x=-160mm.
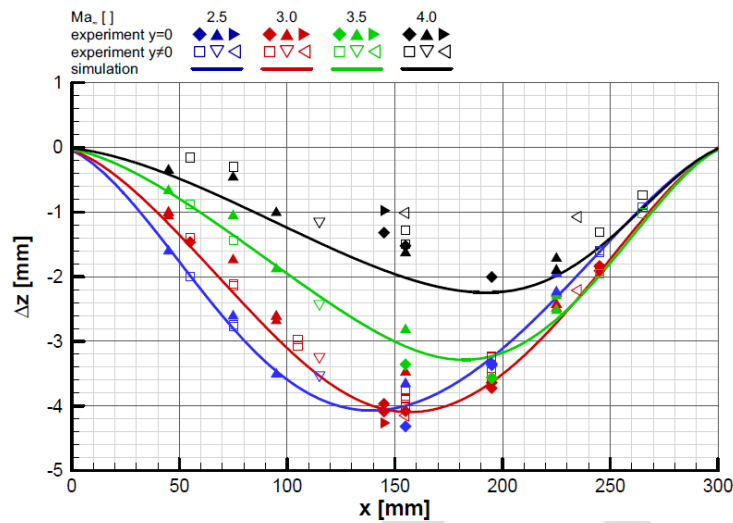
Fig. XX14: Static deflection of the elastic panel for different Mach numbers at x=-160mm

From the dynamic components several frequencies for the panel vibrations could be identified which correlate well with the eigenfrequencies of the elastic panel from structural analysis. An important aspect is thereby the adequate formulation of the structural boundary conditions in comparison between experiment and numerical analysis. With this, the approach of coupled CFD-FEM analysis at FOI has been qualitatively verified but showed still shortcomings for quantitative analysis. The interaction of experiments, detailed DNS and coupled CFD-FEM simulation provide a comprehensive assessment on the physical aspects as well on the needs for accurate engineering design models.

5.5 Aero-Thermal Aspects for Cooling and High Heat Loads

CFD-tools for detailed studies and industrial design are since many years applied to address cooling aspects for e.g. combustion chamber components experiencing high heat loads. The tools and models mainly apply RANS-approaches with different turbulence modelling approaches. They differ between the software packages applied in these terms. Therefore validation work for single jet impingement heat transfer and cooling has been performed by the three partners, ESA, USTUTT and MBDA using a common benchmark case from the ERCOFTAC-database. The best suited models for each partner for this comparison has been applied for the regenerative cooling path featuring the PTAH-SOCAR technology from MBDA as generic pin-fin channel cooling investigated at USTUTT. Application of the chosen models to the experiments for the hot impingement compressible jet investigations at EADS-IW revealed further needed corrections including conjugate analysis of flow, heat transfer, conduction and radiation.

5.6 Benchmark Study for Single Impingement Jet

The case of a single round impinging jet has been selected as test case, since impinging flows are difficult to predict by means of CFD due to the complex flow physics. The validation data is available from an ERCOFTAC test case "C.25 Normally-Impinging Jet from a Circular Nozzle" (mainly based on the experimental results by Cooper et al. [RR11]). This common test case was investigated by the partners with three different flow solvers CFD-ACE (ESA-ESTEC), CEDRE (MBDA) and ANSYS-CFX (USTUTT) with respect to results obtained from different CFD-solvers and implemented turbulence models (see Table TT3). From the available database of this test case and similar studies in literature one specific case (Re=23,000, H/D=2) has been investigated in several independent studies and the data analysed in form of Nusselt numbers for heat transfer

and flow field variables. Due to the symmetry of the physical situation using RANS the geometrical domain to be analysed was simplified and a "quasi"-two-dimensional mesh was applied with different grid resolutions to assess grid independency. All partners used the same mesh regarding spatial discretization of the computational domain and identical boundary conditions (see Fig. XX15). Details are given in D5.2.3+D5.2.4 [RR12].
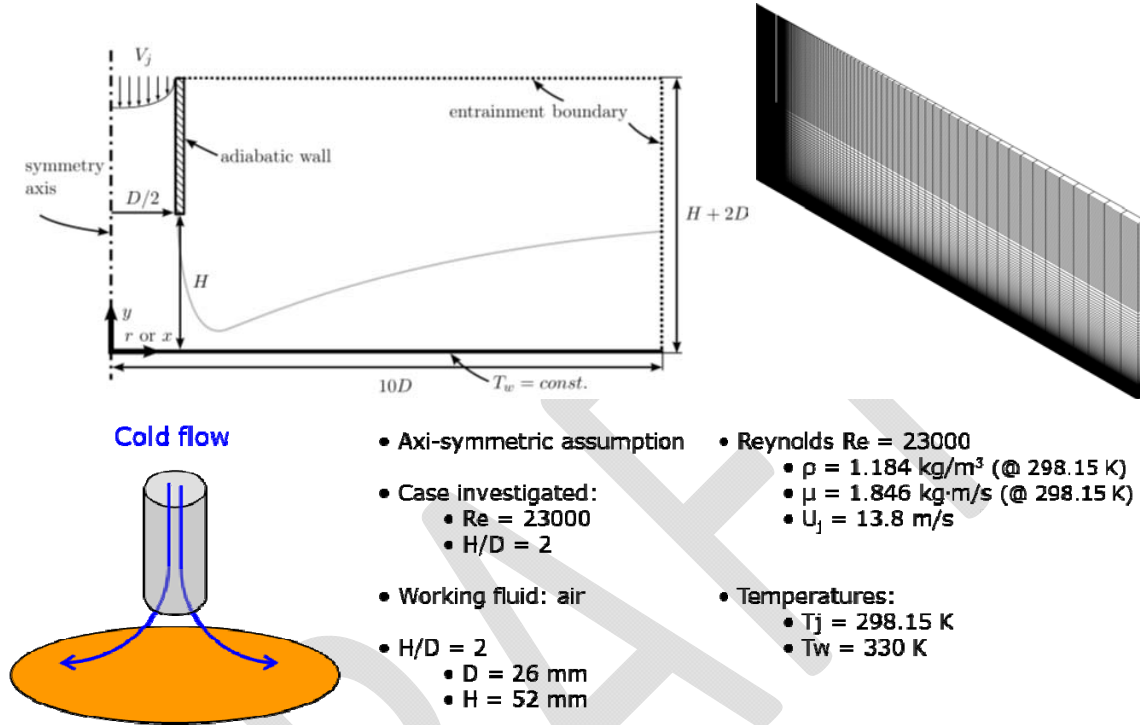
Fig. XX15: Domain and boundary conditions simulated (upper left) and mesh structure (upper right) and boundary conditions (lower)

Partner	Code	Turbulence models	Remark
USTUTT	ANSYS-CFX	k-ε	eddy-viscosity model
	-	k-ω	eddy-viscosity model
	-	k-ω-SST	eddy-viscosity model
	-	BSL	RSM model
	-	SSG	RSM model
	-	SSGLR	RSM model
MBDA	CEDRE	k-L	eddy-viscosity model
	-	k-ω-SST	eddy-viscosity model
	-	k-ε	eddy-viscosity model
ESA-ESTEC	CFD-ACE	Laminar simulation	No turbulence model
	-	k-ω	eddy-viscosity model
	-	RNG- k-ε	eddy-viscosity model
	-	Two-layer- k-ε	eddy-viscosity model
	-	Realizable k-ε	eddy-viscosity model

-	k-ω-SST	eddy-viscosity model

Table TT3: Codes and turbulence models applied for single jet impingement analysis

Fig. XX16 shows exemplarily the results for the radial Nusselt number distributions in comparison to experimental data for the different codes and turbulence modelling applied.
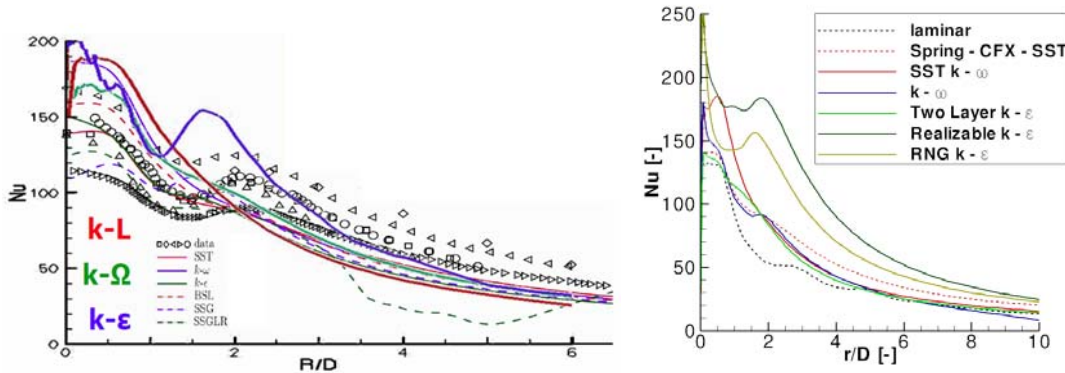
Fig. XX16: Nusselt number distributions. USTUTT and MBDA (full lines) – left; ESA-ESTEC-right

As can be seen a "best modelling" approach" is difficult to define. In view of industrial applications, the use of implemented Reynolds Stress Models (RSM) as used by USTUTT seems not to provide better results than the less expensive k-ω–SST model. The k-ω–SST model was chosen by USTUTT and MBDA for the further heat transfer studies described below, whereas for ESA-ESTEC the two-layer-k-ε and the realizable- k-ε performed better especially in the stagnation point region for heat transfer.

5.7 Pin Fin Channel Cooling

Pin Fin Channel Cooling is one technology well known from gas turbine cooling. The regenerative cooling technology PTAH-SOCAR experimentally investigated in detail on WP 4 for a generic configuration for this cooling technology has been numerically addressed by MBDA and USTUTT. In accordance to the experimental test program in WP4 were performed for the specific configurations in a Reynolds number range from 5,000 to 25,000) using the k-ω–SST model at USTUTT and MBDA. As the parameter ranges with respect to pin spacings in stream-wise and lateral directions and height (S_x, S_y, H) normalized by the pin diameter D differ from most studies available in literature, several cases have been investigated (see Fig. XX17).

Case / variable	Sx/D	Sy/D	H/D
Case 4/5/5	5	5	4
Case 2.67/3.33/3.33	3.33	3.33	2.67
Case 2/2.5/2.5	2.5	2.5	2
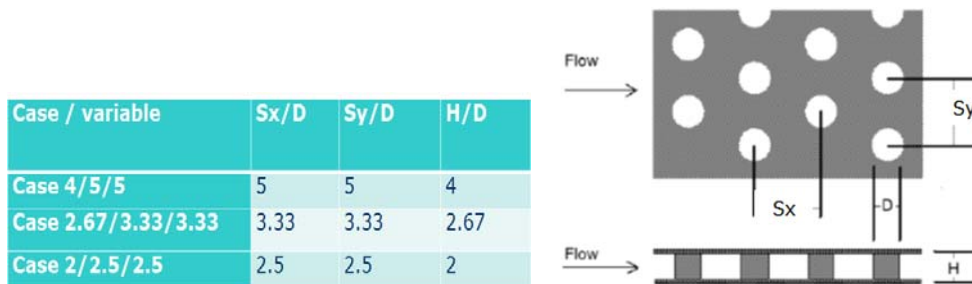
Fig. XX17: Test matrix (upper-left), Parameter definitions (upper-right) and mesh (bottom)

All meshes were constructed as block-structured meshes with hexahedral elements. The reduced computational domain allowed for resolving all walls with very fine mesh scales ($y^+<2$)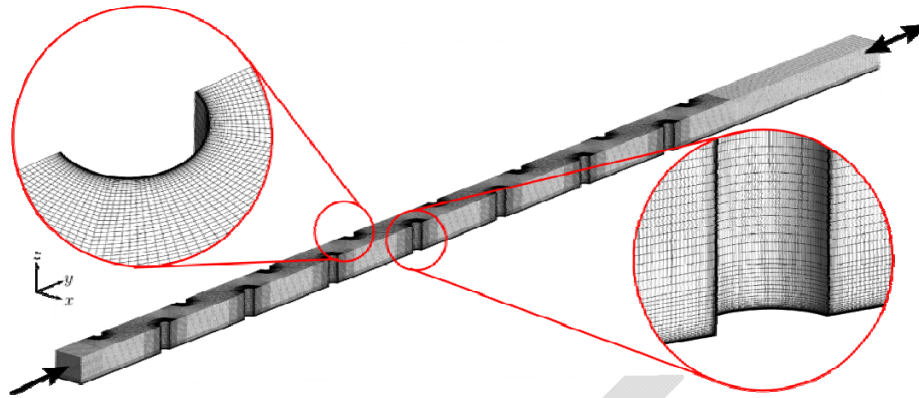 so that a low-Reynolds wall treatment could be used important for accurate heat transfer predicitions. From this modelling analysis, a computational approach has been identified, that can be considered appropriate and computationally efficient at the same time for industrial tool design work. It is based on a half-height channel using periodic boundary conditions as given in Fig. XX18 on the upper right. Further studies showed that adaptions of modelling parameters and modifications regarding e.g. transitional turbulence and curvature correction modification improve the simulation results in comparison to the experimental data for both heat transfer and pressure losses. Thereby also the importance of appropriate boundary conditions as in the experimental investigations has been addressed.
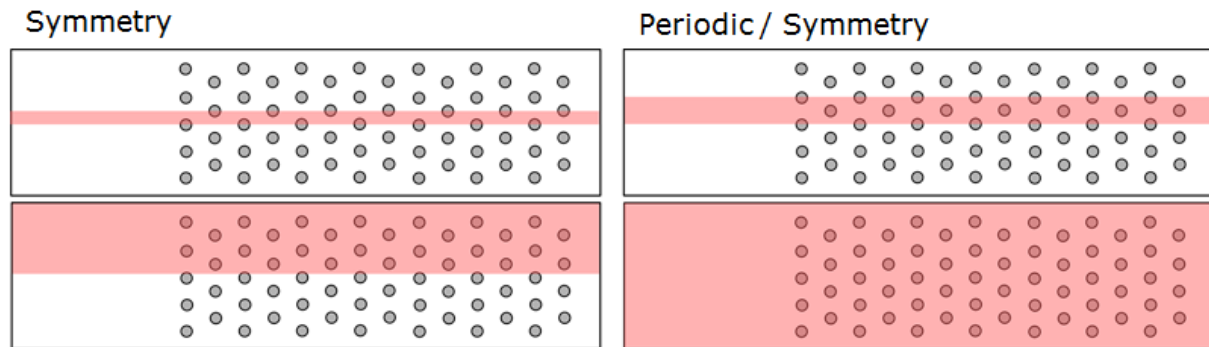
Fig. XX18: Domain modelling approaches using symmetry and periodic conditions for half and full channel heights

Similar findings can be reported form the extensive detailed study of MBDA on the pin-fin channel cooling in comparison to the same experimental results and additional to data from literature as e.g. overall heat transfer characteristics reported in Metzger et al. [RR13]. Using extensive parameter variations it was found, that the pressure losses for all cases could be sufficiently accurate for engenerring applications predicted. Both partners found always an under-prediction of the heat transfer on the side- respective end-walls of the pin-fin channel but an over-prediction of the average heat transfer (as measured) on the pin-fins themselves. This might explain the results from MBDA, that the overall heat transfer also in comparison to the literature data from is generally satisfactorily for industrial design assessments but the row-wise distribution differs as shown in Fig. XX19 for the simulation of the Metzger et al. pin-fin experiments [RR13] for two operating conditions.
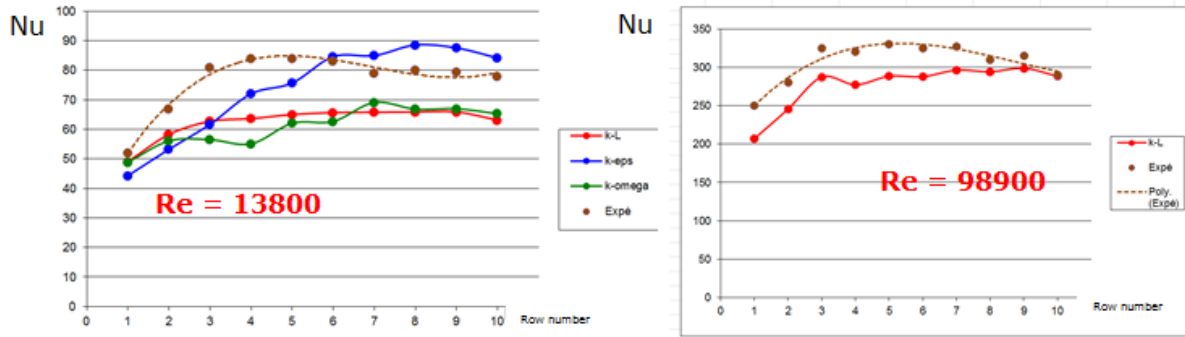
Fig. XX19: Results from MBDA-analysis using CEDRE for Metzger et al. [RR13] test case

For the higher Reynolds number it has not been possible to obtain converged results for two of the three turbulence models tested (k-ω and k-ε). This might be caused by compressibility effects in a strongly confined flow.

5.8 Hot Compressible Jet Impingment

All the findings, assessments, modelling approaches and modifications and made hypotheses described above have to be taken into account for the investigations of the numerical studies on the hot compressible jet impingement case studied experimentally at EADS-IW in WP4 using the ERBURIG[K]-test facility. An oblique high temperature jet impinges on a solid anisotropic plate sample (CMC-material) and heats up the sample with time. Experimental data was obtained with transient local thermocouple and pyrometer data on top of the test sample and on the sidewalls for assessing appropriate boundary conditions as well as the numerical domain (see Fig. XX20).
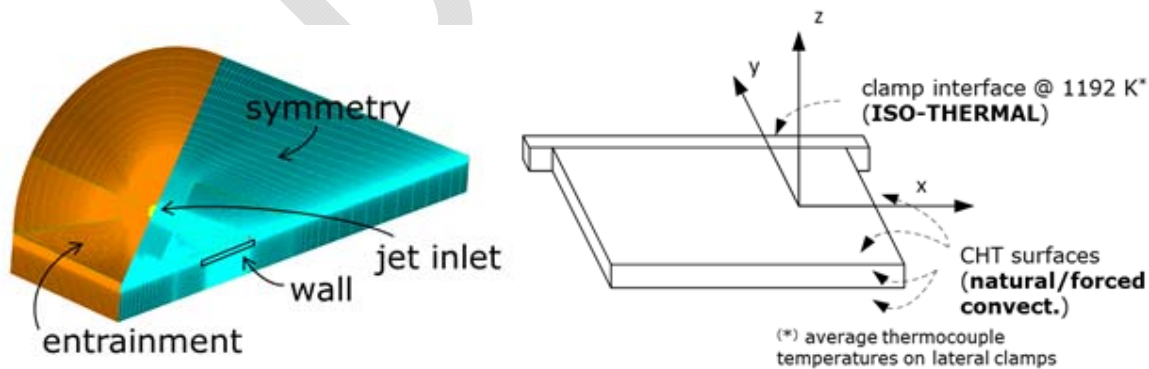
Fig. XX20: Domain modelling and boundary settings

After several investigations the ESTEC analysis using CFD-ACE revealed, that the turbulent viscosity had to be strongly limited to describe the Mach number contours as observed visually in the experiments. With this a good agreement was found for the local temperature measurements in comparison to the experiments. The heat transfer distribution on the solid wall did not well correspond to the numerical results with CEDRE at MBDA. This is shown in Fig. XX21. From the modelling at MBDA it was recognized, that for this situation with high compressibility effects an adaptation had to be applied to the chosen turbulence model. This was achieved with a correction model developed by Aupoix [RR14].
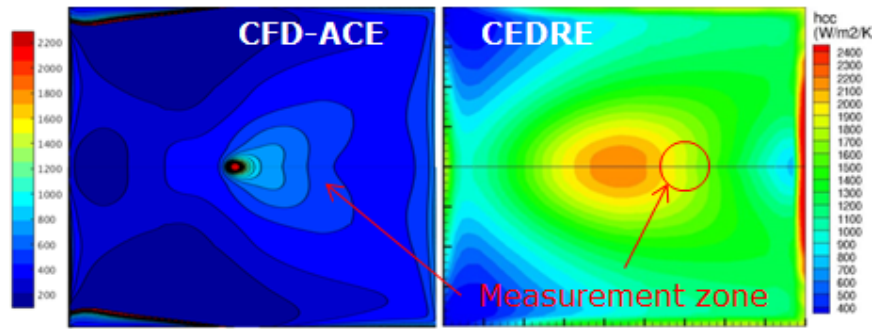
Fig. XX21: Heat transfer distributions as predicted by CFD-ACE and CEDRE indication the measurement locations

With this compressibility correction, CEDRE brought satisfactory results. Further a "quasi-conjugate modelling was applied by interpolating the heat transfer data from the flow solution as boundary conditions for a transient solid conduction analysis of the sample. The major challenges, approaches and achievements are summarized in Table TT4 and detailed in D5.2.1 [RR15].

| Technical Issue/ Challenge	Followed Approach	Main achievements
Prediction of Aero-thermal Loads on Solids	Incompressible cold test case	Common assessment of existing codes Identification of optimum RANS turbulenc model
	Compressible hot test case (CFD-ACE/*ESTEC*) Compressible hot test case (CEDRE/*MBDA*) Modification of computational domain Approach for considering conjugate situation Careful verification of parameters and modelling	Evaluation of conjugate heat transfer. Identified need of compressibility correction f SST k-ω Initial simulation very dissipative, discrepanc to exp. ~1000K Aupoix correction (compressibility effects) f round jets successful Very good agreement with experiment Very good agreement also for dynam response!

Table TT4: Major findings for the hot compressible jet impingement study

5.9 Summary

The activities in WP5 of ATTLAS2 with close interaction between experimental investigations addressing significant areas of aero-thermal-structural interactions for high-speed vehicle concepts, and detailed physical analysis and design tools has been successfully completed thanks to the elongation of the project duration by the EC.

The investigations on **Aero-Thermal-Structural and High-Speed Transition for External Components** provided comprehensive databases for SWBLI at relevant flight conditions.

The wind tunnel model designed and integrated in the High Enthalpy Shock Tunnel Göttingen (HEG) allowed for tests at elevated surface temperatures of up to 800 K and to study flow phenomena such as boundary layer transition or shock wave boundary layer interactions. The conducted tests revealed a boundary layer transition promoting effect of the heated model surface

compared to the cold reference case. Furthermore, an impact on the surface pressure and heat transfer distribution on the flap was found.

The experiments in TMK provide a large database for the investigation of pure SWBLI at Ma $\in$ {2.5, 3.0, 3.5, 4.0} and in combination with a FSI on an elastic panel. The flow leads to a large static deflection and has a significant effect on the panel vibrations and the deflection has a significant effect onto the shock positions and oscillations. Additional excitation with magnetic fields enhance these effects. The detailed numerical analysis by DNS provided in depth results for low frequency loads in SWBLI conditions. The developed FSI engineering modelling using engineering-design coupled approaches were applied and shown to be able to predict the basic qualitative behaviour for the response of an elastic panel but revealed at the same times shortcomings in the current modelling.

A comprehensive approach was take to investigate high-speed transition effects on drag and heat loads from experimental and numerical analysis side and allowed to develop and calibrate engineering laminar-to-turbulent boundary layer transition models including intermittency based ones through detailed DNS, experiments and RANS-CFD. A new and unique database for high-speed laminar-turbulent transition on plates and cones with different roughness elements has been developed. A general frame was setup to allow straightforward implementation of transition model ling into CFD-RANS tools. This approach and the achieved generic modelling is quite unique at present, especially for the design aspects concerning supersonic-hypersonic flows.

The investigations on **Aero-Thermal Aspects for Cooling and High Heat Loads** focused on the further development of thermal design tools. Considering the results obtained with respect to turbulence modelling has shown, that a choice depends on how the model is implemented in a specific code and also on the problem to be addressed (compressibility, high or low Mach number, conjugate situation). The SST k-ω model is recommended for MBDA and for USTUTT, while it is not following ESTEC conclusions, where the two-layer k-ε and realizable k-ε models are preferred. Hereby the importance of close interactions between experiment and simulation to define the appropriate boundary conditions for dedicated assessment and corrections has been shown.

This is especially to be considered for very complex physical situations as e.g., the hot compressible jet impingement case. Here, both simulations by MBDA and ESTEC have initially led to a large overspreading of the jet, and consequently a large under-estimate for heat flux and temperature distributions on the CMC sample. The simulations could significantly improve by considering the compressibility effects present in jets in the turbulence modelling. Several further development approaches have been identified in the scope of an enhancement of industrial tools. In CEDRE, non-isotropic conductivity and emissivity function of the temperature could be of interest. In CFD-ACE, a specific correction for compressible round jets seems to be essential for future applications.

6   Conclusions

7   Report on Societal Implications

>> *To be completed by ALL WP-leaders*

7.1   Deliverables

Replies to the following questions will assist the European Commission to obtain statistics and indicators on societal and socio-economic issues addressed by projects. The questions are arranged in a number of key themes. As well as producing certain statistics, the replies will also help identify those projects that have shown a real engagement with wider societal issues, and thereby identify interesting approaches to these issues and best practices. The replies for individual projects will not be made public.

A General Information *(completed automatically when **Grant Agreement number** is entered.*		
Grant Agreement Number:	ACP0-GA-2010-263913	
Title of Project:	ATLLAS II	
Name and Title of Coordinator:	Dr J. Steelant	
B Ethics		
1. Did you have ethicists or others with specific experience of ethical issues involved in the project?	O **Yes** X **No**	
2. Please indicate whether your project involved any of the following issues (tick box) :		*YES*
INFORMED CONSENT		
• Did the project involve children?		
• Did the project involve patients or persons not able to give consent?		
• Did the project involve adult healthy volunteers?		
• Did the project involve Human Genetic Material?		
• Did the project involve Human biological samples?		
• Did the project involve Human data collection?		
RESEARCH ON HUMAN EMBRYO/FOETUS		
• Did the project involve Human Embryos?		
• Did the project involve Human Foetal Tissue / Cells?		
• Did the project involve Human Embryonic Stem Cells?		
PRIVACY		
• Did the project involve processing of genetic information or personal data (eg. health,		

sexual lifestyle, ethnicity, political opinion, religious or philosophical conviction)	
• Did the project involve tracking the location or observation of people?	

RESEARCH ON ANIMALS

• Did the project involve research on animals?	
• Were those animals transgenic small laboratory animals?	
• Were those animals transgenic farm animals?	
• Were those animals cloning farm animals?	
• Were those animals non-human primates?	

RESEARCH INVOLVING DEVELOPING COUNTRIES

• Use of local resources (genetic, animal, plant etc)	
• Benefit to local community (capacity building ie access to healthcare, education etc)	

DUAL USE

• Research having potential military / terrorist application	

C   Workforce Statistics

3   Workforce statistics for the project: Please indicate in the table below the number of people who worked on the project (on a headcount basis).

Type of Position	Number of Women	Number of Men
Scientific Coordinator		1
Work package leader		6
Experienced researcher (i.e. PhD holders)		
PhD Students		
Other		

4   How many additional researchers (in companies and universities) were recruited specifically for this project?

Of which, indicate the number of men:	
Of which, indicate the number of women:	

8 References

[1]   Aero-Thermodynamic Loads on Lightweight Advanced Structures II (ATLLAS II), Annex I - Description of Work, November 2010.

[2]   Zanchetta M., Walton C., "*Preliminary vehicle definition and performance*", ATLLAS-II Deliverable D2.1.1, GDL, 2012.

[3]   N, "*Nose to tail computations of the vehicle*", ATLLAS-II Deliverable D2.1.2, MBDA/ESA, 2015.

[4]   N,"*Final vehicle definition and performance*", ATLLAS-II Deliverable D2.1.3, GDL/ESA, 2015.

[5]   Kopp A., Garbers N., "*Preliminary structural sizing of ATLLAS-II reference configuration*", ATLLAS-II Deliverable D2.2.2, DLR-SART, 2013.

[6]   G-S Wang, "*Detailed structural design of a thermal protective panel structure*", ATLLAS-II Deliverable D2.2.4, FOI, 2014.

[7]   T. Cain, "*Thermal management layout (cabin requirements)*", ATLLAS-II Deliverable D2.2.1, GDL, 2015.

[8]   Mizuno M., Zhu S., Nagano Y., Sakaida Y., Kagawa Y. & Watanabe M., "*Cyclic-Fatigue Bahavior of SiC/SiC Composites at Room and High Temperatures*",. J. of American Ceramic Society. 79(12), 3065–77, 1996.

[9]   Jarlås R., Rabia H., "*Trade-off study and structural sizing*", ATLLAS-II Deliverable D2.2.3, FOI, 2015.

[10] J. Hodgkinson, "*Aircraft Handling Qualities*", Blackwell Science Ltd, ISBN 0-632-03816-0, 1999.

[11] MIL-F8785C, "Military Specification Flying Qualities of Piloted Airplanes", November 1980.

[12] Flight global, 23 Mar 2011, 747-8 Limit Cycle Oscillation.

[13] S. R. Ginn, "*Sofia 747-SP, Structural Dynamics Overview*", ISBN: 9781289075231, 2013.

[14] Carlson, "*Design and Testing of Flexible Aircraft Structures*", TRITA-AVE 2004:14

[15] Chevalier et al, "*An analytical method for predicting the stability and control characteristics of large elastic airplanes at subsonic and supersonic speeds*", AGARD-CP-46.

[16] N, "*CFD data for caustic and propagation through atmospheric turbulence*", ATLLAS-II Deliverable D2.3.2, ONERA, 2015.

[17] N, "*Sonic boom evaluation by advanced numerical methods*", ATLLAS-II Deliverable D2.3.4, ONERA, 2015.

[18] N., "*Evaluation of focused sonic boom through transonic acceleration*", ATLLAS-II Deliverable D2.3.5, UPMC, 2015.

[19] N., "*Influence of atmospheric turbulence on sonic boom*", ATLLAS-II Deliverable D2.3.6, UPMC, 2015.

[20] Cain T., "*Sonic boom prediction using 3D MOC*", ATLLAS-II Deliverable D2.3.7, GDL, 2015.

[21] Tengzelius U., "*Modelling methods for the plume mixing and chemical kinetics and result from NOx and ozone plume study*", ATLLAS-II Deliverable D2.3.1&3, FOI, 2015.

[22] Koch A., "*Stochastic multidisciplinary improvement of ATLLAS-II reference configuration and geometry data for component optimisation*", ATLLAS-II Deliverable D2.4.1, DLR-SART, 2015.

[23] Rabia H. and Jarlås R., "*Static aero-elastic MDO design methodology applied to a hypersonic wing*", ATLLAS-II Deliverable D2.4.3, FOI, 2014.

[24] Ivanov D., "MDO-Tool extension and application to the ATLLAS-II reference configuration", ATLLAS-II Deliverable D2.4.2, DLR, 2015.

[25] Stoica C., "*Wind tunnel test plan*", ATLLAS-II Deliverable D2.4.4, INCAS, 2015.

[26] Stoica C., "*Wind tunnel test report*", ATLLAS-II Deliverable D2.4.5, INCAS, 2015.

[27] N., "*Numerical verification of the wind tunnel experiments*", ATLLAS-II Deliverable D2.4.6, ESA/FOI, 2015.

[28] B., "*Proposed development roadmap*", ATLLAS-II Deliverable D2.5.1, MBDA/GDL/ESA/FOI, 2015.

[29] A. Wagner, "Shock Waves Boundary Layer Interaction at Varying Model Surface Temperatures in the High Enthalpy Shock Tunnel Göttingen", ATLLAS-II Deliverable 5.1.8.

[30] R. Narasimha. "On the distribution of intermittency in the transition region of a boundary layer", Journal of Aeronautical Science, 24:711–712, 1957.

[31] A. Passaro, G. Cifali, "Transition Experiment Test Report", ATLLAS-II Deliverable 5.3.3.

[32] J.P.J.P. Van den Eynde, and N.D. Sandham, „Sharp-edged roughness transition to turbulence compared to smooth bump cases", ATLLAS-II Deliverable 5.3.2.

[33] N. De Tullio, J.P.J.P. Van den Eynde, and N.D. Sandham, "Receptivity of smooth and sharp-edged roughness elements to free stream disturbances", ATLLAS-II Deliverable 5.3.5.

[34] L. Ferrina, V. Fernández-Villacé, J. Steelant, A. Passaro, "Intermittency based transition modelling", ATLLAS-II Deliverable 5.3.6.

[35] P. Eliasson , "EDGE, a Navier-Stokes Solver for Unstructured Grids", Proceeding to Finite Volumes for Complex Applications III, ISBN 1 9039 9634 1, 2002, pp 527-54.

[36] M. Dalenbring, A. Jirasek, and G.-S. Wang, "Fluid-coupled CFD Simulations of the TKM Experimental Test", ATLLAS-II Deliverable 5.1.5.

[37] S. Willems, A. Gülhan, "Unsteady Fluid Structure Interaction Tests in TMK with modified model ", ATLLAS-II Deliverable 5.1.6.

[38] J.P.J.P. Van den Eynde, N.D. Sandham, "LES of Low Frequency Structural Loading", ATLLAS-II Deliverable 5.1.4.

[39] D. Cooper, D. Jackson, B. Launder, and G. Liao, "Impinging jet studies for turbulence model assessment—I. Flow-field experiments", International Journal of Heat and Mass Transfer, vol. 36, no. 10, pp. 2675–2684, 1993.

[40] J. Steelant, J. Thoemel, V. Fernández-Villacé, E. Dufour, S. Spring, "Modelling of cooled and uncooled structures under various thermal loads & Industrial computations of cooled structures" ATLLAS-II Deliverable 5.2.3+5.2.4.

[41] D. E. Metzger, R. A. Berry, J. P. Bronson, "Developing Heat Transfer in Rectangular Ducts with Staggered Arrays of Short Pin Fins", Transactions of the ASME, J. of Heat Transfer, vol. 104, pp. 700-706, 1982.

[42] B. Aupoix, "Modeling of compressibility effects in mixing layers", J. of Turbulence, Vol. 5, 2004.

[43] E. Dufour, V. Fernández Villacé, J. Steelant, "Thermal load prediction for HVOF tests", ATLLAS-II Deliverable 5.2.1.

9   Annex A

10 Annex B

DRAFT